Universitat Jaume I
Departament de Ciències Experimentals
Area de Física Aplicada

Estudio de los procesos de intercalación en materiales electrocrómicos (a-WO_3, polímeros conductores y viológenos)

Jorge García-Cañadas

Dirigida por Germà Garcia-Belmonte

Tesis Doctoral
Castellón de la Plana, septiembre 2006

El Dr. Germà Garcia Belmonte, profesor Titular del Área de Física Aplicada del Departamento de Ciencias Experimentales de la Universitat Jaume I de Castellón,

Certifica: que la Tesis Doctoral “Estudio de los procesos de intercalación en materiales electrocrómicos (a-WO_3, polímeros conductores y viologenos)” ha sido desarrollada bajo su dirección en el Área de Física Aplicada del Departamento de Ciencias Experimentales de la Universitat Jaume I de Castellón, por Jorge García Cañadas.

Lo que certifico para los efectos oportunos en Castellón de la Plana, a 4 de septiembre de 2006

Fdo. Dr. Germà Garcia Belmonte

A Trini y Lucio

Esta Tesis ha sido realizada, y consecuentemente será defendida, de forma adecuada para la obtención del título de *Doctorado Europeo.*

Previamente a la defensa de la Tesis Doctoral, este trabajo ha sido evaluado por tres censores europeos independientes, Prof. François E. G. Henn *(Université de Montpellier 2, Montpellier, Francia),* Prof. Laurence M. Peter *(University of Bath, Bath, Reino Unido)* y el Dr. Emilio J. Palomares *(Institut Català d'Investigació Química, Tarragona, España)*.

Agradecimientos

Mucho ha sido el tiempo que ha transcurrido desde que comencé mi andadura para obtener el Título de Doctor, hasta el día de hoy que indica el final de esa etapa. Si no me equivoco han sido 6 largos años en los que he vivido experiencias importantes e inolvidables, que incluso alguna de ellas nunca llegué a imaginar.

Todo empezó en la quinta planta del Departamento de Química Inorgánica de la Universidad Autónoma de Madrid, donde empecé a trabajar en el laboratorio de la Dra. Carmen Navarro, a la que agradezco enormemente su amistad y su ayuda en aquellos días en que uno recién acabada la carrera, no tiene claro hacia donde tirar. Allí también compartí gratos momentos con dos buenas compañeras, Eva y Dori, a las que agradezco la atención que me prestaron, la paciencia que tuvieron y esos primeros consejos para un investigador novato.

Poco después pasé unos pocos meses en el laboratorio del Dr. Josè Manuel Pérez "Petrucci", donde conseguí mi primera publicación científica. Junto a él, su compañero Miguel Ángel y el resto de becarios del laboratorio pasé quizás los meses más divertidos de mi doctorado. Gracias por aquellos días tan agradables.

Tras finalizar mi temporada en el área de la Química Bioinorgánica me sumergí en el mundo de la Electroquímica bajo la supervisión de María Luisa Marcos, una de las mejores docentes que conozco y la persona que más se ha preocupado por responder a mis preguntas. No os imagináis la suerte que es tener a alguien así a tu lado. Agradezco también su ayuda a los profesores Jaime González Velasco y Gonzalo Rodríguez. Su colaboración fue de gran ayuda para conseguir el Título de Estudios Avanzados y varias publicaciones más.

Un momento clave en mi andadura fue mi estancia en la universidad de Bath del Reino Unido bajo la supervisión del profesor Laurie Peter. Fue una experiencia dura pero gratificante, sobre todo gracias a grandes amigos que conocí en aquellas tierras. Mi más sincero agradecimiento al Dr. Upul Wijayantha y familia y al Dr. Shin Ushiroda "Champion" con el que compartí despacho y los mejores momentos en Bath, una de las ciudades más preciosas y elegantes que he visitado. Pasear por sus calles y descansar en sus parques tiene un encanto muy especial.

Cuando volví de Bath tomé una decisión que nunca imaginé que tomaría. Me fui a vivir a Castellón de la Plana, donde entré a formar parte del grupo del profesor Juan Bisquert. Aquí he pasado la temporada más fructífera profesionalmente. Agradezco a

los profesores Germà Garcia Belmonte y Juan Bisquert la oportunidad que me han dado de trabajar en su equipo, la confianza que me han brindado así como la formación que me han proporcionado. Los comienzos no fueron fáciles, era un químico rodeado de físicos cuya investigación estaba basada en conceptos nuevos que no eran fáciles de asimilar, pero finalmente creo que he logrado entender gran parte de ellos. Me gustaría agradecer especialmente al Dr. Fran Fabregat su ayuda en este aspecto y a mis compañeros Iván, Ángela, Magda, Noemí, Chema y Eva por crear un buen ambiente de trabajo. También quisiera agradecer el tiempo que compartí con los visitantes internacionales que estuvieron por nuestro laboratorio, en especial con Roland Hass (¡Que bien te lo pasaste, eh!), y con el resto de becarios que andan por la universidad [Teo, Nahum, Caraqui (¿Por qué te fuiste?), Santi, Laura "La prima" y muchos más].

Al margen del aspecto profesional quisiera agradecer de forma muy especial a toda la gente del Club Frontenis Serradal, con quienes he compartido los mejores momentos en Castellón practicando mi deporte favorito y que me aportan esa dosis de *desconexión* que siempre es necesaria para mantener tu equilibrio mental. Tampoco quiero olvidarme de mis amigos de toda la vida a los que ya veo muy poco debido a la distancia (Bienzo, Carlos, Ainhoa, Mari, Luis hijo, Vielba, Unai, Javi "Metal", la gente del Club Henares y muchos más).

Gracias también a Marillion, Pink Floyd, los Burning, Nexx, Mago de Oz, Triana y un montón de grupos más que han puesto la banda sonora a estos días de doctorado y que con su música de fondo me hacen los días más agradables.

Finalmente estaré siempre agradecido a mis padres, Lucio y Trini, por darme la oportunidad de estudiar y aceptar mis decisiones, aunque más de una no les haya hecho mucha gracia. Gracias por vuestro esfuerzo y preocupación por sacarme adelante. Agradecer también al resto de mi familia, sobre todo a mis hermanos, Dani y Laura.

Index

Objetivos de la tesis

Objetivos de la tesis

Los materiales electrocrómicos presentan un cambio reversible en sus propiedades ópticas cuando son oxidados o reducidos electroquímicamente mediante la aplicación de un voltaje externo. Estos materiales tienen importantes aplicaciones como paneles informativos con memoria óptica, las ventanas electrocrómicas que permiten modular la cantidad de luz y energía solar que entra desde el exterior en vehículos y edificios, y espejos retrovisores antideslumbrantes que hacen la conducción más segura.

Numerosos materiales presentan electrocromismo, tanto de carácter orgánico como inorgánico. Como inorgánicos destacan los óxidos metálicos, siendo el WO_3 el más ampliamente estudiado. Dentro de los orgánicos resaltan los polímeros conductores y los compuestos bipiridínicos (viológenos).

En esta tesis se ha realizado un estudio termodinámico mediante técnicas electroquímicas de los procesos de coloración en el WO_3 amorfo, los polímeros conductores y los viológenos. Este tipo de estudio nos permite conocer mejor los fenómenos físicos que se producen en dichos materiales y poder así entender mejor su funcionamiento para lograr mejorar los dispositivos.

Los objetivos específicos del estudio realizado son los siguientes:

- Introducción al campo de investigación de los materiales electrocrómicos destacando los avances y problemas actuales de esta tecnología.
- Revisar conceptos termodinámicos importantes en el estudio de los materiales electrocrómicos.
- Obtener e interpretar la respuesta de películas de a-Li_xWO_3 a medidas de impedancia electroquímica.
- Interpretar los voltamogramas cíclicos típicos que presentan las películas de a-

WO_3 amorfo.

- Estudiar la respuesta electroquímica de películas de a-Li_xWO_3 de diferentes espesores cuando es cargado a corriente constante en condiciones de quasi-equilibrio.
- Estudiar la difusión de los iones Li^+ en el interior de la red del a-WO_3.
- Desarrollar un modelo capaz de explicar las principales características de los picos de oxidación resultantes en los experimentos de voltamería cíclica en los polímeros conductores.
- Averiguar mediante medidas electroquímicas y electro-ópticas que procesos intervienen en la coloración de las moléculas de viológeno cuando estas son adsorbidas sobre un electrodo de TiO_2 nanoestructurado.
- Crear un dispositivo electrocrómico que funcione usando un film de a-WO_3 como material electrocrómico.

Para conseguir los objetivos propuestos se siguió el siguiente plan de trabajo:

- Revisión bibliográfica del estado del arte de los materiales electrocrómicos.
- Preparación y caracterización de películas de WO_3 amorfo depositadas sobre un substrato de vidrio conductor mediante la técnica de evaporación por haz de electrones.
- Obtención y análisis de espectros de impedancia electroquímica obtenidos a distintos valores de inserción en películas de a-Li_xWO_3.
- Realizar medidas de voltametría cíclica de las películas de a-Li_xWO_3 y examinar los cambios que presentan al variar la velocidad de barrido y otros parámetros.
- Explicar las principales propiedades de los voltamograms mediante un modelo

electroquímico sencillo.

- Examinar la evolución del voltaje con el grado de intercalación en filmes de a-Li_xWO_3 de distintos espesores en condiciones de quasi-equilibrio y obtener el valor de la capacidad química.
- Proponer un modelo termodinámico capaz de interpretar los valores de capacidad química observados basado en distorsiones de la red de a-WO_3 causadas por su interacción con el intercalante.
- Obtener los cambios volumétricos experimentados por las películas de Li_xWO_3 mediante perfilometría óptica y compararlos con los predichos por nuestro modelo.
- Calcular y analizar la variación con la composición del coeficiente de difusión de los iones Li^+ en la red de WO_3 mediante la técnica de impedancia electroquímica.
- Revisar los modelos nernstianos existentes para explicar las propiedades de los voltamogramas de polímeros conductores.
- Describir un modelo basado en distribuciones Gaussianas de estados de energía capaz de explicar los picos de oxidación observados en los voltamogramas de los polímeros conductores.
- Preparación de películas de poli(pirrol) como ejemplo de polímero conductor y ver su comportamiento voltamétrico y comparar los picos voltamétricos obtenidos con el modelo propuesto.
- Obtener mediante medidas de impedancia electroquímica las distintas contribuciones a la capacidad del electrodo de n-TiO_2 modificado con moléculas de viológeno.

- Explicar las principales características de la respuesta electro-óptica de los electrodos de n-TiO_2 modificados con moléculas de viológeno y diferenciar las contribuciones asociadas al TiO_2 y a la oxido-reducción del viológeno.
- Preparar las diferentes partes de que consta un dispositivo electrocrómico, ensamblarlo y estudiar su funcionamiento y estabilidad.

Tras la realización del plan de trabajo propuesto, se obtuvieron nuevos modelos capaces de describir la termodinámica de distintos compuestos electrocrómicos como el a-WO_3, los polímeros conductores y los electrodos modificados con moléculas de viológeno. Los principales resultados y conclusiones de nuestra investigación se describen a continuación:

- Sobre el a-WO_3: Se interpretaron los voltamogramas característicos del a-WO_3 mediante el uso de un circuito sencillo R_SC. Se explicaron las curvas voltaje-composición obtenidas para películas de diferentes espesores mediante un modelo termodinámico basado en distorsiones de la red del óxido debidas a las interacciones con el intercalante. La comparación de la función termodinámica con un modelo anterior que describe las expansiones de la red producidas durante la intercalación, nos permitió obtener valores de los cambios volumétricos experimentados por las películas de a-WO_3. Usando métodos electroquímicos sencillos y analizando las curvas de capacidad química podemos calcular el cambio volumétrico producido en los filmes, que muestra un buen acuerdo con los valores obtenidos directamente mediante perfilometría. El coeficiente de difusión de los iones Li^+ en la red del óxido decrece con la composición, lo que es coherente con el modelo propuesto basado en las

distorsiones de la red.

- Sobre polímeros conductores: Los voltamogramas de estos polímeros presentan picos de oxidación bastante anchos seguidos de un plató de corriente, que no pueden ser explicados por medio de modelos Nernstianos. Un modelo de distribuciones de energía Gaussianas es propuesto capaz de explicar dichos picos hasta la aparición del plató de corriente. El modelo proporciona una herramienta muy útil para analizar las distribuciones de polarones y bipolarones en dichos polímeros.
- Sobre el n-TiO_2 modificado con moléculas de viológeno: Se diferenciaron las diferentes capacidades químicas que contribuyen a la respuesta capacitiva total del sistema y se explicaron los cambios de transmitancia observados de forma simultánea a la obtención de los voltamogramas. Finalmente se desacopló del voltamograma la respuesta asociada únicamente a la oxido-reducción del viológeno.
- Sobre los dispositivos electrocrómicos: Se prepararon dos dispositivos basados en a-WO_3 como capa electrocrómica, usando un líquido iónico como electrolito y Sb-doped nanoporous SnO_2 ó poly(3,4-etilendioxipirrol) como ánodo. Los dispositivos mostraron un buen funcionamiento pero baja estabilidad.

Varios aspectos de nuestra investigación necesitan de un estudio más profundo y quedan sujetos a investigaciones futuras. Varios de dichos aspectos se citan a continuación.

- La termodinámica de intercalación de iones Li^+ en películas de a-WO_3 muestra un comportamiento claramente distinto para filmes de 100 nm de espesor en comparación con películas más gruesas, ya que no se observan cambios

volumétricos a lo largo del proceso de intercalación para dicho espesor. Este hecho apunta hacia la posible existencia de un mecanismo de intercalación particular gobernado por la reducción del espesor.

- La voltametría de polímeros conductores presenta un plató de corriente una vez alcanzado el pico de oxidación. Con el modelo de distribuciones Gaussianas descrito aportamos una descripción de los picos volumétricos hasta alcanzarse dicho plató. Se cree que en esa región el sistema está dominado por una corriente capacitiva, pero su origen aun no esta bien entendido. Tratar de explicar este comportamiento junto a los efectos de histéresis que se manifiestan en dichos polímeros queda pendiente para futuros estudios.
- Una vez estudiado el comportamiento del electrodo de n-TiO_2 modificado con moléculas de viológeno de manera independiente, sería interesante estudiar su comportamiento en los dispositivos (sistema de dos electrodos), donde pueden producirse movimientos de la bandas del TiO_2 o nuevas formas de conducción por saltos electrónicos a través de las moléculas de viológeno.

1. Introduction

1. Introduction

Electrochromics are materials that have the ability of changing their optical properties in response to an external applied potential. They can switch in a reversible way from transparent to coloured or between two different coloured states. Some features that make them promising materials are that only few volts are needed to produce the optical change and they are able to keep their colouration state for a long time without a constant application of the external voltage.

Several successful applications for these materials have been found. They are used in anti-dazzling vehicle mirrors to provide a safer conduction, in informative panels with optical memory and as electrochromic windows to control the amount of light and solar energy entering in buildings and vehicles.

The most studied electrochromic material is the WO_3 which is the most promising for electrochromic windows. Conducting polymers also show electrochromism and they are acquiring a great interest due to the fact that they can be easily processed. Viologen molecules attached into a nanostructured electrode or in solution are the most commercially successful electrochromic material so far, it takes part in anti-dazzling rear view mirrors and informative panels. The physical processes that produce the optical change in these materials are not fully understood yet, and their knowledge is necessary to be able to improve the devices.

In the case of amorphous metal oxides such as the WO_3, electrons are injected in the material at the same time that small cations from the electrolyte, such as Li^+ or H^+, become intercalated in its structure to keep the charge balance. The voltage in the a-WO_3 layer changes with the extent of intercalation. Moreover, it is thought that the process that limits the rate of colouration is the diffusion of cations in the bulk of the a-

WO_3.

Conducting polymers can be easily electrodeposited onto a transparent conducting substrate. When they are oxidised, electrons from their valence band are extracted, creating holes that are balanced by anions from the electrolyte. If one electron is extracted, a radical cation species called polaron is formed. If a second electron is extracted from a polaron site, the radical species disappear and a bipolaron is formed (see Fig. 1.1). Colouration change is produced when polarons or bipolarons are formed in the polymer, so the knowledge of the distribution of both species is a key point to be considered.

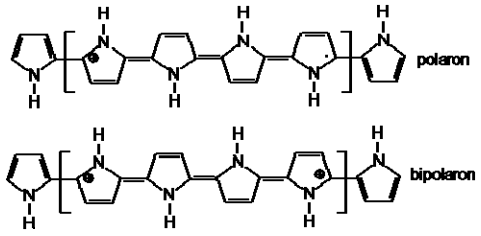

Fig. 1.1. Polaron and bipolaron species resulting from oxidation of polyaniline.

Viologen-modified nanostructured TiO_2 films present rapid switching between the bleached and coloured states, high contrast ratios and good cycling stability. Viologens (e.g. 1,1'-disubstituited 4,4'-bipyridinium dications) work as redox chromophores. The first reduction of the viologen dication is highly reversible and leads to the formation of the intensely deep blue coloured radical cation. The devices rely on the fast interfacial electron transfer between the nanocrystalline oxide and the adsorbed modifier as well as on the high surface area of the nanocrystalline support, which amplifies optical phenomena by two or three orders of magnitude. Studies of the electrical and optical response of these films can give light on the dynamics and kinetics of the colouration process in this system.

1.1 Summary outline

This thesis presents an analysis of the intercalation thermodynamics in a-WO_3 films by means of electrochemical methods. An interpretation of the electrochemical impedance and cyclic voltammetry results is given. A new model capable of describing the chemical capacitance variation at different film thicknesses based on distortions of the a-WO_3 lattice along intercalation is proposed. Diffusion of Li^+ ions in the material has been also discussed. In the conducting polymers field, an analysis of the voltammetric response is given by means of a Gaussian distribution of sites model capable of describing the polaron and bipolaron distributions in the material. The dynamic behaviour of viologen-activated nanostructured TiO_2 and the correlation between kinetics of charging and coloration has been studied. The main features observed in the electro-optical measurements can be satisfactorily explained and the viologen redox process can be separated from the overall response of the system. Finally, two electrochromic devices were fabricated as an example of application. The dissertation is organised as follows:

The remaining of chapter one presents the field of research. A survey of the importance of the chromogenic materials, their types and applications is given. Electrochromic materials are introduced in detail afterwards, considering the types and the state of the art of the applications where they are involved.

Chapter two describes the thermodynamic concepts that will be used in the development of the theoretical models proposed in the thesis. For the electrochemical potential a review of the existing models in the literature is given.

Chapter three shows the fundamentals of the electrochemical methods employed in

our study, such as electrochemical impedance, voltammetry and chronopotenciometry.

Chapter four presents the results of our research in amorphous WO_3 films. Sample preparation and the electrochemical measurements performed are explained. A detailed description of the impedance model which accurately accounts for the impedance spectra is given. Description of the shape of the voltammograms obtained is discussed as well. A thermodynamic model accounting for the chemical capacitance-composition variation at different thicknesses is presented. Volume changes variation of the films can be approximated by means of our model. Finally, a detailed study of the diffusion coefficient variation in the amorphous system is provided.

Chapter five is devoted to study the voltammetric response of conducting polymers. A review of the existing nernstian models for conducting polymers is given. These models are not able to explain the rather broadened peaks observed in the voltammograms, nevertheless a Gaussian distribution of energy sites is proposed, which provides a good fit to the first part of the oxidation peaks.

Chapter six analyses the contributions to the overall capacitive response in a viologen modified n-TiO_2 electrode. The change of the potential applied to the film controls the optical response, whose evolution can be explained properly considering the statistics of occupancy in the film.

In chapter seven two electrochromic devices based on a-WO_3 are constructed as an example. Description of the assembly and the performance is given.

Finally, chapter eight summarises the most important conclusions of our work.

1.2 Chromogenic materials

1.2.1 Importance and definition

The 21st century is being strongly conditioned by energetic aspects. If we have a look to the most serious problems occurring in the world today, many of them are related with energy (natural disasters, strategic wars, climate change, pollution, etc.). To maintain our standard of living, we are consuming more and more fossil fuel amounts, and every day that goes by, we are closer to the date where fossil resources will run out. The search for alternative and green energy sources is needed, and in fact, a lot of work is in progress (fuel cells, solar cells, supercapacitors, etc.).

Apart from clean energy sources, low-power consuming technologies are needed,

Fig. 1.2. Some of the most serious problems occurred in the world recently. All of them related with energy.

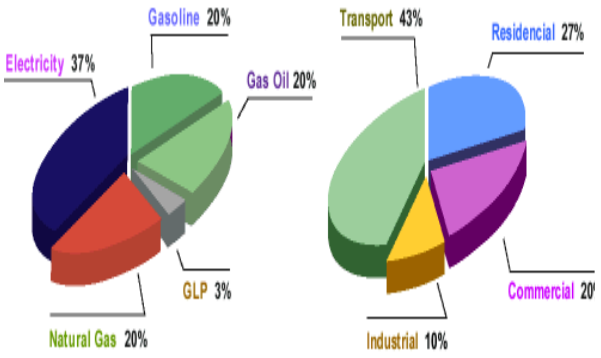

Fig. 1.3. Energy consumption in Barcelona in 1997 by energy sources (left) and activity sectors (right).

since when we produce energy, we damage nature. The production of electricity causes more damage to the environment than any other single human activity. Every energy use produces contamination or environmental problems. Even wind power, maybe the less contaminating energy source, perturbs the flight paths of birds, and many of them die when colliding with the wind machines, so it is very important to reduce our energy

consumption.

Two of the most typically consuming activity sectors in cities are transport and residential ones. The sum of both usually exceeds the 50% of the total energy consumed by a city, so it would be very helpful to lower the energy consumption in these sectors. To achieve that, different types of promising materials have appeared in the last years. One of them are the c*hromogenic materials*, which can provide us control over the amount of light and heat entering in a closed place, like buildings and vehicles, when they are incorporated in windows.

Approximately a 30% of the energy consumed in buildings could be saved, what implies a very important amount of money (more than $50 billion annually) as well. It is thought that in 2015, energy savings from advanced windows will allow us to avoid the emission of 71 million tons of CO_2, 157,000 tons of SO_2, and 142,000 tons of NO_x[1]. For that reasons, there is growing investment by companies and governments in promoting chromogenic technology[2]. It is expected that spectrally selective glazings (smart windows) will penetrate in the market in the following years[3].

A chromogenic material exhibits a large change in optical properties upon a change in an external stimulus (electrical field, light intensity, spectral composition, temperature and so on). The change in optical properties can be in the form of absorbance, reflectance, or scattering and can be either totally or partly over the visible and solar spectrum[2]. Depending on the stimulus applied to produce the optical change, there are several types of chromogenic materials: photochromics, thermochromics, phase dispersed liquid crystals, suspended particle systems and electrochromics are the most relevant.

1.2.2 Types of chromogenic materials and applications

Chromogenics cover any visibly switchable technology useful for glazing, mirrors, transparent displays, and a variety of other applications. Each different type of chromogenic material offer distinct performance features, offering a wide range of opportunities for different applications.

- *Photochromic materials:* They are one of the oldest switching materials. Photochromism occurs when the material changes its optical properties when exposed to the electromagnetic radiation, and revert to their original properties in the dark. Basically the phenomenon is the reversible change of a single chemical species between two energy states having different absorption spectra. This change is induced by electromagnetic radiation (usually UV light)[2]. For glazing there are two types of photochromic materials, the ones based on metal halides and the photochromic plastics. Of the inorganic materials, the best known commercial photochromic is photochromic eyeglasses[4]. They were first developed by Corning in the late 1960s and popularized by Transitions in the 1990s[5]. Photochromic lenses have a great amount of metal halide crystals (such as AgCl or AgBr) of about 15 nm in size embedded in them. When UV light illuminates the glass, the metal halide dissociates into metallic silver and the halide, causing a visible absorption to take place. When the UV light is removed, the metal halide molecule recombines thermally to its original transparent

Fig. 1.4. Corning Thin & Dark photochromic lenses reportedly change from clear to dark sunlens in a minute.

state. In the photochromic plastics field, certain dyes, stereoisomers and polynuclear aromatic hydrocarbons are involved. The most suitable glazing material in this class are the derivatives of spirooxazine applied to plastic[6]. Upon UV exposure, bond scission occurs in the molecule and a chromophore in the visible region forms as a result. Bond reformation takes place thermally and bleaching occurs when UV light is removed. Other photochromic inorganic materials are some metal oxides as tungsten and molybdenum oxides[7].

Photochromics are not considered as versatile as other chromogenic materials, such as electrochromics, because they cannot be manually controlled. Their performance requires consideration of temperature conditions as well as solar radiation. For example, inside a car, where most of the UV light is blocked out by the windshield, they do not work properly. Apart from their application in lenses, photochromics are suitable materials for radiation sensors, information storage devices, smart textiles, etc.

- *Thermochromic materials:* They show an optical change upon a change in temperature. Like photochromism, this phenomenon is one of the oldest of the chromogenic family. A large variety of substrates, such as organic[8] (spiroheterocycles, Schiff bases, bianthrones, etc.), inorganic[9] (VO_2, Fe_3O_4, AgI…), organometallic and macromolecular systems (e. g., polythiophenes) or supramolecular systems (such as liquid crystals) exhibit this behaviour. Thermochromic materials change colour by going through a thermally induced chemical reaction or by a phase transformation, causing scattering or multiple absorption of light. A large electronic change such as an insulator to semiconductor transition can also produce thermochromism. For glazing, these materials usually appear clear at lower temperatures, but become opaque at higher

temperatures. For that reason, they can be used for skylights, inclined glazing, and upper windows where view is not important. Most thermochromics are based on hydrogels[10], such as the polyether/ethylene oxide/carboxyvinyl polymer gel. 'Cloud Gel' by Suntek, a hydrogel film laminated between two pieces of glass, is the earliest

Fig. 1.5. ThermoSEE thermochromic glazing. The off-state is shown on the left and the heated on-state on the right (Pleotint, USA).

example of this type of films. A thermochromic called ThermoSEE has been introduced by US company Pleotint with an activation temperature range between -10ºC to 50 ºC. The technical problems with the gels are UV stability, cyclic lifetime, no manual control, and inhomogeneity during switching.

- *Phase dispersed liquid crystals:* The mechanism of optical switching in these materials is to change the orientation of liquid crystal molecules interspersed between two conductive electrodes with an applied electric field. Two sheets of transparent conductor-coated polyester or glass, serve as electrodes. The orientation of the molecules change with the field strength that alters the overall optical properties of the window, changing the glass between clear (on-state) and translucent (off-state). At

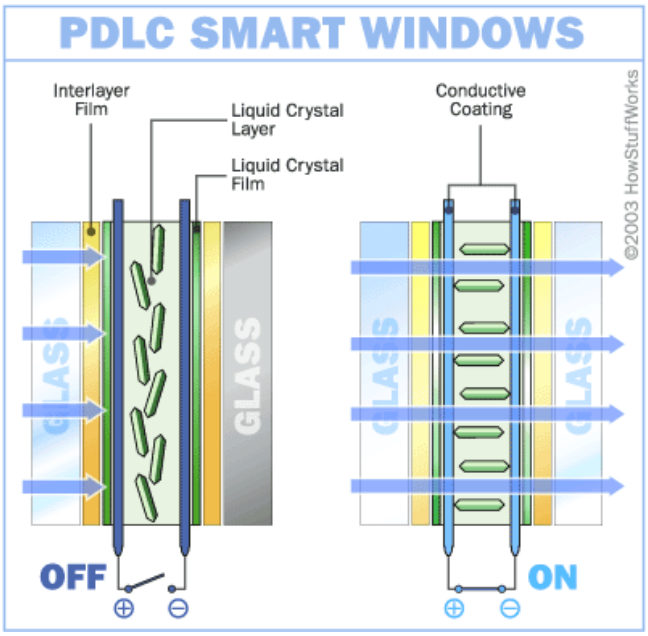

Fig. 1.6. How a phase dispersed liquid crystal (PDLC) window works. Orientation of the dispersed molecules is achieved upon application of an electric field.

times, dyes are added to darken the device in the off-state, which provides considerable control over visible transmittance compared with an undyed film[11]. Open circuit memory (conservation of optical properties when removing the electric field) is not possible with liquid crystals. Typically, these devices operate between 24-120 V and power consumption is less than 20 W/m^2. However, since the devices require continuous power to be clear, the power consumption is higher than for electrochromics. Nevertheless, a great advantage of these glasses is that switching is instantaneous.

Phase dispersed liquid crystals (PDLC) technology are among the most used chromogenic technology. It can already be found in offices and homes around the globe, but still some issues remain, such as long-term UV stability, haze permanence in the transparent state, and cost ($750-950/m^2). An important disadvantage is

Fig. 1.7. PDLC windows made by **SwitchLite Privacy Glass** in its on and off states.

that they don't reduce heating.

- *Suspended particle devices:* They are constructed using two panes of conductive glass separated by a suspension of light absorbing, microscopic particles. These particles are rod-shaped or plate-like and dispersed either in a liquid or in droplets encapsulated within a thin plastic film. In the 'off' state when no voltage is applied, the particles are suspended randomly and absorb light, making the glass unit non-transparent. When voltage is applied the particles align and permit light to pass through the film. An ac voltage (about 100 V) is required to prevent particle clustering. By simply adjusting the electrical voltage, manually or automatically, the amount of light passing through the window can be controlled quickly and with precision. Commercial development of these devices for goggles, eye glasses and windows is being done mainly by Research Frontiers Incorporated[12] and licensees. It is as durable as the glass within which it is enclosed (~10^8 cycles) and they have a fast switching response (fractions of seconds). This technology can be scaled to larger surface-area devices; because small currents are needed, the lateral voltage drops across the thin

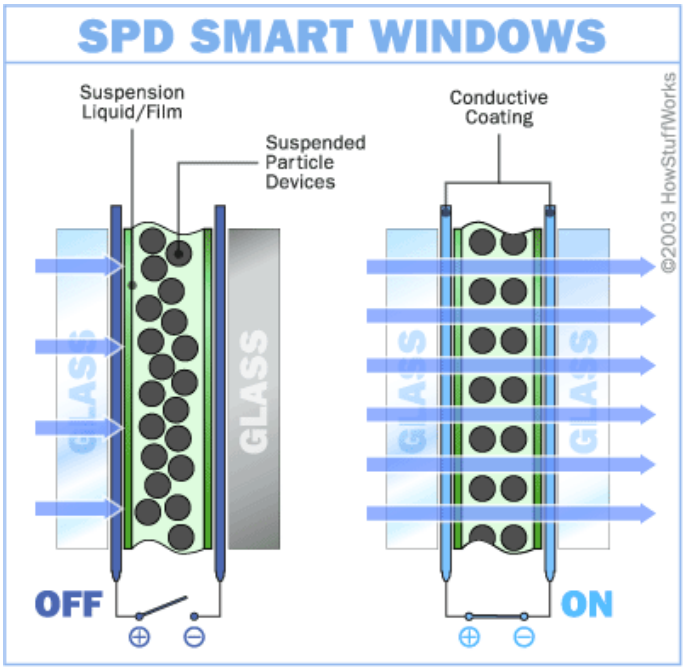

Fig. 1.8. How a suspended particle device (SPD) window works. Orientation of the dispersed molecules is achieved upon application of an electric field.

Fig. 1.9. Suspended particle device (SPD) car window by Research Frontiers Incorporated. Transparent (on-state) on the left and colored (off-state) on the right.

conducting layers are smaller and 'iris' effect is negligible. Due to the fact that they only use one active layer between two conducting layers, the fabrication is relatively easy and relatively inexpensive, their production costs are between $11 and $43 per square meter. Other applications available are rear-view mirrors (they offer a better response time and may prove to be less expensive than electrochromics) and sunroofs in cars and information displays.

- *Electrochromics:* Electhrochromism refers to the reversible change in optical properties when a material is electrochemically oxidized or reduced. It will be treated in more detail in the next section, but briefly we can say that the devices are usually composed by three layers: an ion storage film, the electrolyte, and the electrochromic layer. When a voltage difference is applied, electrons enter into the electrochromic layer and positive ions move towards the electrochromic material to keep charge neutrality. Different kinds of materials show electrochromism[13]. Transition metal oxides (WO_3, V_2O_5), viologens (1,1'-disubstituted-4,4'-bipyridinium dications) and conducting polymers are the more promising. A very important feature of these materials is that they show *memory effect*; when voltage is removed, coloration remains for quite a long time, so power is mainly needed only during switching. Voltage required to produce the

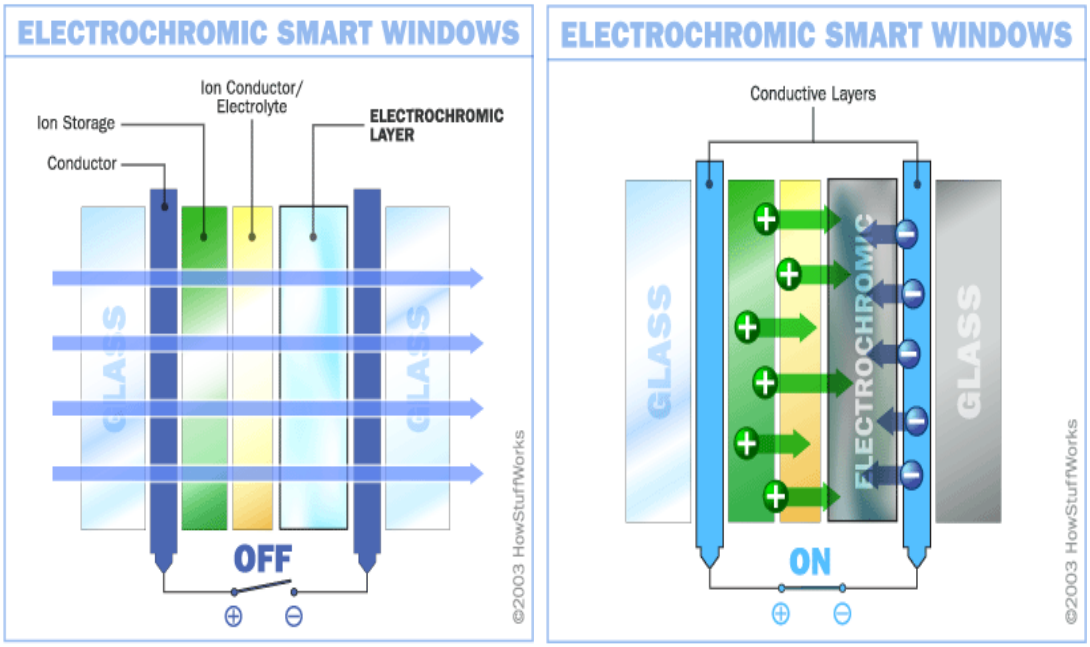

Fig. 1.10. How an electrochromic window works. Coloration occurs through an electrochemical reaction. Electrons are transferred into the electrochromic layer and ions intercalate at the same time to maintain electro-neutrality.

optical change is very low, usually 1-5 V. By controlling the voltage, gradual control of the coloration intensity is achieved. Because electrochromic devices depend on ion injection and chemical reactions, the process is inherently slow, typically in minutes for larger areas of glass. For example, it takes about 10 minutes to fully darken or bleach a ~1 m^2 pane of electrochromic glass. Few years ago, a new type of electrochromic device, called photoelectrochromic window, appeared[14]. The device incorporates an electrochromic layer in a dye-sensitised solar cell[15], thus the driving voltage needed for coloration is obtained when illuminated, so energy supply is not needed. The typical cycle lifetime is approximately 10,000 cycles for a large pane of architectural glass. If two cycles are applied per day, a lifetime

Fig. 1.11. Electrochromic window using WO_3 as electrochromic material.

of about 12 years is obtained. The production cost of electrochromic glass is estimated as $25 to $40 per square foot. Nowadays lots of companies are developing electrochromic devices[16] and several applications are already successfully used, as rear-view mirrors by Gentex, Magna Donnelly, etc.

- *Reflective hydrides:* These materials can be classified as electrochromics, but they are different in several ways from conventional electrochromics. They switch from transparent to reflective state (no absorbing state, as occurs in electrochromics) by injection of hydrogen from a gas or solid phase[17]. Optical change is quite spectacular as they change from a transparent glass into a mirror in a several milliseconds time. For that reason they are known as *switchable mirrors*. Metals (Y, Ln) or metal alloys (Mg-Ni, Gd-Mg) are the electrochromic materials that produce the optical change when hydrogenated. Discovery of this behaviour is very recent, it dates back to 1996[18], so development is still in progress. They offer interesting possibilities for smart windows, antireflection coatings for TV screens, rear-view mirrors and so on.

Fig. 1.12. Switchable mirror prototype showing transparent (above) and reflective (below) states.

From all the different chromogenic technologies described above, suspended particle devices and phase dispersed liquid crystals are the most used in the market. But electrochromism are the most promising, since they offer manual and gradual control of

the optical change and the voltage needed for switching is low and is not necessary to keep it applied after switching.

1.3 Electrochromic materials

1.3.1. Definition and historical aspects

The word electrochromic is a combination of electro (electricity) and chromic (colour). Chemical species that can be electrochemically switched between different colours are said to be electrochromic. Electrochromism results from the generation of different visible region electronic absorption bands on switching between redox states. Different kinds of materials, ranging from organic to inorganic, show electrochromism[13].

History of electrochromics dates back to 1704, when Diesbach discovered the chemical coloration of Prussian Blue, a hexacyanoferrate, that can be changed reversibly between deep blue and transparent states. In 1930 Kobosew and Nekrassow[19] found that tungsten oxide powders could be coloured blue by electrochemical reduction in acidic solution. A first step towards an electrochromic device was made by Talmey, who patented the coloration of particulate molybdenum and tungsten oxide layers. The first electrochromic device was made by Deb in 1969[20]. This paper marks the beginning of the scientific interest in electrochromic materials, and is widely cited usually in publications. By the mid-1970s, electrochromic devices were being developed for displays. Since its discovery in 1977[21], conducting polymers have attracted great interest as electrochromic materials[22], as they offer important advantages such as the possibility of being chemically modified, they are easily processable and simple to produce at low cost. Other organic compounds including viologens, metallopthalocyanines, etc. have received greater attention as well as electrochromics.

Electrochromics based on viologens and tungsten oxide followed in the 1980s for switchable mirrors in cars, which continues as a viable product to this day. In the 1990s, several companies began developing devices for glazing applications and the work still continues.

1.3.2. Electrochromic devices: Structure and deposition methods

There are different possible electrochromic device constructions; the most typically used is shown in Fig. 1.13, where three layers are assembled between two glass or plastic substrates. They are covered with a transparent conducting film, usually Indium Tin Oxide (ITO), F-doped SnO_2 (FTO) or Al-doped ZnO, where external circuit is contacted. In the internal part, the electrochromic compound (WO_3, conducting polymer or others) takes electrons from the substrate and intercalates ions from the ion conductor (organic or inorganic electrolyte). The ion storage film can be electrochromic or not. If it does, it should be complementary to the first electrochromic film.

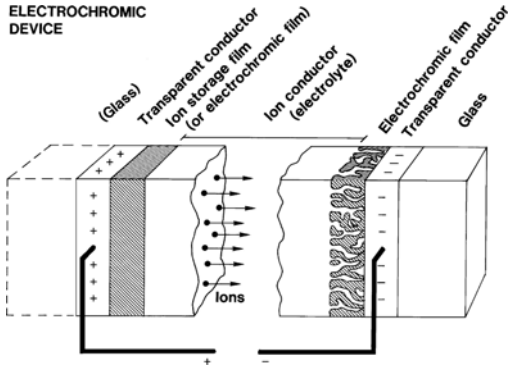

Fig. 1.13. Number of layers presented in a typical electrochromic device, as an electrochromic window.

A wide range of deposition techniques are available to deposit the layers of these devices[23], often leading to somewhat different film properties. In a chemical deposition method, a fluid precursor undergoes a chemical change at a solid surface, leaving a solid layer, whereas physical deposition uses mechanical or thermodynamic means to produce a thin film of solid. These both groups of techniques are typically used for metal oxides (SnO_2, WO_3…) deposition. Organic materials usually cannot bear high

temperatures, so other methods of deposition are employed in that case, such as doctor blade, spin coating, electrochemical techniques, and so on.

Evaporation methods belong to physical techniques where the film is produced by target vaporization under heating in vacuum. Thermal evaporation uses an electric resistance heater to induce evaporation. An electron beam impacts the compound to be deposited in an electron beam evaporator. Sputtering relies on a plasma (usually a noble gas, such as Argon) to knock material from a 'target'. Pulsed laser deposition systems work by an ablation process. Pulses of focused laser light vaporize the surface of the target material and convert it to plasma; this plasma usually reverts to a gas before it reaches the substrate.

In chemical deposition methods, a fluid precursor undergoes a chemical change at a solid surface, leaving a solid layer. Chemical vapor deposition is one of the most employed techniques, which uses a gas-phase precursor of the element to be deposited. When precursor is resistively heated, we are employing the hot-wire chemical vapor deposition method, which results very useful, since it is relatively cheap and produces homogenous films[24]. In a sol-gel process, the starting material is usually a metal liquid salt, 'sol', that after a spraying, transforms through hydrolysis or polymerization into a solid 'gel' phase. After final heat treatment, the film is formed. The spray pyrolysis process is a technique where a solution is sprayed onto a hot substrate and then decomposes to yield the desired film. The decomposition reaction (pyrolysis) is based in thermal decomposition of a compound to form the desired solid.

Electrochemical deposition can also be achieved when the electroactive precursor material is oxidised or reduced in an electrochemical cell.

1.3.3. Types of electrochromic materials and applications

A large number of electrochromic materials are available from all branches of synthetic chemistry. Here some of the most outstanding materials will be reviewed.

- *Transition metal oxides – WO_3:* Many transition metal oxides show electrochromism, such as V_2O_5, MoO_3, TiO_2, etc., but the most extensively studied material is by far the tungsten trioxide[23]. In this material coloration takes place when it is reduced and small metal ions (Li^+, H^+, Na^+…) are intercalated into the lattice.

$$W^{+6}O_3(colorless) + xM^+ + xe^- \longleftrightarrow M_xW_x^{+5}W_{(1-x)}^{+6}O_3(blue)$$

Coloration change is due to the new electronic transitions raised along the intercalation process, what is not well understood yet[25]. The rate limiting process of this reaction is usually the ion diffusion inside the metal oxide lattice, what slows down the switching time of the devices. Compared to other electrochromic materials, metal oxides have excellent durability, stability and reliability. However, they suffer from slow response times, narrow colour variation and high cost.

- *Conducting polymers:* In 2000, Shirakawa et al.[21] were awarded the Nobel Chemistry Prize for the discovery and developing of conducting polymers. All these polymers rely on a delocalised π-electron band structure and on increasing their conductivity when they are doped (oxidised or reduced). Upon doping, a new range of states appear in the gap region (polarons and bipolarons), leading to new electronic transitions that produce the optical change. An important property of conducting polymers is that they could be chemically modified easily, providing in that way

practically all the colours that we desire[26]. Polyaniline, polypyrrole and poly(3,4-ethylenedioxythiophene) are among the most employed conducting polymers. Compared to metal oxides they are inexpensive, easy to process, have high coloration efficiency, great amount of different colours availability and low fabrication cost. However, they show poor stability. Apart from their use in electrochromism, there are a very large amount of applications where they are involved, such as organic light emitting diodes, solar cells, batteries, sensors, etc.[27]

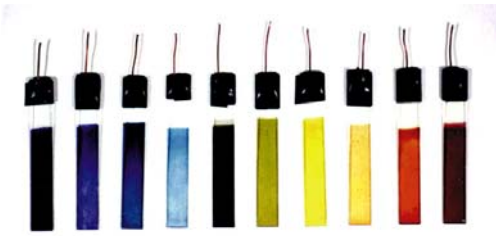

Fig. 1.14. Variable band gap conducting polymers demonstrating the range of accessible colours.

- *Viologens:* They are 1,1'-disubstituted-4,4'-bipyridinium dications. They change from colorless to deeply blue or green when reduced, leading to the radical coloured monocation formation. In the electrochromic devices they are used either dissolved in solution or attached to a nanoporous electrode such as TiO_2[28]. In these compounds, charge transfer reaction with the electrode is typically fast, leading to shorter switching time in devices. The most commercially successful electrochromic device so far is the rear-view mirrors from Gentex Corporation. They use two dissolved electrochromic compounds, one of them being a viologen, spaced between a transparent conducting glass and the metallic reflective surface, acting both as the electrodes. When redox processes take place after applying the voltage, viologen is reduced in the cathode and the other

Fig. 1.15. Electrochromic rear-view mirrors developed by Gentex (www.gentex.com).

electrochromic compound is oxidized in the anode, producing the coloured compounds, which diffuse to the bulk solution and react each other regenerating their original colorless state[13]. Compared to other electrochromics, they offer faster response times and good coloration efficiency. However, they are less durable and stable than metal oxides.

Nowadays, lots of companies are developing electrochromic glazing[16]. A great challenge is to make this technology, with low-cost fabrication techniques, in the $100-250/m^2 price range, but most of prototypes are currently above this value. ChromoGenics Sweden, the recently established company from Uppsala University, has developed a flexible electrochromic on plastic for visors on motorcycle helmets. Saint Gobain company is commercialising electrochromic sunroofs that have been used by Ferrari in its Superamerica model. SAGE and Apogee Enterprises are selling a ~1 m x

Fig. 1.16. Electrochromic displays by NTERA (left) offer an ink-on-paper readability at a competitive cost. In the middle, the electrochromic sunroof used in Ferrari Superamerica developed by Saint-Gobain. It changes from clear to almost black in about 60 seconds. Electrochromic SageGlass skylights are on the right.

0.6 m SageGlass switchable skylight. NTERA company has successfully developed electrochromic displays (NanoChromics) with low power consumption and high resolution at a competitive cost[29, 30] that could substitute the current liquid crystal technology used in clocks, thermostats and other devices. Gentex has incorporated electrochromic cabin windows in the new Boeing 787 Dreamliner aircraft, which is now being produced and whose first flight is planned for 2007[31]. In spite of these promising

applications, electrochromics are not well-established in the market yet. Several problems such as long switching times and *iris effect* (edges of window changing colour faster than the centre) due to voltage drops across the thin conducting layers, have to be improved yet. Price is another important issue, since it is in the range of 100-1,000$/m^2 and should lie in the 100-250$/m^2 region. Stability is poor, since devices typically show a lifetime of about 12 years that agrees for low-area applications (mirrors, displays) but not for windows in buildings.

1.4 References

(1) *http://eetd.lbl.gov/EA/mills/Lab2Mkt/Lab2Mkt.html*

(2) C. M. Lampert. *Proceedings of WIndow Innovations '95* (1995)

(3) E. S. Lee, D. L. DiBartolomeo, F. M. Rubinstein and S. E. Selkowitz. *Energy and Buildings* 36 (2004) 503.

(4) R. J. Araujo. *J. Non-Cryst. Solids* 47 (1982) 69.

(5) www.allaboutvision.com/lenses/photochromic.htm

(6) C. Nyc. *Solar Energy Materials* 14 (1986) 215.

(7) J. N. Yao, B. H. Loo, K. Hashimoto and A. Fujishima. *J. Electroanal. Chem.* 290 (1990) 263.

(8) J. H. Day. *Chem. Rev.* 63 (1963) 65.

(9) J. H. Day. *Chem. Rev.* 68 (1968) 649.

(10) H. R. Wilson. *Proceedings of the SPIE* 2255 (1994) 473.

(11) P. Vankonynenburg, S. Marsland and J. McCoy. *Solar Energy Materials* 19 (1989) 27.

(12) *http://www.refr-spd.com/*

(13) R. J. Mortimer. *Chem. Soc. Rev.* 26 (1997) 147.

(14) C. Bechinger, S. Ferrer, A. Zaban, J. Sprague and B. A. Gregg. *Nature* 383 (1996) 608.

(15) U. Opara Krasovec, A. Georg, A. Georg, V. Wittwer, L. Joachim and M. Topic. *Sol. Energy Mater. Sol. Cells* (2004)

(16) C. M. Lampert. *Materialstoday* 7 (2004) 28.

(17) R. Griessen. *Europhysics News* 32 (2001)

(18) Huiberts J.N., Griessen R., Rector J.H., Wijnaarden R.J., Dekker J.P., deGroot D.G. and K. N.J., *Nature* 380 (1996) 231.

(19) Kobosew N. and N. N.I., *Zeitschrift fur Elektrochemie* 36 (1930) 529.

(20) S. K. Deb. *Applied Optics* supp. 3 (1969) 192.

(21) H. Shirakawa, E. J. Louis, A. G. MacDiarmid, C. K. Chiang and A. J. Heeger. *Chem. Commun.* 578 (1977) 578.

(22) Argun A.A., Aubert P.H., Thompson B.C., Schwendeman I., Gaupp C.L., Hwang J., Pinto N.J., Tanner D.B., MacDiarmid A.G. and R. J.R., *Chem. Mater.*

16 (2004) 4401.

(23) C. G. Granqvist. *Handbook of Inorganic Electrochromic Materials*. Elsevier (1995).

(24) Mahan A.H., Parilla P.A., Jones K.M. and D. A.C., *Chem. Phys. Lett.* 413 (2005) 88.

(25) E. Avendaño, L. Berggren, G. A. Niklasson, C. G. Granqvist and A. Azens. *Thin Solid Films* 496 (2006) 30.

(26) B. L. Groenendaal, F. Jonas, D. Freitag, H. Pielartzik and J. R. Reynolds. *Adv. Mat.* 12 (2000) 481.

(27) J. Jagur-Grodzinski. *Polymers for advanced technologies* 13 (2002) 615.

(28) R. Cinnsealach, G. Boschloo, N. S. Rao and D. Fitzmaurice. *Sol. Energy Mater. Sol. Cells* 57 (1999) 107.

(29) D. Corr, U. Bach, D. Fay, M. Kinsella, C. McAtamney, F. O'Reilly, S. N. Rao and N. Stobie. *Solid State Ionics* 165 (2003) 315.

(30) http://0-www.spectrum.ieee.org.csulib.ctstateu.edu/jan06/2605

(31) http://www.ppg.com/gls_ppgglass/aircraft/22779.pdf

2. Thermodynamic and kinetic properties

2. Thermodynamic and kinetic properties

In this chapter several important thermodynamic and kinetic properties, such as electrochemical potential, capacitance, and diffusion coefficient, will be introduced. The understanding of these concepts is essential to be able to describe the thermodynamics of intercalation materials. Although many of these parameters are used in some other fields of research, it is important to overview its meaning in the electrochromic area.

2.1 Electrochemical potential

2.1.1 Definition

When a piece of apparatus measures the potential value V between two electrodes, what is actually measuring is the difference of the electrochemical potential $\bar{\mu}$ of the electron (Fermi level) between both electrodes[1], divided by the negative value of the elemental charge e,

$$V = -\frac{1}{e}(\bar{\mu} - \bar{\mu}_{CE}) \tag{2.1}$$

being $\bar{\mu}$ and $\bar{\mu}_{CE}$ the electrochemical potential of the electron in the working and counter electrode (or reference electrode if measuring in a three-electrode regime) respectively. To define the electrochemical potential it is necessary to introduce first the classical definition of electrostatic potential, that is,

$$\phi(x, y, z) = \int_{\infty}^{x,y,z} -\vec{E}d\vec{l} = \psi + \chi \tag{2.2}$$

the work done when the positive unit charge is moved from an infinite distance to a

point (x, y, z) in the interior of a phase. $\vec{E}$ and $d\vec{l}$ are the electric field and the displacement vectors respectively, the latter being infinitesimal and tangent to the trajectory. ψ is the *external potential*, that is defined as the electrostatic potential 'just outside' the surface. χ is the *superficial potential difference* due to the presence of oriented dipoles or to the inhomogeneous distribution of charge at the surface[2]. It should be noticeable that in all the interior points of a conducting phase (metal, electrolyte…) E =0 when no current is flowing, i.e., when there is no net movement of charge carriers. Under this consideration, the potential difference between any two points in the interior of the phase must also be zero. ϕ is also known as the *inner* or *Galvani potential* and is one of the elements that define the electrochemical potential.

In an α phase, for a species i, the electrochemical potential is defined as[2],

$$\bar{\mu}_i^{\alpha} = \mu_i^{\alpha} + z_i e \phi^{\alpha} \tag{2.3}$$

where z_i is the charge of i and μ_i^{α} is the chemical potential, which is defined as,

$$\mu_i^{\alpha} = \left(\frac{\partial G}{\partial n_i} \right)_{T,P,n_{j \neq i}} = \mu_i^{0\alpha} + k_B T \ln \left(\frac{a_i^{\alpha}}{a^0} \right) \tag{2.4}$$

being G the free energy, n_i the mole number of i, $\mu_i^{0\alpha}$ the standard chemical potential, T the temperature, P the pressure, a_i^{α} the activity of species i and a^0 the absolute activity, which equals to the unit value. Generally μ_i^{α} tell us how the free energy varies in phase α when only the amount of i species is changed.

In semiconductor physics is quite common to use the parallel concept of *Fermi level*, E_F, which appears in the Fermi-Dirac distribution $f(\varepsilon)$ that determines the probability of occupation of an energy state ε,

$$f(\varepsilon) = \frac{1}{1+\exp\left(\frac{\varepsilon - E_F}{k_B T}\right)} \tag{2.5}$$

and it is defined as the energy where the occupation probability is equal to 1/2. The Fermi level in a phase α is equal to the electrochemical potential of the electron in this phase[3],

$$E_F = \overline{\mu}_e^{\alpha} = \mu_e^{\alpha} - e\phi^{\alpha} \text{ (in eV).} \tag{2.6}$$

It is important to remark that E_F is always referred to the electrochemical potential of the electron and therefore it informs about how the free energy varies in phase α when

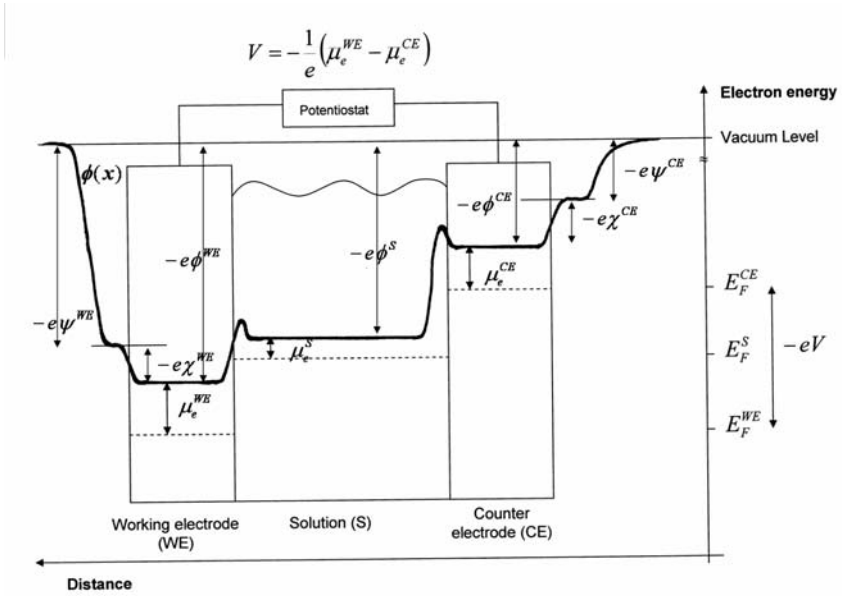

Fig. 2.1. Description of the different potentials that exist in the phases of a two-electrode electrochemical cell. $\phi(x)$ is defined by the thick line and Fermi levels (E_F) by the dotted lines. Profile of $\phi(x)$ is only tentative.

the number of electrons is changed.

As a summary, Fig. 2.1 shows all the contributions to the electrochemical potential of the electron in the diverse phases of an electrochemical cell.

2.1.2 Existing models in metal oxides

Depending on the system under consideration, the electrochemical potential can be described by different models. In an intercalation cell, the equilibrium of the system is achieved when the electrochemical potential of the intercalant species (Li^+ in our case) is equal in all phases of the system. Under this assumption, the cell voltage can be expressed by[4],

$$-eV = \mu_{Li^+} - \mu_{Li^+}^{CE} + \mu_e - \mu_e^{CE} = \Delta\mu_{Li^+} + \Delta\mu_e \qquad (2.7)$$

where the μ values without super index refers to the working electrode. So two contributions to the cell potential arise[4], the ionic $\Delta\mu_{Li^+}$ and the electronic $\Delta\mu_e$. Since the chemical potential of electrons and Li^+ does not change in the Li foil counter electrode, V can be described by the changes of the chemical potential of the ion and the electrons in the metal oxide, which both vary with the composition level x. In the case of using a-WO_3 as electrode, at low insertion levels ($x > 0.1$), the material possesses a high electronic conductivity, so can be considered that all the change in the cell potential is due to the variation of the chemical potential of Li^+ in the a-WO_3 electrode,

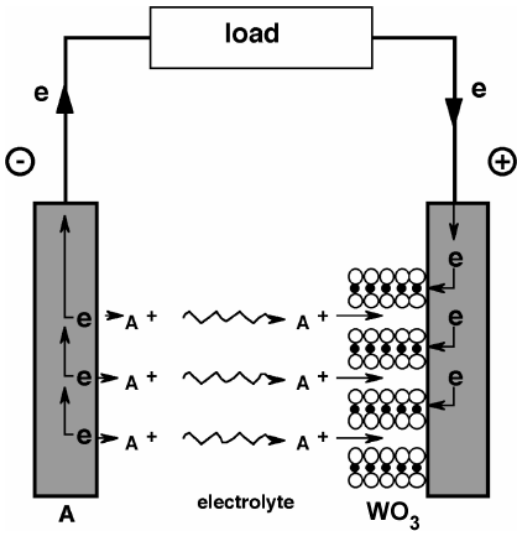

Fig. 2.2. Scheme of the intercalation cell Li/electrolyte/a-WO_3/ITO were measurements were taken. A corresponds to Li.

$$-eV(x) \propto (\mu_{Li^+}(x) - \mu_{Li^*}^{CE}). \qquad (2.8)$$

An intense researching activity has been carried out in the last years to explain the chemical potential function in metal oxides. As a first approximation, *lattice-gas*

models were employed[5]. This model considers that ions are distributed randomly in the host lattice in N equivalent sites of E_0 energy and they do not interact with one another, so the chemical potential is expressed as,

$$\mu(x) = E_0 + k_B T \ln\left(\frac{x}{1-x}\right) \tag{2.9}$$

where k_B is the Boltzman constant. If interactions between ions are taken into account, the simplest way is add a term to this equation, supposing that ions remain randomly arranged, if U is the total interaction energy that a given ion would feel if all the other sites were full, when only a fraction x of the sites is occupied, the interaction would be Ux, thus

$$\mu(x) = E_0 + k_B T \ln\left(\frac{x}{1-x}\right) + Ux. \tag{2.10}$$

This is often called a mean-field approximation; each ion feels the mean interaction from its neighbours. This equation has been used to understand intercalation systems[6], but an accurate description is not easy to find. Berlinsky et al.[7] reported the first quantitative experimental description using this model in $Li_xMo_6Se_8$. Levi et al.[8] used a similar approach in Li_xCoO_2 but taking into account kinetic aspects. Strømme Mattsson[9] applied the lattice-gas model in crystalline WO_3 obtaining good results. A problem rising from mean-field approximation is that only long-range interactions between intercalants can be taken into account, so it fails when short-range interactions are relevant. Nevertheless, Monte Carlo

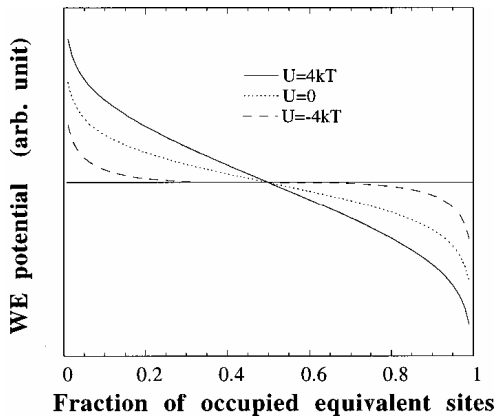

Fig. 2.3. Evolution of the mean-field lattice-gas model at different interaction parameter values. At U =0, simple lattice-gas is obtained.

simulations provide a suitable description in these cases[10, 11]. In amorphous materials usually voltage decreases steeper along composition than in their crystalline counterparts. If we use a mean-field lattice-gas model for description, we obtain very high U values (>1 eV), two or three times larger than those related with crystalline compounds, what is difficult to understand. Trying to solve this problem, Kudo and Hibino[12] proposed a new model arguing a distribution of site energies, what is likely to take place in an amorphous material. An expression for the chemical potential based on a Gaussian distribution was proposed. This model fits satisfactorily $\mu(x)$ in amorphous a-WO_3 but fails when trying to account for other features like the variation of the capacitance vs. composition slope at different film thicknesses[13].

Another important aspect occurring in intercalation materials is that the host lattice becomes distorted along intercalation[14]. Vakarin et al.[15] introduced this issue in the lattice-gas model description. They combined it with linear elasticity theories allowing to obtain a quantitative description of various insertion processes[16]. This model will be described in the following lines in a more extended way, since it will be compared with our results in the next chapter.

2.1.3 Lattice gas model considering lattice distortions

As a first step, the free energy F consisting on three terms is calculated[16],

$$F = F_H + F_G(x) + F_{el}(x). \qquad (2.11)$$

The first term involves the host free energy in the absence of intercalation. F_G is the guest free energy for a rigid lattice, which can be calculated using simple lattice gas statistics. F_C is the elastic part and describes the coupling between the host and the intercalant. This term is difficult to calculate since real host materials have rather

complicated elastic properties, so it is estimated on the basis of the continuum theory of elasticity with concentration dependent stress and strain fields. It is approximated by the free energy of a strained isotropic body under a loading stress $\sigma(x)$ and assuming that the strain $\varepsilon(x)$ is purely dilatational,

$$F_{\mathrm{el}}(x) = \frac{1}{2}\Lambda\varepsilon(x)^2 - \sigma(x)\varepsilon(x). \tag{2.12}$$

Λ represents an effective, concentration-independent elastic constant and $\sigma(x)$ finally corresponds to loading stress resulting from other mechanisms different than dilatation. The total stress $S(x) = \mathrm{d}F_{\mathrm{el}} / \mathrm{d}\varepsilon$ conveys then two terms

$$S(x) = \Lambda\varepsilon(x) - \sigma(x), \tag{2.13}$$

the internal, or self-stress, $\Lambda\varepsilon(x)$ accounts for the host reaction to the intercalant insertion, and the stress resulting from the loading procedure, $\sigma(x)$.

The guest chemical potential is given by the concentration derivative of the total free energy, which in addition to the term derived from simple lattice gas statistics $\mu_0 = E_0 + \beta^{-1}\ln(x/1-x)$ should contain the elastic contribution[16],

$$\mu = \mu_0 + \Lambda S(x)\frac{\mathrm{d}\varepsilon(x)}{\mathrm{d}x} - \frac{\mathrm{d}\sigma(x)}{\mathrm{d}x}\varepsilon(x), \tag{2.14}$$

being $\beta^{-1} = k_B T$ the thermal energy. The second term involves the so-called chemical expansion coefficient $\mathrm{d}\varepsilon/\mathrm{d}x$, whereas the last term is associated with the loading path. The strain is related to the volume variation by the expression[17]

$$\varepsilon(x) = \frac{V(x) - V(0)}{V(0)} = \delta p(x), \tag{2.15}$$

being $\delta = [V(1) - V(0)]/V(0)$ and $p(x) = [V(x) - V(0)]/[V(1) - V(0)]$. A special case can be described if we consider the vanishing of the loading stress $\sigma(x)$ =0, as in an unclamped film, arriving at

$$\mu = E_0 + \beta^{-1} \ln \frac{x}{1-x} + \Lambda \delta^2 p(x) \frac{\mathrm{d}p(x)}{\mathrm{d}x} . \qquad (2.16)$$

In general this model allows us to relate the chemical potential variation of the guest in the host lattice with the elastic properties of the system, which typically undergoes a volume variation along the intercalation process.

2.1.4 Existing models in conducting polymers

In conducting polymers the electrochemical potential function have been described using the similar concepts than the ones argued in the lattice gas models, i.e., considering distributions and interactions of polaron and bipolaron species[18-22]. The simplest model for a single energy, non-interacting species gives the Nernst equation (Langmuir isotherm). Interactions are often treated in the mean-field approximation corresponding to the Frumkin isotherm[23]. A review of the nernstian models applied to conducting polymers will be presented in Sec. 5.2.

2.2 Capacitance

Capacitance is an important concept in electrochemistry. It is used when an accumulation of charge takes place in a phase. Depending on the nature of the phase and how the charge is distributed when accumulated, we can describe several kinds of capacitances.

- *Capacitance (electrostatic concept):* In a parallel-plate capacitor, capacitance C describes the faculty of accumulate charge Q when the voltage V between its plates is varied.

$$C = \frac{Q}{V} = \frac{\varepsilon A}{d} \tag{2.17}$$

being ε the dielectric permittivity, A the area of one of the plates and d the distance between them. In a capacitor of this kind, capacitance is only dependent on the geometry (A, d) and on the nature of the dielectric (ε). All these parameters do not change, so C is always constant in a capacitor.

- *Helmholtz capacitance (C_H):* Helmholtz model is the simplest one to describe the double layer that is formed in the electrode/electrolyte interface[24]. In this model when a charge Q is accumulated in the surface of the electrode, a plane of charge $-Q$ appears in the electrolytic solution for compensation. This looks like a parallel-plate capacitor, and the capacitance of the interface can be described using Eq. (2.17). C_H is usually in the μFcm^{-2} range and does not tend to vary a lot with potential.

- *Redox capacitance (C_r):* When there is charge transfer between the electrode and a redox couple, the charge passes to the redox species where in some way it is accumulated, leading to a capacitance of electrochemical character, instead of electrostatic. Actually, the redox capacitance is a pseudo-capacitance, which can be measured by means of electrochemical techniques[25]. In a redox reaction like this,

$$Ox(solution) + 1e^{-}(electrode) \leftrightarrow \mathrm{Re}\,d(solution)$$

redox capacitance per volume unit is defined as[18],

$$C_r = eF\frac{dc_{red}}{d\bar{\mu}} = \frac{eFc_{tot}}{k_BT}x(1-x) \qquad (2.18)$$

where F is the faraday constant, c_{red} and x are the concentration and molar fraction of the reduced species respectively, $c_{tot} = c_{ox} + c_{red}$ is the overall concentration of species and $\bar{\mu}$ is the Fermi level in the electrode, proportional to the redox potential V_{redox}, which is given by the Nernst equation,

$$\bar{\mu} = -eV_{redox} = \mu_{redox}^{0'} + k_BT\ln\frac{x}{1-x} \qquad (2.19)$$

where $\mu_{redox}^{0'} = \mu_{red}^{0} - \mu_{ox}^{0}$ is the formal chemical potential. Unlike the Helmholtz capacitance, which does not usually vary a lot along potential, the nernstian redox capacitance shows a bell shape with a maximum value $eFc_{tot}/(4k_BT)$ at x=0.5, that corresponds to the formal potential $V_{redox}^{0'} = -\mu_{redox}^{0'}/e$.

- *Chemical capacitance (C_μ):* When a material different from a metal is used as electrode, specially a semiconductor (WO_3, TiO_2…), if the Fermi level E_F (or $\bar{\mu}$) is changed, charge carriers are accumulated inside the material when no charge transfer occurs, originating a capacitance that depends on the *chemical* nature of the electrode.

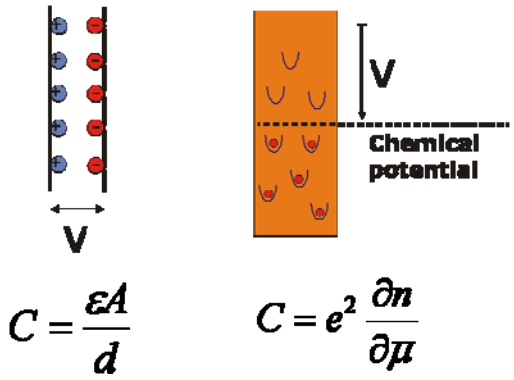

Fig. 2.4. Comparison of the capacitance (left) and chemical capacitance (right) concept.

The accumulated charge can be balance in different ways, such as intercalation of ions, charging of the electrode/electrolyte double layer, etc. The chemical capacitance can show different trends upon potential, for example in nanoporous TiO_2 it is shown an exponential variation[26]. C_μ is given, per volume unit, by,

$$C_\mu = e^2 \frac{dn}{d\bar{\mu}} \tag{2.20}$$

being n the density of charge carriers. Normally it depends on the density of states in the material, which probability of occupancy is generally given by the Fermi-Dirac distribution[27].

In the batteries researching field, it is often to find the term *capacity*, but it is not related with a capacitance, since it is referred to the amount of energy that a battery can store and it is measured in amperes by hour (Ah).

2.3 Diffusion coefficients

Most of the electrochromics, like metal oxides and conducting polymers, are intercalation materials, i.e., they balance the charge excess by intercalating ions in their structure. The intercalants can diffuse inside the lattice of the host. Typically this process is slow and often is the limiting process of the coloration change in the devices.

A species diffuses when there is a gradient in chemical potential, going from the high chemical potential region to the lower. In accordance with Fick's first law, the mole number of a species i that crosses in the x direction, a normal surface in the time unit, i.e., the flux J_i, is defined as[24],

$$J_i = -D_{ch}\frac{\partial C_i}{\partial x} \tag{2.21}$$

being C_i the concentration of species i and D_{ch} the chemical diffusion coefficient. The real driving force leading the diffusion is the chemical potential difference, for that reason the flux is also defined as[28],

$$J_i = -L_0\frac{\partial \mu}{\partial x} \tag{2.22}$$

and hence,

$$D_{ch} = L_0\frac{\partial \mu}{\partial C_i} \tag{2.23}$$

being L_0 a coefficient and is $\partial\mu/\partial C_i$ which accounts for the difference between a concentration and a chemical potential gradient respectively.

Regarding a microscopic approach, D_{ch} can be described using the Green-Kubo theory[29], where the flux J_i is defined as,

$$J_i = \sum_{i=1}^{n} v_i(t) \tag{2.24}$$

being v_i the velocity of diffusion of i, n the total number of particles per volume unit and t the time. In this approach D_{ch} is defined as,

$$D_{ch} = \chi_T D_J \tag{2.25}$$

where χ_T is the *thermodynamic factor*, that accounts for the difference between concentration and chemical potential gradient[30]. It is given by,

$$\chi_T = \frac{\partial(\mu / k_B T)}{\partial \ln x}. \tag{2.26}$$

D_J is the *jump diffusion coefficient* which describes the movement of the intercalant from one site of the lattice to another (hopping)[31]. It is defined by,

$$D_J = \Gamma l^2 \tag{2.27}$$

being Γ the average frequency of hopping and l the distance between neighboring sites. D_J is related to the displacement of the center of mass of all the diffusing ions, and can be also given by,

$$D_J = \lim_{t\to\infty}\left[\frac{1}{2dt}\left\langle \frac{1}{N}\left(\sum_{i=1}^{N}\vec{r}_i(t)\right)^2\right\rangle\right]. \tag{2.28}$$

N corresponds to the number of diffusing ions, $\vec{r}_i(t)$ is the displacement of the ith ion after time t, and d is the dimension of the lattice on which diffusion takes place. D_J does not account for the interactions between the intercalated particles, what alter the diffusion process specially when their number is high. The parameter accounting for that is the thermodynamic factor χ_T that takes a similar role to the activity coefficient that equals one in diluted solutions, where interactions between particles are weak.

In metal oxide lattices, diffusion of cations, typically Li^+, Na^+ and H^+, takes place by hopping from one site to another. Van der Ven et al.[30] reported a theory of ionic

diffusion applied to Li_xCoO_2. A strong dependence of the chemical diffusion coefficient on composition is well documented[32], although nearly constant values have been also reported[33] for WO_3. The differences among the distinct values obtained rise mainly from the dependence on deposition conditions[32]. In this thesis we analyse in chapter 3 the variation of diffusion constant for lithium insertion into a-WO_3 prepared by electron beam evaporation technique. A decrease of several orders of magnitude along composition is obtained, what matches with an increase of the hop activation barrier.

2.4 References

(1) I. Riess. *Solid State Ionics* 95 (1997) 327.

(2) N. Sato. *Electrochemistry at Metal and Semiconductor Electrodes*. Elsevier (1998).

(3) H. Reiss. *J. Phys. Chem.* 89 (1985) 3783.

(4) H. Gerischer, F. Decker and B. Scrosati. *J. Electrochem. Soc.* 141 (1994) 2297.

(5) W. R. Mckinnon.Solid State Electrochemistry, *Insertion electrodes I: Atomic and electronic structure of the hosts and their insertion compounds*. Cambridge University Press (1995).

(6) A. J. Berlinsky, W. G. Unruh, W. R. McKinnon and R. R. Haering. *Solid State Commun.* 31 (1979) 135.

(7) S. T. Coleman, W. R. McKinnon and J. R. Dahn. *Phys. Rev. B* 29 (1984) 4147.

(8) M. D. Levi, G. Salitra, B. Markovski, H. Teller and D. Aurbach. *J. Electrochem. Soc.* 146 (1999) 1279.

(9) M. S. Mattsson. *Phys. Rev. B* 58 (1998) 11015.

(10) S. W. Kim and S. I. Pyun. *Electrochim. Acta* 46 (2001) 987.

(11) R. Darling and J. Newman. *J. Electrochem. Soc.* 146 (1999) 3765.

(12) T. Kudo and M. Hibino. *Solid State Ionics* 84 (1996) 65.

(13) J. García-Cañadas, F. Fabregat-Santiago, I. Porqueras, C. Person, J. Bisquert and G. Garcia-Belmonte. *Solid State Ionics* 175 (2004) 521.

(14) J. E. Fischer and H. J. Kim. *Phys. Rev. B* 35 (1987) 3295.

(15) E. V. Vakarin, J. P. Badiali, M. D. Levi and D. Aurbach. *Phys. Rev. B* 63 (2000) 014304/1.

(16) E. V. Vakarin and J. P. Badiali. *J. Phys. Chem. B* 106 (2002) 7721.

(17) E. V. Vakarin and J. P. Badiali. *Solid State Ionics* 171 (2004) 261.

(18) C. E. D. Chidsey and R. W. Murray. *J. Phys. Chem.* 90 (1986) 1479.

(19) M. A. Vorotyntsev and J. P. Badiali. *Electrochim. Acta* 39 (1994) 289.

(20) G. Paasch, P. H. Nguyen and A. J. Fischer. *Chem. Phys.* 227 (1998) 219.

(21) M. A. Vorotyntsev and J. Heinze. *Electrochim. Acta* 46 (2001) 3309.

(22) D. Posadas, R. M. J. Presa and M. I. Florit. *Electrochim. Acta* 46 (2001) 4075.

(23) M. D. Levi and D. Aurbach. *Electrochim. Acta* 45 (1999) 167.

(24) A. J. Bard and L. R. Faulkner. *Electrochemical Methods, Fundamentals and Applications*. John Wiley and sons (1980).

(25) B. E. Conway. *Electrochemical supercapacitors*. Plenum Publishing (1999).

(26) F. Fabregat-Santiago, I. Mora-Seró, G. Garcia-Belmonte and J. Bisquert. *J. Phys. Chem. B* 107 (2003) 758.

(27) J. Bisquert. *Phys. Chem. Chem. Phys.* 5 (2003) 5360.

(28) L. Onsager and R. M. Fuoss. *J. Phys. Chem.* 36 (1932) 2689.

(29) C. Uebing and R. Gomer. *J. Chem. Phys.* 95 (1991) 7626.

(30) A. van der Ven, G. Ceder, M. Asta and P. D. Tepesch. *Phys. Rev. B* 64 (2001) 184307.

(31) G. Garcia-Belmonte, V. S. Vikhrenko, J. García-Cañadas and J. Bisquert. *Solid State Ionics* 170 (2004) 123.

(32) C. G. Granqvist. *Handbook of Inorganic Electrochromic Materials*. Elsevier (1995).

(33) M. S. Mattsson. *Solid State Ionics* 131 (2000) 261.

3. Electrochemical methods

3.1 Cyclic voltammetry

3.2 Electrochemical impedance

3.3 Chronopotenciometry

3. Electrochemical methods

In this chapter the electrochemical techniques that have been used in our work will be introduced. In general, every electrochemical method consists on applying a perturbation to the system and registering the response observed. Different information about the system is provided depending on the method employed.

3.1 Cyclic voltammetry

It is the most employed electrochemical technique. Typically measurements are taken in a three-electrode electrochemical cell. The perturbation is applied in the working electrode. The reference electrode provides a constant potential, which is used as reference. The counter electrode completes the electric circuit.

This technique consist on applying a linear variation of the potential in the system, starting at an initial potential V_0, arriving at a potential vertex V_1 and returning again to

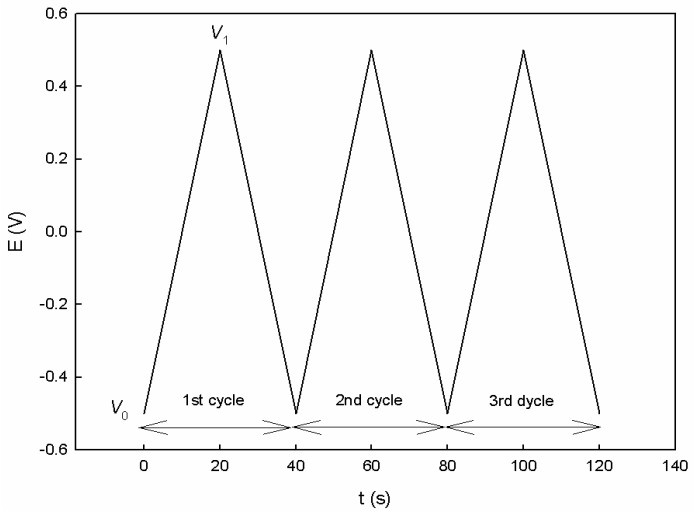

Fig. 3.1. Perturbation applied along a cyclic voltammetry experiment comprising 3 cycles. Voltage follows a linear change $V = V_0 \pm st$.

the initial point. This combination comprises a voltammetric cycle. The voltage is varied at a constant rate s, typically in the 1-100 mV/s range.

The response obtained is the variation of the current I vs. the applied potential. A few examples of different responses that can be obtained are given in Fig. 3.2. In the left

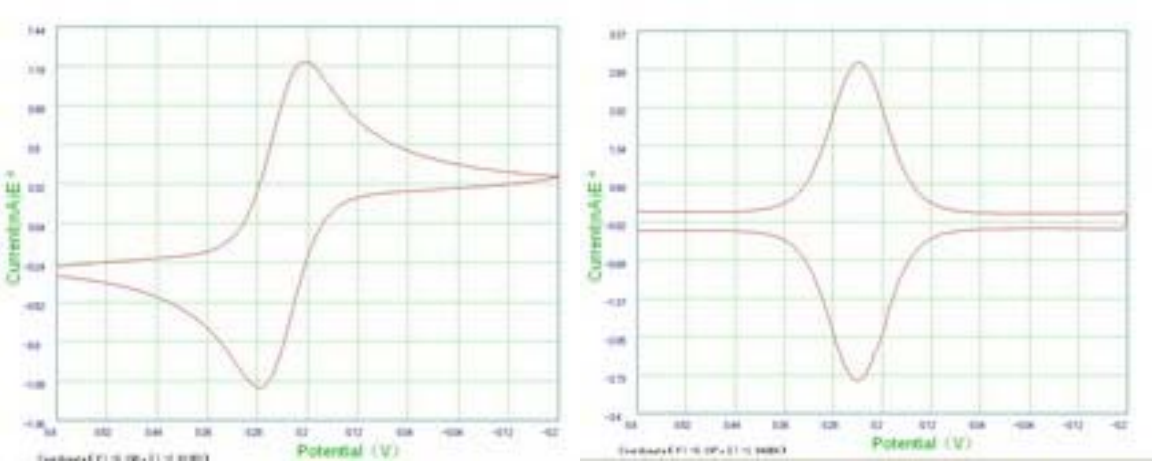

Fig. 3.2. Two typical cyclic voltammograms corresponding to a simple redox reaction with the species in solution (left) or adsorbed over the electrode (right).

part the cyclic voltammogram (CV) corresponds to a simple redox reaction $Ox + ne^- \leftrightarrow \mathrm{Re}\,d$ where both Ox and $\mathrm{Re}\,d$ are in solution. The current does not tend to zero after the peak due to the diffusion of the species. On the right part the electroactive species are deposited over the electrode, so they cannot diffuse and a nearly symmetrical response is observed. It is worth mentioning the rectangular response observed in the CV on the right out of the area where the peaks appear. This response is due to the charging-discharging of the double layer electrode/electrolyte (Helmholtz capacitance).

3.2 Electrochemical impedance

Electrochemical impedance technique consists on applying an oscillating potential (ac potential) with low amplitude V_0 in the electrochemical system at a certain frequency ω, that oscillates around a fixed value V_{dc} (dc potential). By using low amplitude, in the order of few milivolts, we assure a voltage-current linear relationship and hence obtaining an oscillating current response with a phase ϕ and amplitude I_0. The experiment is performed in a frequency range, calculating at each frequency the ratio between voltage and current, i.e., the impedance $Z = V/I$, that is represented in the complex plane, where V, I and Z take the expressions

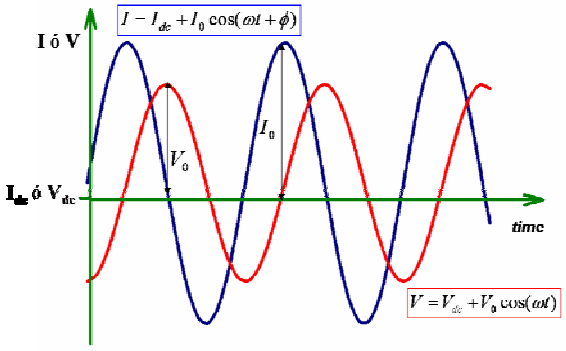

Fig. 3.3. Applied voltage (red) and registered current (blue) at a certain frequency.

$$V = V_0 e^{i\omega t}, \tag{3.1}$$

$$I = I_0 e^{i\omega t} e^{i\phi}, \tag{3.2}$$

and

$$Z = \frac{V}{I} = \frac{V_0}{I_0} e^{i\phi}, \tag{3.3}$$

where $i = \sqrt{-1}$ is the imaginary unity.

The resulting collection of points at different frequencies forms the impedance spectrum. Interpretation of the spectra is usually obtained by means of an equivalent circuit, formed by the combination of circuit elements such as resistors, capacitors,

constant phase elements (CPEs), etc. Depending on the elements and how they are

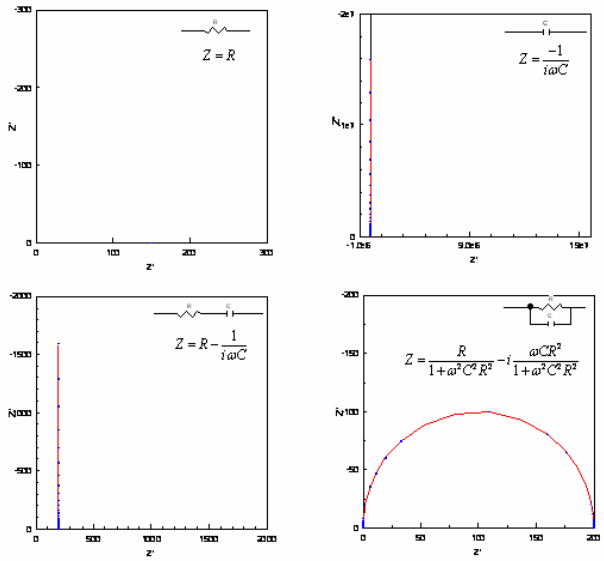

Fig. 3.4. Electrochemical impedance spectra obtained for different elements (resistor and capacitor) and different equivalent circuits (resistor and capacitor in series and parallel respectively). Analytical expressions of the impedance functions are given for each case.

combined (series or parallel) different spectra can be obtained. Some of the most frequent circuit elements and equivalent circuits are described in Fig. 3.4. Each of the elements comprising an equivalent circuit describes a physic phenomenon that occurs in the system. Usually several equivalent circuits are able to fit to the experimental impedance spectrum properly, but an accurate description of the physical processes involved must be given to obtain the right one.

The main advantage in the use of the impedance technique is that you can easily distinguish and separate all the processes that are taking place in the electrochemical system. Moreover, a quantitative calculation of the main properties of the system (charge transfer resistances, capacitances, transport phenomena, etc.) and how they vary along potential can be obtained.

3.3 Chronopotenciometry

This method applies a constant current to the working electrode during certain time. The response registered is the evolution of the voltage along time. This technique is frequently used for electropolymerisation of conducting polymers (see Fig. 3.5 as an example).

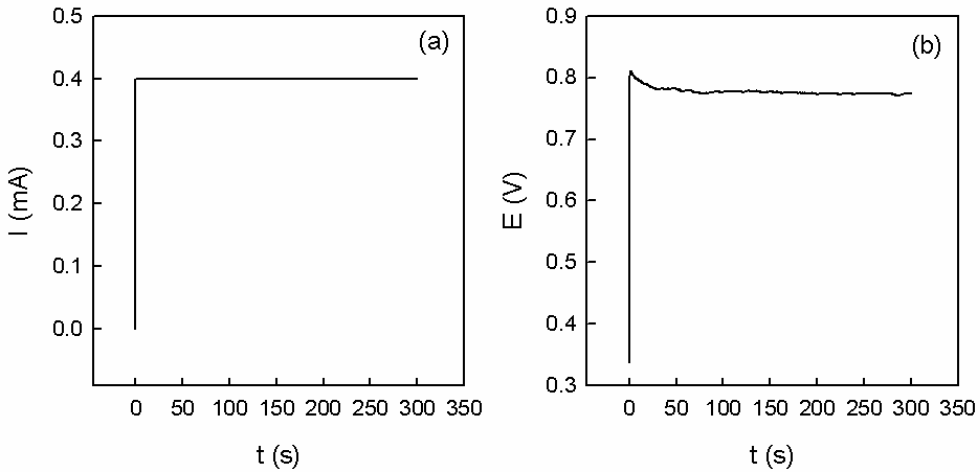

Fig. 3.5. Chronopotenciometry experiment performed at 0.4 mA constant current for polimerisation of pyrrole. (a) Corresponds to the perturbation applied and (b) is the registered response.

Generally the voltage of the working electrode increases quickly until the value where the electrochemical reaction is produced. At that point the voltage remains nearly constant till the electroactive species are consumed. This technique is also useful to study the thermodynamics of charging and discharging in electrodes that form part of batteries, such as metal oxides, when low enough currents are employed, what establish quasi-equilibrium conditions.

4. Tungsten oxide: a-WO_3

4. Tungsten oxide: a-WO_3

We performed an in-depth electrochemical study of amorphous tungsten oxide, a-WO_3, in order to understand properly the intercalation thermodynamics in this material. In general, studies about the amorphous oxide are less frequent in the literature. Crystalline oxides typically are able to accumulate bigger amount of charge and experiment phase transformations along the intercalation process, what makes their study a bit more complex. They are preferably used in batteries. On the other hand, amorphous oxides are easier to process when preparing the devices and are more usually focused in the electrochromic field.

4.1 Experimental part

4.1.1. Sample preparation

a-WO_3 films were prepared by electron beam evaporation technique with a Leybold APS 1104 machine (Fig 4.2) on B270 'Superwite' Schot glass as substrate. In a vacuum chamber, a high voltage is applied to a tungsten filament what causes electrons to be discharged. The stream of electrons emitted excites the targeted solid

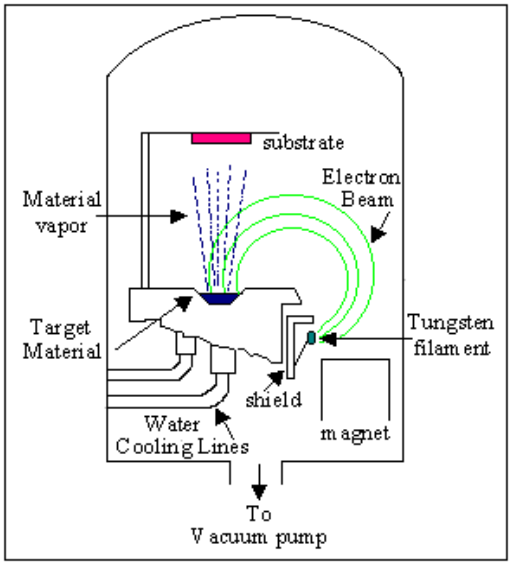

Fig. 4.1. Description of an e-beam evaporator.

Fig. 4.2. Electron beam evaporator used in the preparation of our samples.

and turns it into vapour, which travels to the substrate. As they reach the surface, they condense and form a thin film coating. The layout of the samples was glass/ITO (indium tin oxide)/a-WO_3. The ITO layer was deposited at 150 ºC of substrate temperature to make the glass conducting. The starting material was 99.99% pure In_2O_3-SnO_2 from Cerac, with molar ratio 91%-9%. The sample was grown up to a thickness of 300 nm, controlled by a QSM (quartz crystal system). The deposition rate was automatically controlled and kept at 0.3 nm/s. In order to achieve a low sheet resistance, ion bombardment assistance was provided by a built-in APS system (Advance Plasma Source). The ITO layers presented a sheet resistance of 15 Ω/□ with a luminous transmittance higher than 89%. The a-WO_3 layers were grown on the ITO-coated glass at 125 ºC of surface temperature. The starting material was 99.99% pure WO_3 from Cerac. An oxygen flow of 40 sccm was employed and the samples were deposited without ion bombardment. The sample thicknesses were between 100 and 400 nm, at a growth rate of 0.3 nm/s, confirmed by profilometry techniques. a-WO_3 layers of high density, 7.16 g cm^{-3} resulted.

To prove the amorphous nature of the deposited WO_3 layer, x-ray diffraction experiments were performed in samples of different thicknesses using a Siemens D-5000 diffractometer with Bragg-Brentano geometry. The divergence, anti-scattering, monochromator and detector slits were 2, 2, 0.2 and 0.6 mm respectively. The spectra were obtained using steps of 0.05º with a step time of 3 s. All of the spectra showed a

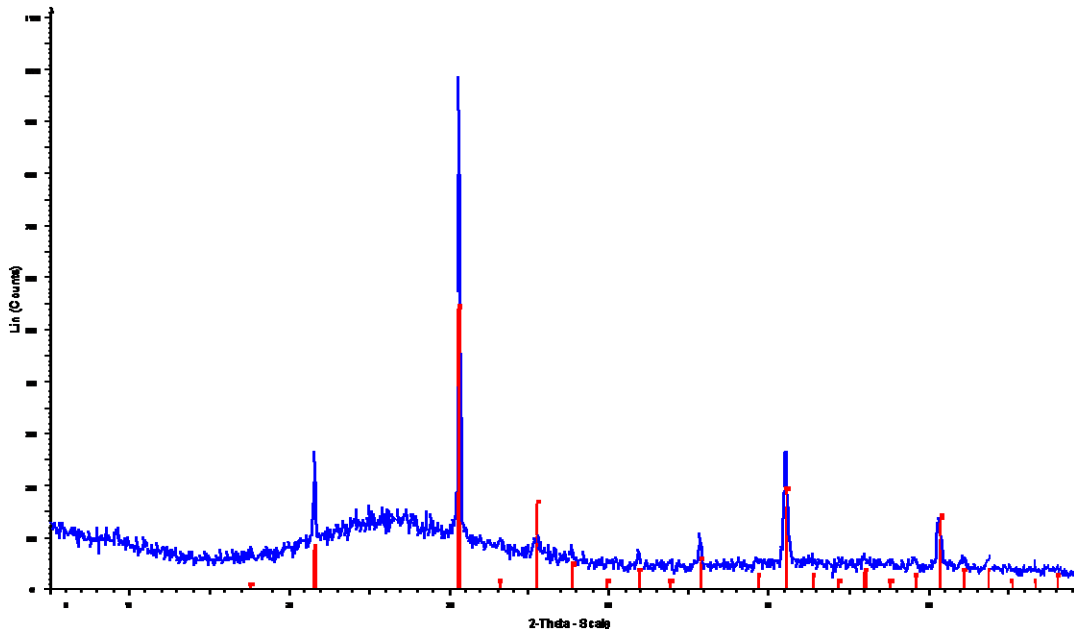

Fig. 4.3. X-ray diffraction spectrum of a 400 nm glass/ITO/WO_3 sample (blue) compared with the theoretical peaks of **In_2O_3 (red)**.

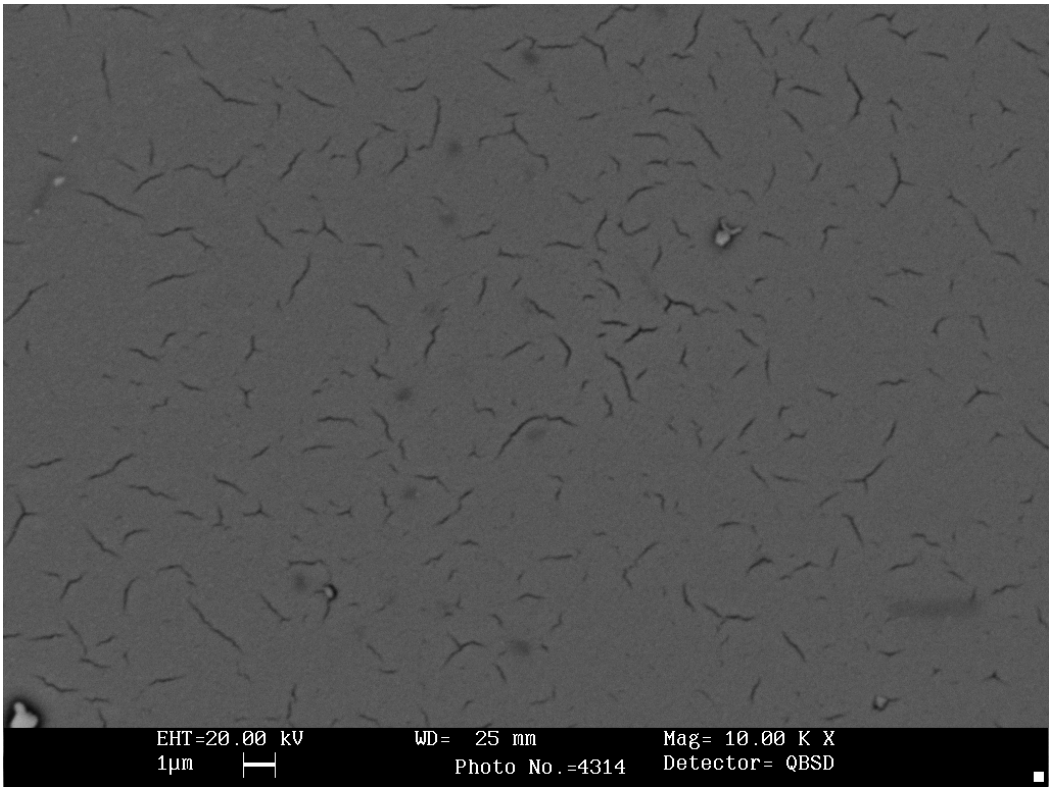

Fig. 4.4. SEM image of the surface of an amorphous 200 nm WO_3 film prepared by the electron beam deposition method.

similar pattern. The spectrum for a 400 nm sample is shown in Fig. 4.3. All the peaks

are due to the In_2O_3 that is present in the ITO layer and there is absence of structure for the WO_3 layer.

Several SEM (Scanning Electron microscopy) images of the surface of the films were taken (see Fig 4.4) using a LEO 440 equipment. Experimental conditions are given in the pictures. All the different thicknesses presented similar results. A uniform surface with some scratches is observed.

Mechanical parameters such as the Young modulus E of the a-WO_3 films were determined using nanoindentation techniques (Nano Indenter XP from MTS) with continuous stiffness measurement (CSM) at $x=0$ (with no ions intercalated). The CSM method consists on applying an oscillating force over the nominal force applied by the indenter, what permits to obtain a profile of the Young modulus along the depth of the sample (Fig. 4.6). Along an indentation experiment, the variation of the applied force with depth is registered. The Young modulus is defined by the scope of the force-depth curve. By averaging between several indentations in different points of the sample, the Young modulus resulted $E \approx 50$ GPa, with slight variations by varying film thickness (see Table 4.1). This technique could not be used to measure E value for the thinnest film.

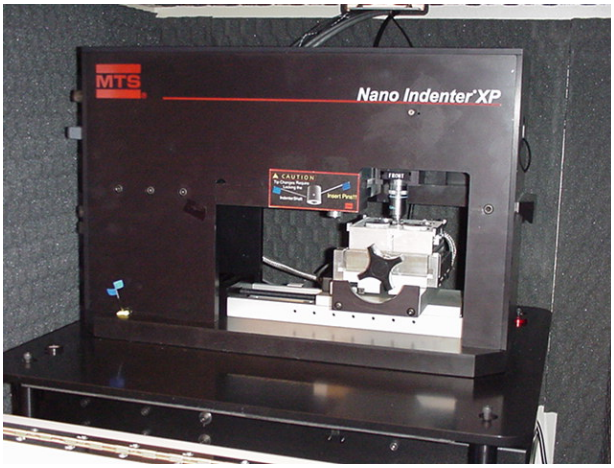

Fig. 4.5. Nano Indenter XP from MTS used to obtain the Young modulus value of the a-WO_3 samples.

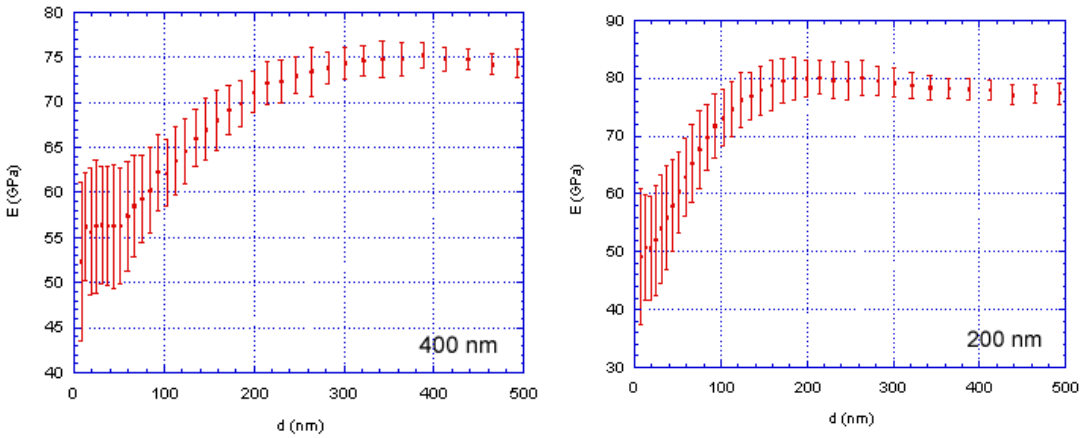

Fig. 4.6. Measurements for the obtention of the Young modulus E for a 400 and 200 nm a-WO_3 film. d is the penetration depth. Reliable values of E are typically located around a 10% of the a-WO_3 layer thickness, so the values for these samples are 56 ± 7 GPa (400 nm) and 51 ± 10 GPa (200 nm).

4.1.2. Electrochemical measurements

Electrochemical measurements were carried out in a shielded two-electrode cell mounted in a dry box. Samples of a-WO_3 deposited onto ITO substrates were used as the working electrodes immersed in a solution of 0.5 M $LiClO_4$ (Aldrich, >95% content) in anhydrous propylene carbonate (Aldrich). The electrolytic solution was bubbled with N_2. A Li foil was used as counter electrode. The cell was specially designed to avoid degradation of Li and consisted on a squared piece of Teflon, where

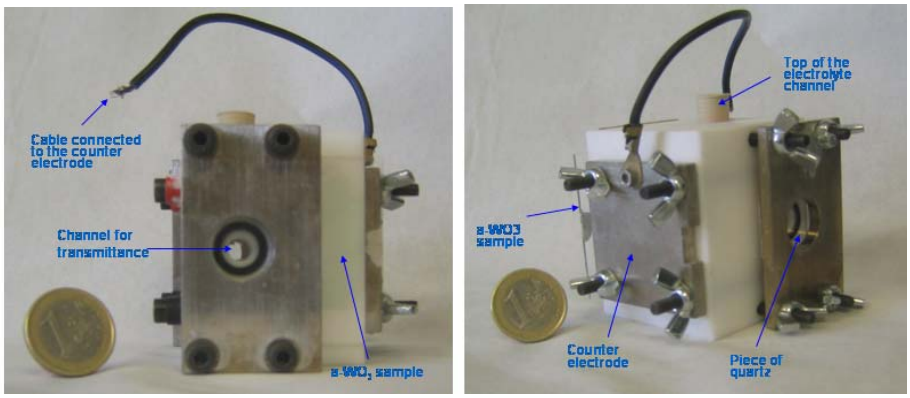

Fig. 4.7. Electrochemical cell employed in the a-WO_3 measurements. Consist on a piece of Teflon with several channels connected one each other. Since a Li foil is used as counter electrode, screws, nuts and joints are used for a proper seal.

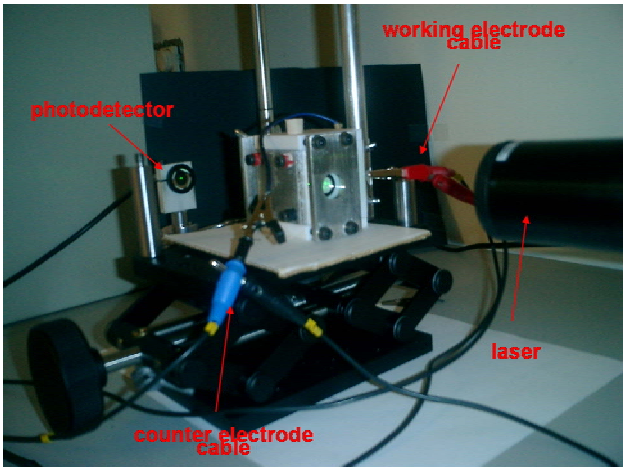

Fig. 4.8. Experimental setup employed for the optical measurements of a-WO_3 samples.

several circular channels were made (Fig. 4.7). Two pieces of quartz were used at the entrance and the exit of the path where optical measurements were performed through. All the experiments were taken using a potentiostat-galvanostat Autolab PGSTAT30 equipment with frequency analyzer module controlled by a computer by means of GPES or FRA software (Fig. 4.9). Chronopotenciometry measurements were carried out at a constant current of 1 or 2 $\mu A/cm^2$. Impedance experiments were performed at several dc potential values in the 10 kHz-1 mHz frequency range, applying a 10 mV ac potential.

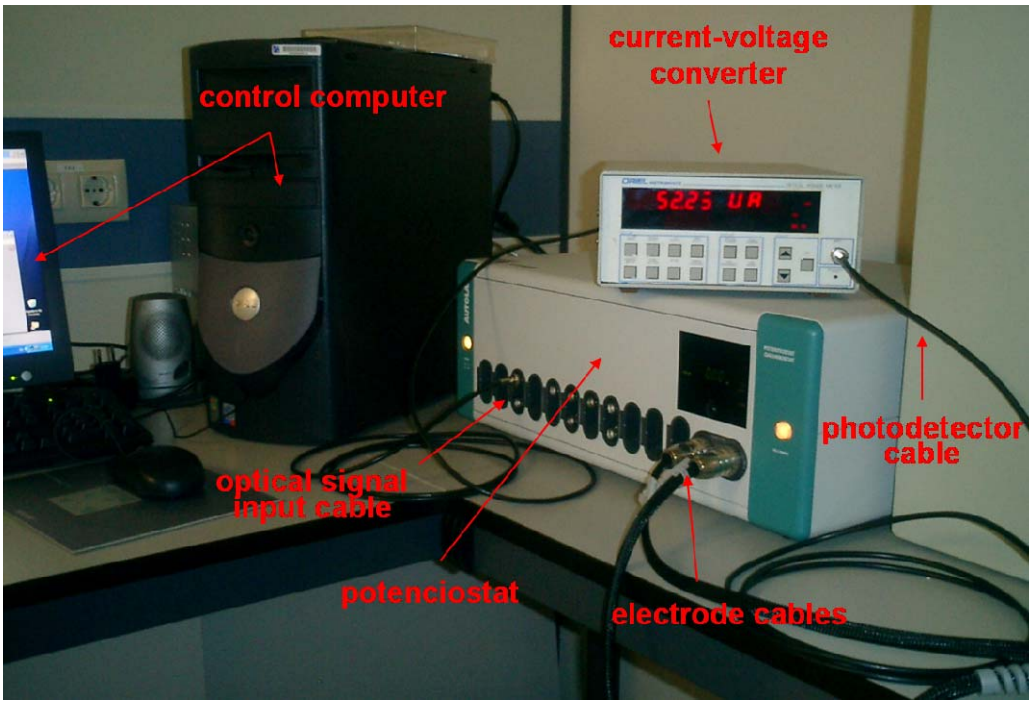

Fig. 4.9. Equipments used in the a-WO_3 measurements. Cables are connected to the potenciostat which is controlled by the computer.

We assure the reach of the electrochemical steady-state in the cell waiting for 15 minutes between the application of the dc potential and the data recording. Fits to the experimental data were performed using SigmaPlot v8.0 software, obtaining good regression coefficient r^2>0.997 and confidence levels (>99%) that assure accurate fits. The optical transmittance was measured simultaneously to the voltammetries by illuminating the cell from the substrate side with a He-Ne laser (wavelenght 543.5 nm) and collecting the transmitted light with a silicon photodetector.

4.2 Description of voltammograms

In a cyclic voltammetry experiment, potential varies linearly with time at a constant scan rate $s = dV/dt$ from an initial value V_1, to a returning potential V_2. Once V_2 is reached, potential returns to its initial value V_1. The cyclic voltammogram (CV) registers the current vs. potential variation. For a pure capacitor, current is given by,

$$I = \frac{dQ}{dt} = \frac{dQ}{dt}\frac{dV}{dV} = Cs\,. \tag{4.1}$$

Apart from capacitors CVs show contributions from another processes like charge transfer, transport phenomena, etc. Deducing how all these processes contribute to the voltammetric response, we will be able to explain the main features of the a-WO_3 voltammetry.

In the experimentally obtained CVs at different scan rates for a 400 nm a-WO_3 film, Fig. 4.10, several characteristics that are also presented at the other thicknesses, are shown. The cathodic current follows a rising behaviour in all cases and a clear anodic peak is drawn after the return voltage is reached. The insertion process is highly reversible chemically as confirmed by the charge being exactly the same in both scan directions. This observation excludes any possibility of a faradaic current flowing in parallel to that responsible for the film charging process. It is also appreciated that the observed anodic peak shifts positively as the scan rate is increased. Moreover, a closer examination allows us to realize that the CVs are highly symmetrical at low enough scan rates and more positive returning potentials (~3.0 V vs. Li/Li^+).

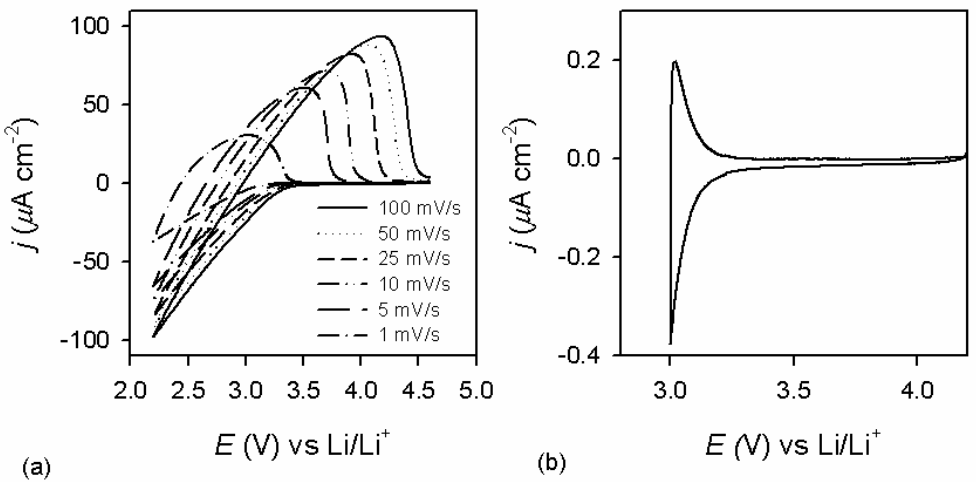

Fig. 4.10. Cyclic voltammograms of a 400 nm a-WO_3 electrode at different scan rates (a), and at a more positive returning potential value (3.0 V vs Li/Li^+) for 1 mV/s scan rate (b).

Since practically all the current is involved in the charging and discharging process of the electrode, the film capacitance will be the starting point to properly describe the CVs. C_μ defines the capability of the electrode to accumulate charge when a variation in the voltage is produced,

$$C_\mu = -\frac{dQ}{dV}. \tag{4.2}$$

As explained in Sec. 2.1.2, the potential of the system relates with the chemical potential of the Li^+ ions in the electrode μ as $dV = -d\mu / e$, hence the chemical capacitance divided by the area can be given by,

$$C_\mu = Le^2 N \frac{\partial x}{\partial \mu} \tag{4.3}$$

where $Q = LNxe$ is the accumulated charge. L is the thickness, N the density of metal atoms in the host, n the density of intercalants and $x = n / N$ the fraction of intercalated Li^+ atoms. From chronopotentiometry experiments (Fig. 4.11a), calculation of chemical capacitance, shown in Fig. 4.11b, is easily obtained by using Eq. (4.3). Huge capacitances are achieved for high insertion levels x>0.1 as is expected for these

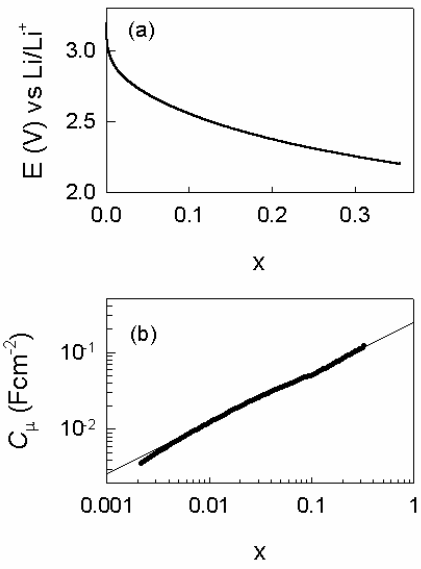

Fig. 4.11. (a) 400 nm a-WO_3 electrode potential as a function of the composition x obtained under constant current (1 μA cm^{-2}) in a solution 0.5 M $LiClO_4$ in propylene carbonate. (b) Equilibrium film capacitance. Straight line corresponds to the power-law dependence $C_\mu \propto x^a$ (a=0.65).

systems, and a power-law dependence of capacitance $C_\mu \propto x^a$ at $x > 10^{-3}$ ($0.8 > a > 0.65$) is obtained for different films. By means of the experimental relationship $V(x)$ shown in Fig. 4.11a and using Eq. (4.3), the dependence of the chemical capacitance on potential $C_\mu \propto V^\alpha$ ($4 > \alpha > 1.85$) is obtained.

For the simulations we will assume that the total film capacitance follows a relationship given by,

$$C = \beta(V_0 - V_{\mathbf{C}})^\alpha + C_{\mathbf{H}} \qquad (4.4)$$

in which the first summand corresponds to C_μ, V_{C} is the potential in the capacitor, V_0 represents the starting point for the rise of C_μ, and C_{H} accounts for the effect of the constant capacitance of the Helmholtz layer (C_{H} ~10 μF cm^{-2}) connected in parallel with the chemical capacitance. α and β are constants. At potentials more positive than V_0 one can assume that $C_\mu \approx 0$. The effect of C_{H} is to provide a baseline at potentials more positive than V_0.

As discussed previously, if the electrode response is that of a capacitance CVs should reflect the dependence of the capacitance on potential, Eq. (4.1). This is the case in which potential drops in the cell associated with kinetic effects (ionic transport or diffusion) can be completely neglected with respect to the charging potential. The curve

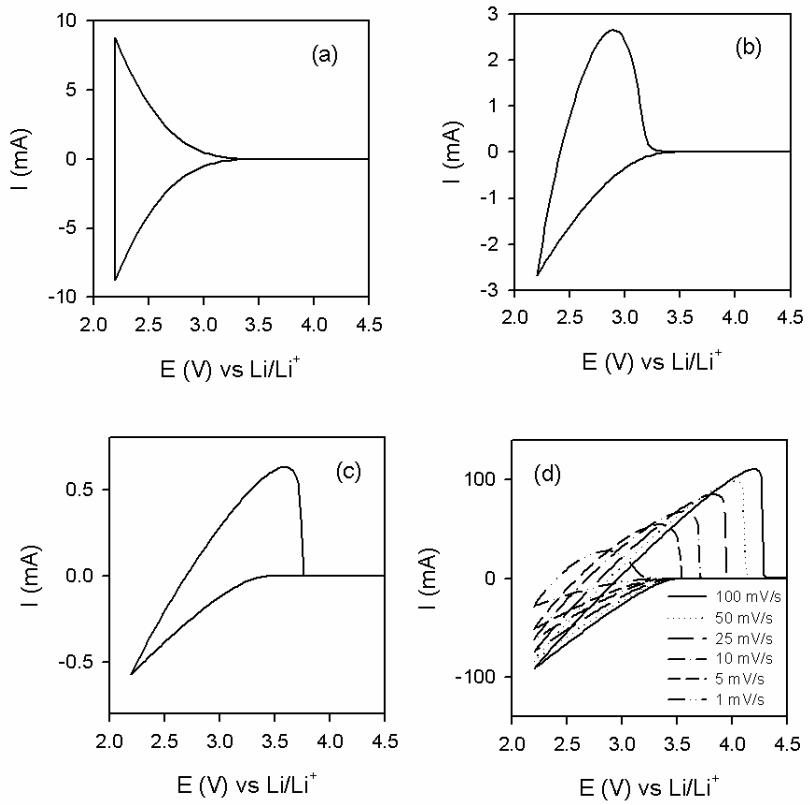

Fig. 4.12. Simulation of cyclic voltammograms for a potential-dependent capacitance [Eq. (4.4)] and a series resistance. V_1 =4.6 V, V_2 =2.2 V, V_0 =3.5 V, α =3, β =0.04 FV^{-3} and C_H =5 μF. For a scan rate of 100 mVs^{-1} and different values of the series resistance R_s (in Ω) (a) 0, (b) 100, (c) 1000, and (d) varying the scan rate for R_s =9000 Ω.

is symmetric because of sign reversal of s (see Fig. 4.12a). This type of response can be observed in the CV of Fig. 4.10b, when the more positive returning potential is applied. We show in the following that the distortion of such symmetrical CV shape in the anodic direction observed for less positive return potentials and high scan rates is due to the effect of a series resistance R_s connected with the film capacitance C. When the kinetic effects such as the transport of ionic species cannot be neglected the cell potential can be written $V = V_T + V_C$, where in addition to the capacitor potential, V_C, the V_T corresponds to potential drops associated with the transport components. We will assume that a constant series resistance R_s suffices to account for the transport effects, so that when the CV current is I, we have $V_T = IR_s$. It is important to

recognize that the voltage fraction absorbed by the series resistor increases as the current grows, $V = V_C + IR_s$. This implies that the only potential at which $V = V_C$ corresponds to $I = 0$, and hence this potential is the less positive value reached by V_C at a given scan rate. In a CV experiment, while polarizing in the cathodic direction between the cell potential limits of V_1 and V_2, V_C is

$$V_C = V_1 - st - R_s I_c . \tag{4.5}$$

In the same way, during the anodic polarization between the cell potential limits of V_2 and V_1, V_C is

$$V_C = V_2 + st - R_s I_a . \tag{4.6}$$

On the other hand, the current that passes through the cell may be described by

$$I = \frac{dQ}{dt} = \frac{dQ}{dV_C}\frac{dV_C}{dt} = C\frac{dV_C}{dt} . \tag{4.7}$$

In our case C is described by Eq. (4.4), which when combined with Eqs. (4.5-4.6) allows us to obtain the differential equations to derive $V_C(t)$. These differential equations can be solved numerically starting from $V_C(t=0)$=0 V and using additional parameters extracted from equilibrium film capacitance fits. Simulation results are shown in Fig. 4.12. CVs become more distorted by the influence of the series resistance, Fig. 4.12(a,b,c). It is useful to point out that for large capacitive elements the cathodic current displays a linear increase with a slope of $1/R_s$ owing to the fact that higher capacitances involve lower values of V_C. Figure 4.12d shows that the main features already described in the experimental CVs of Fig. 4.10 are now reproduced by the simple model. On the one hand, the anodic peak undergoes a shift toward more positive potentials as scan rate increases. In the $R_S C$ model, the capacitor stores charge during the cathodic direction of the voltammogram and also during the anodic direction while

the current is negative. When the current becomes positive in the anodic direction, the capacitor releases all the charge accumulated giving rise to a peak with a certain positive maximum I_{max}. It must be noted that the return peaks illustrated in Fig. 4.12 are not related to a diffusion-limited redox process but instead derive from the distortion of the purely capacitive voltammogram (Fig. 4.12a) produced by R_S. When current is low (lower values of s and/or more positive potential values) the IR_S term takes less relevance and the CV shows a more symmetric (capacitive) form.

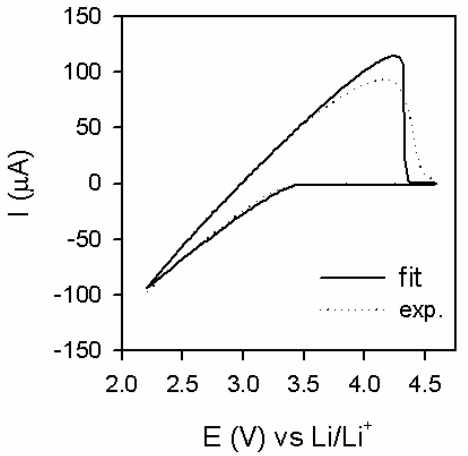

Fig. 4.13. Theoretical fit using the R_sC -series circuit model discussed in the text of the CV at 100 mV s^{-1}. V_1 =4.6 V, V_2 =2.2 V, V_0 =3.5 V, α =3, β =0.05 FV^{-3}, C_H =1 μF and R_s =9000 Ω.

We have also used the model for fitting experimental CVs responses. An example of the results obtained is shown in Fig. 4.13. Experimental curves are reproduced in their general trends, although some deviations between experiment and fits occur in the high voltage range of the anodic direction. Capacitance parameters obtained from fits agree with those derived from chronopotentiometry experiments. On the other hand, series resistance $R_s \approx 9000\ \Omega$, what clearly indicates that other resistive effects than the electrolyte contribution must be involved. Fits likely improve by considering a voltage-dependent resistance as well. We propose that both the ionic charge transfer on the solution-WO_3 interface as well as the resistance related to the Li^+ diffusion inside the film should account for explaining the kinetic limitation responsible of the CVs deviation from a purely capacitive behaviour.

4.3 Thermodynamic model

In this section we study the thermodynamic behaviour of a-WO_3 films of different thicknesses. Chemical capacitance vs. composition variations are calculated by means of chronopotenciometry measurements. The existing model[1] that accounts for the voltage-composition curves based on a distribution of energy sites is reviewed. A new model based on host-lattice distortions is proposed. Along the whole section, we will refer to μ_{Li^+} just by using μ for simplicity.

4.3.1. Review of the distribution of energy sites model

From chronopotenciometry experiments shown in Figure 4.14, the chemical capacitance (per unit volume) was calculated using

$$C_\mu = C_0 \frac{\partial x}{\partial(\beta\mu)}, \tag{4.8}$$

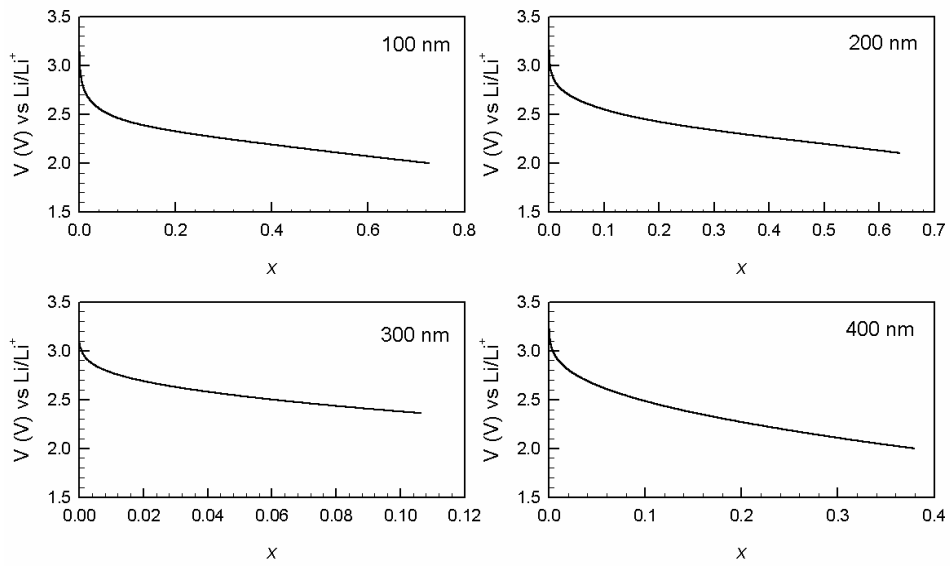

Fig. 4.14. a-Li_xWO_3 electrode potential as a function of the composition x in a solution 0.5 M $LiClO_4$ in propylene carbonate for different film thicknesses.

where $C_0 = \beta e^2 N$ is a constant approximately equal to 20 kF cm^{-3} for these films. It is worth noticing that this equation equals to Eq. (2.18). Variations of $C_\mu(x)$ are shown in Fig. 4.15 in a log-log representation that highlights asymptotic dependences in the intercalation level within $10^{-3} < x < 0.6$. By examining Figure 4.15 one can observe a clear change of the asymptotic slope m of the capacitance with x under variation of the film thickness. Slope tends to one as film thickness is reduced and reaches $m \approx 0.65$ for the thickest film.

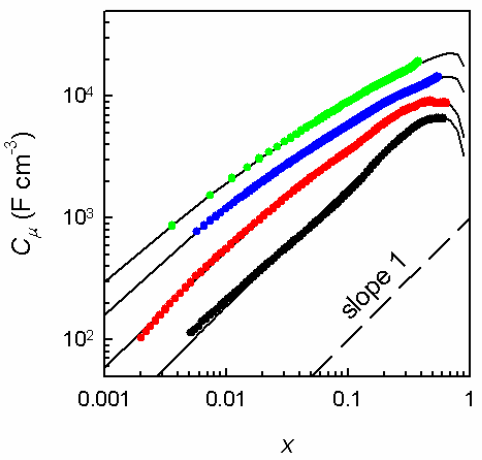

Fig. 4.15. Chemical (equilibrium) film capacitance as a function of the composition x for film thicjness (in nm): (black) 100, (red) 200, (blue) 300, and (green) 400. Fine solid lines correspond to fits using Eq. (4.15). Capacitance is multiplied by 2,4, and 8 for thickness 200, 300, and 400 nm, respectively, to improve the clarity of the graph.

An important effort in the understanding of voltage-composition curves in amorphous materials was proposed by Kudo et al[1]. They considered a wide distribution of sites energies for the ions to intercalate, which is quite reasonable for amorphous materials. This is a model of non-interacting ions so that available sites are occupied randomly. The amount of insertion is related to the chemical potential as

$$x = \frac{1}{N}\int_{-\infty}^{\mu} g(E)dE\,. \qquad (4.9)$$

$g(E)$ is the density of states function, i.e. the density of stationary ion sites with the potential energy at the level E. For a continuous distribution of sites energies the chemical capacitance per volume unit takes the form,

$$C_\mu = e^2 N \frac{\partial x}{\partial \mu} = e^2 g(\mu)\,. \qquad (4.10)$$

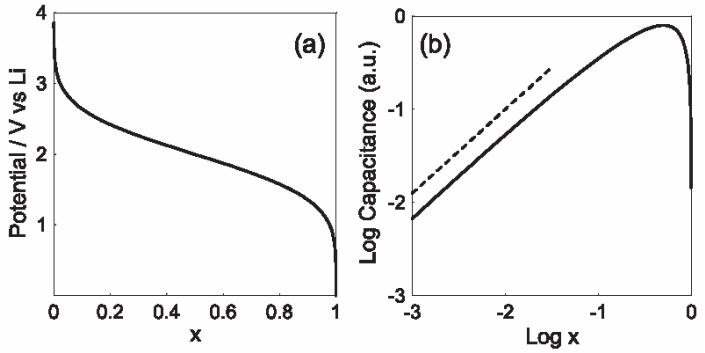

Fig. 4.16. Thermodynamic quantities for a Gaussian distribution of energy sites, σ =0.5 eV, E_0 =-2.0 eV. (a) Electrode potential, Eq. (4.12). (b) Chemical capacitance, Eq. (4.13). The dashed line indicates the dependency $y = x^{0.9}$.

Therefore, C_μ shows directly the density of states in the material. For the Gaussian distribution of energy sites,

$$g(E) = \frac{1}{(2\pi)^{1/2}} \frac{N}{\sigma} \exp\left[-\frac{(E - E_0)^2}{2\sigma^2} \right], \tag{4.11}$$

being E_0 the energy of $g(E)$ maximum and σ the half-width at half-height, the chemical potential can be given in terms of the inverse error function[1],

$$\mu(x) = E_0 + 2^{1/2} \,\mathrm{erf}^{-1}(2x - 1). \tag{4.12}$$

From Eqs. (4.10-4.12), the chemical capacitance for the Gaussian distribution is obtained

$$C_\mu(x) = \frac{e^2 N}{(2\pi)^{1/2} \sigma} \exp\left\{ -\left[\mathrm{erf}^{-1}(2x - 1) \right]^2 \right\}. \tag{4.13}$$

Fig. 4.16 illustrates both Eq. (4.12) and Eq. (4.13) in the $0 < x < 1$ range. It was found to provide a good fit[1, 2] to the potential-composition curves of a-WO_3. However, the shape of Eq. (4.13) is independent of the parameters σ and E_0. The spread σ modifies the shape of $\mu(x)$, but not that of $C_\mu(x)$, leading to a $C_\mu \propto x^a$ relation at low intercalation levels, being $a \approx 0.9$ always constant, what is not consistent with our experimental results (Fig. 4.15). Apart from that, the shape of the distribution implies

larger intersite distance between the lower energy sites, which are filled first at low x, so that diffusion along deep sites should be more difficult than among higher density states, just the opposite observation that we obtained (Fig. 4.24). That will be discussed later in Sec. 4.6.1.

4.3.2. Host distortion model

We have proposed a phenomenological approach for interpreting the cell voltage variation with the amount of inserted ions by regarding contributions to the chemical potential of Li^+ inside the amorphous film caused by host distortions. In this approach the chemical potential takes the form,

$$\mu = E_0 + (1+\eta)Gx^{\eta} + \beta^{-1}\ln\frac{x}{1-x}. \qquad (4.14)$$

In this equation the first term E_0 corresponds to a constant energy level, the second one $(1+\eta)Gx^{\eta}$ relates to the dependence of the intercalant-host interaction with the insertion level. For $G>0$ additional energy is needed to deform the host. The last summand accounts for the entropic term ($\beta^{-1}=k_{\mathrm{B}}T$ is the thermal energy). An additional term Ux, included in the mean-field lattice gas model [Eq. (2.10)], is not considered in Eq. (4.14). It represents the interparticle interaction contribution which is estimated to be weak ($U \approx k_B T$) and can be safely neglected.

Chemical capacitance results from combining Eq. (4.8) and Eq. (4.14) as

$$C_{\mu} = C_0\left[\eta(1+\eta)\beta G x^{\eta-1} + \frac{1}{x(1-x)}\right]^{-1}. \qquad (4.15)$$

We have used Eq. (4.15) in order to fit the behaviour exhibited by the chemical capacitance (see Figure 4.15 for a comparison between fitting and experimental curves).

Excellent fits were obtained. For the thinnest (100 nm) film the intercalant-host interaction term G is not detectable so that the system behaves like an ideal non-interacting lattice gas in which entropic contributions play the determining role. In this case a power-law relationship as $C_\mu \propto x$ for $x << 1$ is obeyed. As thickness is increased G becomes larger what modifies the asymptotic behaviour of the chemical capacitance (see Figure 4.15). The exponent of the intercalant-host interaction term resulted $\eta \approx 0.5$, and N laid within the range of 10^{22} cm^{-3}. All fitting parameters are summarized in Table 4.1.

film thickness (nm)	N ($10^{21}cm^{-3}$)	G (eV)	η	E (GPa)
100	6.2 (1.3)	<0.001	—	—
200	4.8 (1.0)	0.058 (0.03)	0.59 (0.02)	51 (10)
300	8.6 (1.1)	0.283 (0.04)	0.51 (0.01)	50 (7)
400	7.8 (1.0)	0.354 (0.01)	0.50 (0.01)	56 (7)

Table 4.1. Fitting parameters resulting by using the variation of the chemical capacitance with composition of Eq. (4.15). Young modulus E obtained by averaging from 25 nanoindentations.

4.4 Volume changes

4.4.1. Experimental results

With the aim of gaining further insight into the thermodynamics of lithium intercalation we have studied the volume-change response of the a-WO_3 electrodes. The relative volume changes at x=0.4 of a set of a-WO_3 films with different thickness were measured with a confocal imaging profiler (Sensofar PLμ). Figure 4.17 corresponds to a topographic representation of the height reached by the outer surface of the film. The image for 200 nm-thick film, which spreads over an area of 637×477 μm^2, clearly shows the bordering limit of the intercalated part (left side of Figure 4.17a) and the flat surface corresponding to non-intercalated film region. Expansion is observed to yield a highly rough surface in the intercalated part. The software of the Sensofar PLμ instrument allows determining the average volume expansion by means of proper image algorithms. All films showed similar patterns, relative volume changes near 10 % in average (see Figure 4.18), except for the 100 nm-thick

(a)

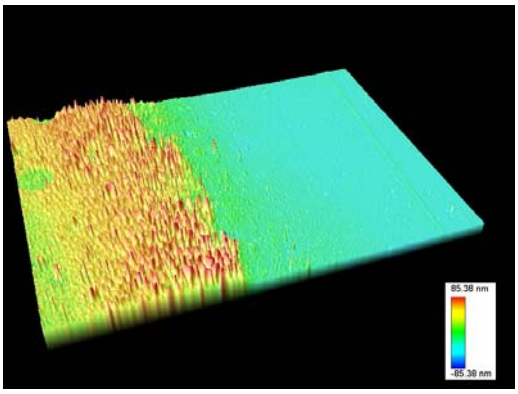

(b)

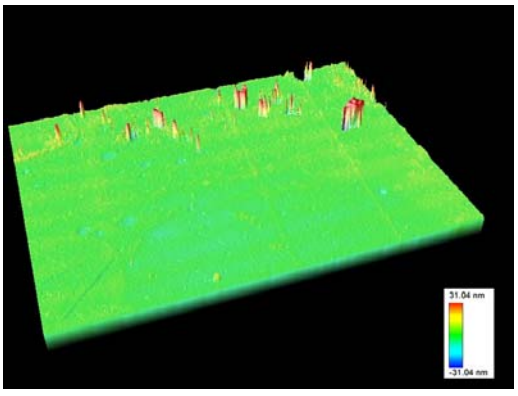

Fig. 4.17. Topography of two a-WO_3 films of 200 nm (a) and 100 nm (b) of the border between a non-intercalated area (right part of the image) and an intercalated one (left part of the image) at x=0.4. Volume change is not observed for 100 nm-thick samples. Scanned area is 637×477 μm^2.

samples (Fig. 4.17b) which presented no expansion at all (same scanned area), in good agreement with findings resulting from electrochemical measurements (G =0).

4.4.2. Vakarin's model on elastic distortions

To correlate electrochemical and topographic measurements we need to extract information related to film expansion from the fitting parameters obtained in analyzing the chemical capacitance response in Eq. (4.15). The model by Vakarin et al[3]. described in Sec. 2.1.3 will be useful for that purpose.

In that model, we will assume that all the stress applied to the sample by the intercalation process is transformed in elastic energy by deforming the lattice. This corresponds to vanishing loading stress $\sigma(x)$=0, as in the case of unclamped films[3], so Eq. (2.16) should be used. To connect this expression with our model [Eq. (4.15)], we adopt the following identifications,

$$\frac{(1+\eta)x^{\eta}}{\alpha} = p(x)\frac{\mathrm{d}p(x)}{\mathrm{d}x}, \tag{4.16}$$

$$\alpha G = \Lambda\delta^{2}, \tag{4.17}$$

being α =2 a proportionality constant, which results from the limiting constraints $p(0)$=0 and $p(1)$=1. After integration of Eq. (4.16), it is obtained that the expansion fraction obeys a power-law of concentration,

$$p(x) = x^{\left(\frac{1+\eta}{2}\right)}. \tag{4.18}$$

Eq. (4.18) implies that the film expansion exhibits a rather smooth, sublinear response presumably caused by the amorphous structure of the films that steeply accommodates the deformation. Since the exponent in Eq. (4.18) results $(1+\eta)/2 \approx 0.75$, one obtains a response near the linear Vegard's law[4].

The effective elastic constant appearing in Eq. (4.17) can be readily written in terms of the Young modulus of the films, $\Lambda = eE / N$, and therefore one arrives at an expression for determining relative expansions at full intercalation,

$$\delta = \left(\frac{2GN}{eE} \right)^{1/2} . \qquad (4.19)$$

Values of volume changes at x=0.4 can be simply obtained by doing the product $\delta p(0.4)$. By applying Eq. (4.18) and Eq. (4.19), the parameters obtained from chemical capacitance fitting, along with the elastic constant E measured, we have an alternative way for determining film expansion. These values are compared with those obtained through profilometry measurements (Fig. 4.18).

4.4.3. Discussion

By examining Fig. 4.18 one can realize that both measurements (electrochemical and profilometric) result in film volume change around 10% in the case of thicker films (300-400 nm). The agreement is even excellent for thinnest films (100 nm) for which no expansion is detected and, accordingly, no deviation from simple lattice gas model is observed. Between these two extreme limits there must be a transition thickness around 200 nm at which the films do not undergo full expansion. A sharp transition region can

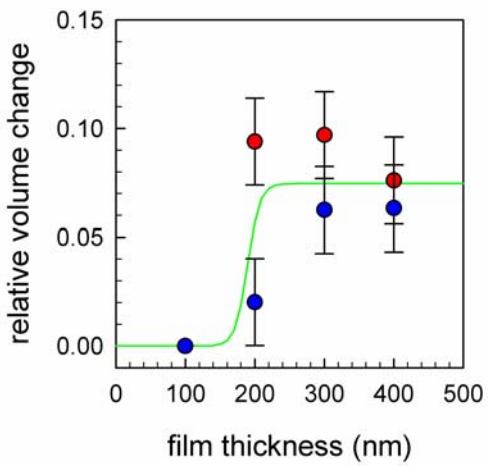

Fig. 4.18. Relative volume change comparison at x =0.4 between values measured by direct profilometry measurements (red dot) and using fitting parameters of the chemical capacitance response with composition (Table 4.1) and Eq. (4.19) (blue dots). Solid line is a fitting made from all points.

explain the difference in volume changes resulting from both techniques for 200 nm-thick films[5].

It is worth noticing the clearly distinct intercalation behaviour reported for 100 nm-thick films in comparison with thicker films. The fact that thinnest films do not exhibit volume changes points to the occurrence of a particular intercalation mechanism somehow governed by the reduction in the layer size. It may be interesting to speculate about the possible origin of such change in the intercalation mechanism. It is broadly accepted that charge storage in bulk materials occurs by homogeneous intercalation of electrons and ions into the host electrode. By means of optical measurements taken along voltammetry experiments (Fig. 4.19) we can assure that electrons enter in the a-WO_3 layer, since a great change in coloration occurs. Yet an alternative charge storage mode has recently been suggested, derived from the charge separation at interfacial boundaries. Jamnik and Maier[6] have specifically addressed nano-size effects in lithium intercalation materials. For semiconductor materials in contact with a metal (or quasi-metallic material like ITO) an electron depletion layer is formed with a length depending on specific parameters of the contact, but usually shorter than 200 nm. It has been then suggested[6] that a purely electron insertion, compensated by ions distributed near the surface of

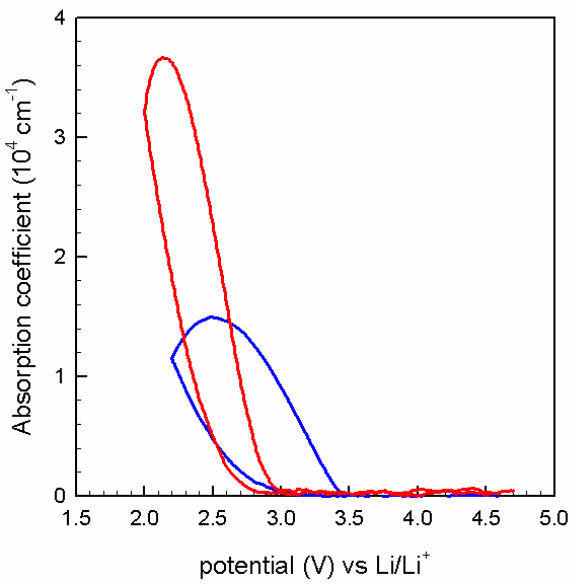

Fig. 4.19. Absorption coefficient evolution at a 543.5 nm wavelength along a cyclic voltammetry experiment at 5 mV/s for a 400 (blue) and 100 nm (red) a-WO_3 film.

depleted nano-particles, is able to reach chemical capacitance values as large as those expected for homogeneous, bulk intercalation. The situation resembles that encountered in electron storage in porous TiO_2 layers made up of particles of nanometer size[7]. Other possibilities cannot be completely discarded: the assumption we have adopted in deriving Eq. (2.16) that the loading stress $\sigma(x)$ is safely negligible is perhaps a simplification of the real stress field built at the ITO/WO_3 interface. Differences in the amorphous structure (free volume) may also be behind the experimental observations. Further research is needed aiming to interpret the distinct response reported for thinner a-WO_3 films in terms of such recently introduced intercalation mechanisms[6].

4.5 Impedance model

The experimentally obtained impedance spectrum of the a-WO_3 films can be theoretically explained with the following elements that describe the distinct processes that take place in the electrochemical system:

- *Series resistance (R_S):* It is always present. It accounts for the resistance to the ionic transport in the solution and the electronic resistance in the leads and wires of the system.

- *Double layer capacitance (Q_{dl}):* It is due to the charge accumulation at the WO_3/electrolyte interface. When electrons are injected in the WO_3, some of them are accumulated in the surface and balanced with ions from the solution, forming the double layer, that is described by a constant phase element (CPE),

$$Z_{Q_{dl}} = \frac{1}{Q_{dl}(i\omega)^n}, \text{ being } 0 \le n \le 1. \qquad (4.20)$$

The parameter n is typically close to one and accounts for the deviation from the ideal behavior (n=1) of the capacitance. In real systems is difficult to find an ideal behavior so CPEs are frequently used.

- *Ionic charge transfer resistance (R_{ct}):* It is the resistance that ions feel when they pass from the solution zone closer to the electrode into the interior of the oxide lattice. In this process the ions should get rid of the solvation molecules and trespass the potential barrier to be intercalated into the interstices of the lattice. This resistance does

not show large changes along the dc potential since its nature is not faradaic (charge transfer).

- *Diffusion impedance:* It describes the phenomena that take place in the bulk of the electrode. When intercalated, ions are accumulated and diffuse along the lattice sites. These processes are accurately described by using a *transmission line* element[8]. It should have two elements, r (Ωcm^{-1}), that is the resistance to the diffusion of ions, and q (Fcm^{-1}), that is the chemical capacitance of the a-WO_3 film and accounts for the capacity of the film to accumulate ions. The impedance of the transmission line is defined as[9]

$$Z_D = R\left(\frac{i\omega}{\omega_d}\right)^{-\frac{\gamma}{2}} \coth\left[\left(\frac{i\omega}{\omega_d}\right)^{\frac{\gamma}{2}}\right] \tag{4.21}$$

where $R = Lr$, being L the film thickness and ω_d the characteristic frequency, located near the elbow of the impedance plot (see Fig. 4.20) and is defined as,

$$\omega_d = \frac{1}{(rqL^2)^{1/\gamma}}. \tag{4.22}$$

The inverse of this frequency corresponds to the transit time for a diffusing particle to cover the whole L distance[8]. From ω_d the chemical coefficient value can be readily obtained[10] by $D_{ch} = (rq)^{-1}$. γ is related to the deviation from the normal spatially restricted diffusion impedance[11] ($\gamma = 1$). When $\gamma < 1$, anomalous diffusion mechanism occurs[12], which may be related to structural disorder effects that are expected to occur in amorphous materials. At high frequencies $Z_D \propto (i\omega)^{-\gamma/2}$ gives a straight line inclined at less than 45º (the common response of ordinary diffusion). At frequencies lower than ω_d the capacitive behaviour due to the film charging is generalized by means of a CPE

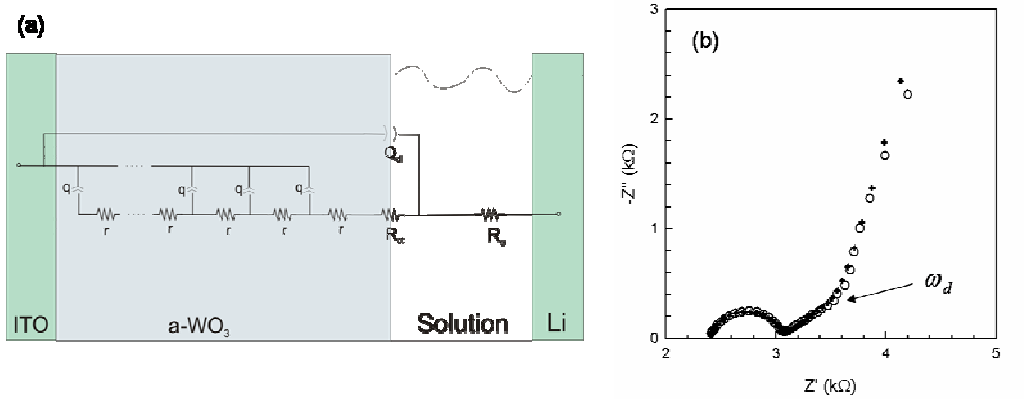

Fig. 4.20. Equivalent circuit (a) used for description of the impedance spectra obtained (b) in a 400 nm a-WO_3 film at 2.2 V vs. Li/Li^+ dc potential. (o) are the experimental points and (+) the fit to the equivalent circuit.

$Z_D \propto (i\omega)^{-\gamma}$. The equilibrium film capacitance $C_\mu = qL$ may be recovered from this low-frequency capacitive behaviour. Both R and C_μ may show large variation along the dc potential.

As a summary, in Fig. 4.20 appears the equivalent circuit with its elements placed in the areas of the system where the physical phenomena that describe take place. On the right it is shown an impedance spectra at a dc potential value where all the elements and processes appear. It is worth noticing the excellent fit provided by our model. The semicircle observed at high frequencies is due to the parallel combination of the ionic charge transfer resistance R_{ct} and the double layer capacitance Q_{dl}. The linear part at less than 45º of inclination is due to the transport resistance r to the diffusion of the ions in the bulk of the

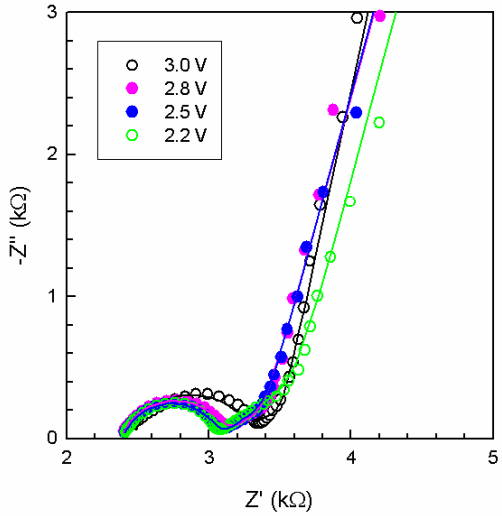

Fig. 4.21. High frequency detail of the impedance spectra taken at the dc potentials indicated in the legend for a 400 nm WO_3 film. Lines are the fits provided by the theoretical model described.

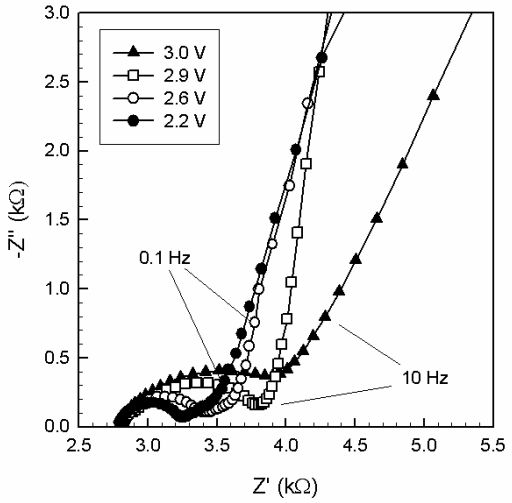

Fig. 4.22. High frequency range of the impedance spectra taken at the dc potentials indicated in the legend for a 100 nm WO_3 film.

material. When ions diffuse and finally arrive at the substrate surface (blocking), they become accumulated in the material and the imaginary part of the impedance increases quickly due to the predominance of the chemical capacitance q.

Finally, Figs. 4.21 and 4.22 show how the impedance spectra changes at different dc potential values for a 400 and 100 nm a-WO_3 film respectively. As discussed previously, it is appreciated that R_{ct} does not show a significant change in its magnitude order and r, the diffusion resistance, increases at lower potential values. Similar spectra are observed for the rest of the film thicknesses, though it is difficult to clearly distinguish the diffusion part in some cases.

4.6 Diffusion coefficients

4.6.1. Experimental results

The chemical diffusion coefficient D_{ch} can be readily determined by means of electrochemical impedance measurements as described in Sec. 4.5. Some of the experimental impedance spectra and their fits are shown in Fig. 4.23. As discussed in chapter 2.3, when an ionic species diffuses in the material, the true driving force for

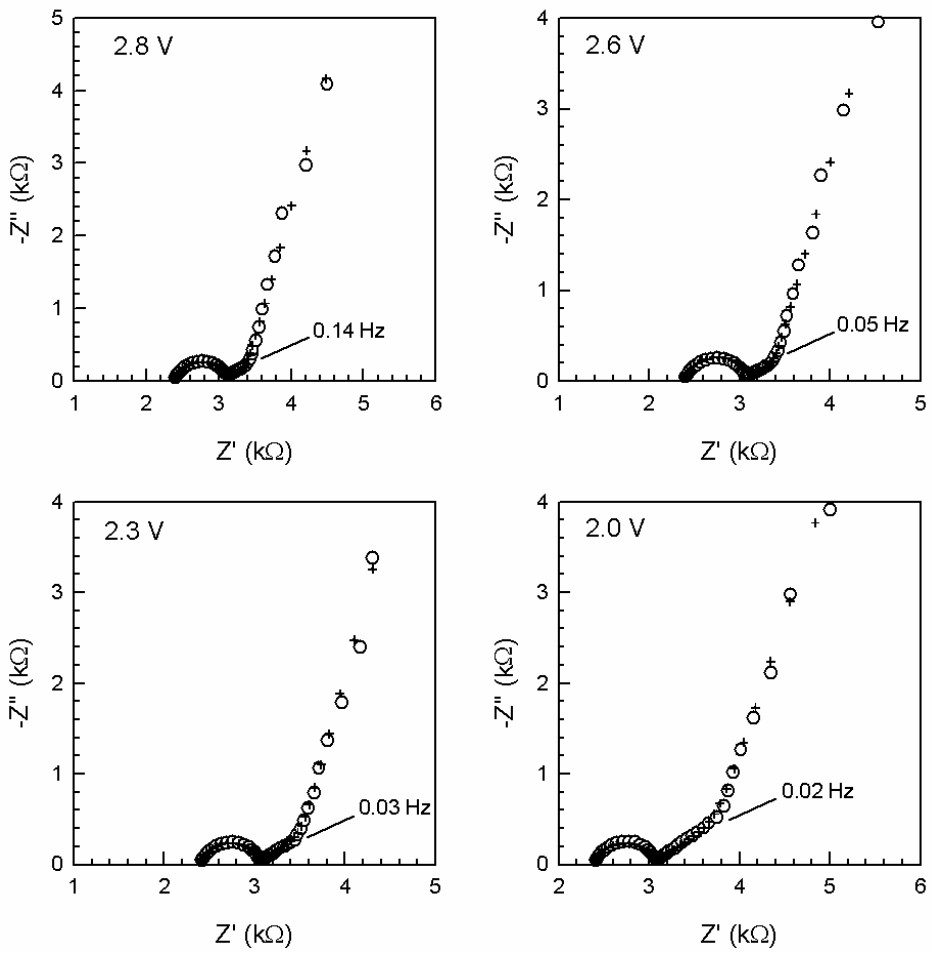

Fig. 4.23. (o) Impedance spectra of a 400 nm a-WO_3 film obtained in a 10 kHz-1 mHz frequency range. (+) Fits provided by the model described in Sec. 4.5. Approximated characteristic frequency ω_d is indicated in each graph.

diffusion is the gradient of the chemical potential. χ_T, the thermodynamic factor, accounts for the difference between concentration and chemical potential gradient and can be easily calculated from the chemical capacitance by,

$$\chi_T = C_0 x / C_{ch} . \tag{4.23}$$

More specifically, the jump diffusion coefficient D_J describes the average hopping events, and is defined by means of

$$D_{ch} = \chi_T D_J . \tag{4.24}$$

From the jump diffusion coefficient values, the mean jump activation energy ΔE can be obtained, since $D_J = \Gamma l^2$, where l ~5 Å is the average hopping distance and the rate Γ with which lithium hops to vacant neighbouring sites is considered to be thermally activated

$$\Gamma = \nu \exp\left(-\Delta E / k_B T\right), \tag{4.25}$$

being ν a vibrational frequency of a migrating ion around its equilibrium position, typically on the order of 10^{13} s^{-1}.

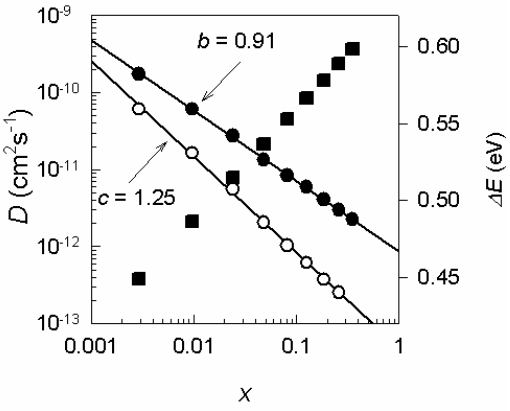

Fig. 4.24. (•) Chemical D_{ch} and (o) jump D_J diffusion coefficients calculated from impedance measurements and the thermodynamic factor, indicating the dependences $D_{ch} \propto x^{-b}$ and $D_J \propto x^{-c}$ for a 400 nm a-WO_3 film. (■) Average potential height ΔE dependence on the insertion level.

Variation of these three parameters (D_{ch}, D_J and ΔE) with composition is shown in Fig. 4.24 for a 400 nm film. Other thicknesses presented similar patterns. Both D_{ch} and D_J decrease with x, showing in this case a relationship of $D_{ch} \propto x^{-b}$ ($b \approx 0.91$) and $D_J \propto x^{-c}$ ($c \approx 1.25$) respectively. On the basis of a Gaussian distribution of energy sites (mentioned in Sec. 4.3.1) consideration, it should be expected that the increasing

occupancy of deep sites with increasing x should lead to an increase of D_J and in fact, the observed variation is the opposite. ΔE shows a $\Delta E \propto ck_BT \ln x$ relationship ($c \approx 1.25$) for the composition range x <0.3. Taking into account our model, Eq. (4.14), where lattice distortion plays an important role, it is presumable that distortion caused during intercalation modifies the intersite barriers for hopping, causing a decrease of the jump diffusion coefficient (increase of the barrier heights) with increasing extent of intercalation.

4.6.2. Potential barrier calculations

For a better understanding of the dependence of the potential barrier height for the hopping pathway with the insertion level, we performed a theoretical study[13] based on first-principles calculations for crystalline WO_3. Results (see Fig. 4.25) predict an increase of the barrier height along intercalation level x, exhibiting a relation of the type $\Delta E \propto ck_BT \ln x$ for x <0.3, the same as the experimental case, but being $c \approx 1.55$. In principle should not be expectable to observe the same behaviour in a crystalline structure of WO_3 than in the amorphous counterpart. This likely

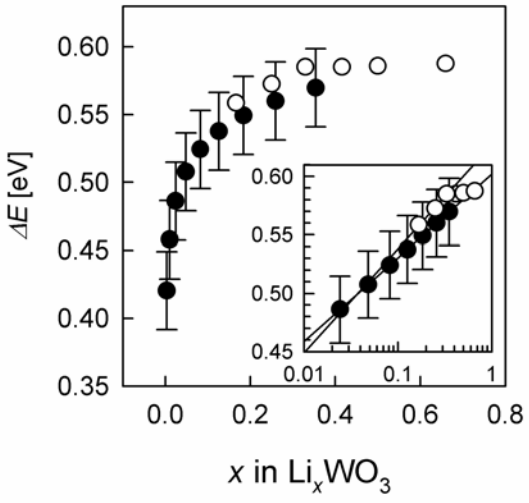

Fig. 4.25. Energy barrier variation on composition x in Li_xWO_3. (●) Example of experimental data derived from measurements of D_J using a vibrational frequency ν =3·10^{13} s^{-1} and hopping distance l =5 Å. Error bars resulting by regarding the vibrational frequency as ranging within 10^{12}–10^{13} s^{-1}. (○) Theoretical calculations results. In the inset, same data in a log-linear representation. Straight lines indicate the relation $\Delta E \propto ck_BT \ln x$ with c =1.55 (simulation) and 1.25 (experiment).

points out that the observed diffusion coefficient trend is an intrinsic property, taking place at a very local area, rather than a behaviour induced by the inherent disorder of the glassy structure.

Apart from the variation of the energy barrier along composition, a detailed examination of the diffusion path has been carried out (Fig. 4.26). The diffusion process

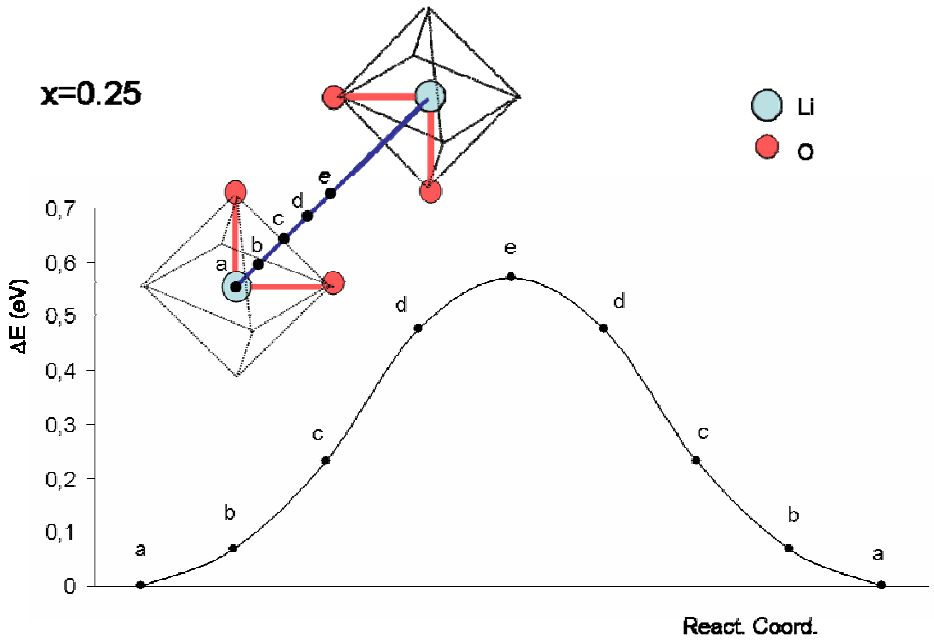

Fig. 4.26. Evolution of the diffusion process along a path connecting the octahedral vacant hole sites (a). For each composition, five geometries have been optimized along the pathway that have been situated as five points on the profile ($x = 0.25$). Energy barrier corresponds to the geometry placed at the midpoint connecting the interstitial sites (e).

implies the migration to an adjacent vacant octahedral site by means of a straight direct path with 5.26 Å of hopping distance, through two oxygen atoms, O_1 and O_2 (Fig. 4.26). The minimum energy path involves the strain of O_1 and O_2 distance by the hopping lithium ion (from 2.65 Å without Li to 4.25 Å when Li is inserted independently of composition), and to overcome a maximum barrier where the Li atom is situated in the middle position of the path, surrounded by four O atoms and two W atoms, with the same distances Li-O than Li-W (2.09 Å).

4.6.3. Intercalation of different cations

At that point, should be interesting to check how the diffusion changes when cations with higher volume than Li^+ are intercalated into the a-WO_3 film. Cyclic voltammetry at 10 mV s^{-1} for the different cations is shown in Fig 4.27. It is observed that the charge accumulated in the film decreases when bigger cations are intercalated. Chemical capacitance (by means of chronopotenciometry) and diffusion coefficients (through electrochemical impedance) of M_xWO_3 films with $M=Li^+$, Na^+ or K^+ were calculated. As observed in examining Fig. 4.28a, C_μ shows very similar behaviour regardless the type of cation inserted, particularly for low insertion levels. This fact has important implications in relation with our recently proposed model of insertion thermodynamics, where the cell voltage dependence on composition is largely determined by the host-guest interaction in case of film thickness >200 nm. Therefore, Fig. 4.28a indicates that for x<0.1 (dilute conditions) such host-guest interaction is independent of the cation size, so it would be reasonable to think that the interaction has an electrostatic origin.

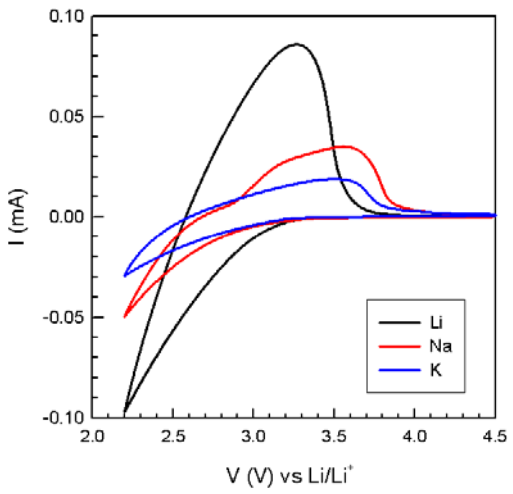

Fig. 4.27. Cyclic voltammograms at 10 mV s^{-1} for a 400 nm a-WO_3 film. Different electrolytes at 0.5 M concentration in propylene carbonate were employed in each measurement: $LiClO_4$ (black), $NaClO_4$ (red) and KCF_3SO_3 (blue).

The jump diffusion coefficient, obtained from electrochemical impedance measurements (Fig. 4.29-4.30), exhibits higher values for the smallest ion (Li^+), and decreases as the ion size enlarges (Fig. 4.28c). In all cases D_J shows lower values for high intercalation levels as reported above. The ion size effect is particularly important in case of K^+, for which D_J varies within more than three orders of magnitude. Finally, it is noted that the type of cation rather influences transport mechanisms than equilibrium properties (insertion thermodynamics)[14].

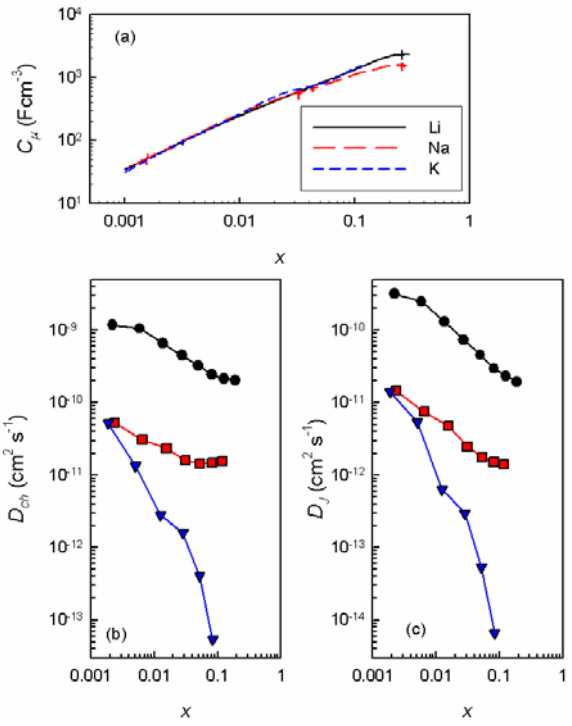

Fig. 4.28. (a) Chemical capacitance of the 400 nm a-M_xWO_3 electrodes [M = Li (solid line), Na (long dashed), and K (short dashed)] as a function of the composition (molar fraction) x. (b) Chemical diffusion coefficient extracted from electrochemical impedance measurements, and (c) jump diffusion coefficient. (●) Li, (■) Na, and (▼) K.

By applying Eq. (4.25) the activation energy for ion diffusion can be estimated assuming a hopping distance $l = 5$ Å and vibrational frequency $\nu = 1013$ s-1 as previously. Fig. 4.31 presents the variation with composition of the barrier height that for Li^+ and Na^+ exhibits a dependence that approximates the relation $\Delta E \propto ck_B T \ln x$ with $c = 0.71$ (Li^+) and $c = 0.65$ (Na^+). Similar results for lithium were presented above where $c \approx 1.25$. In both cases ΔE tends to a constant limit for $x > 0.1$ in accordance with theoretical calculations (Fig. 4.25). For K^+ diffusion, the barrier height grows rapidly as the amount of inserted ions increases.

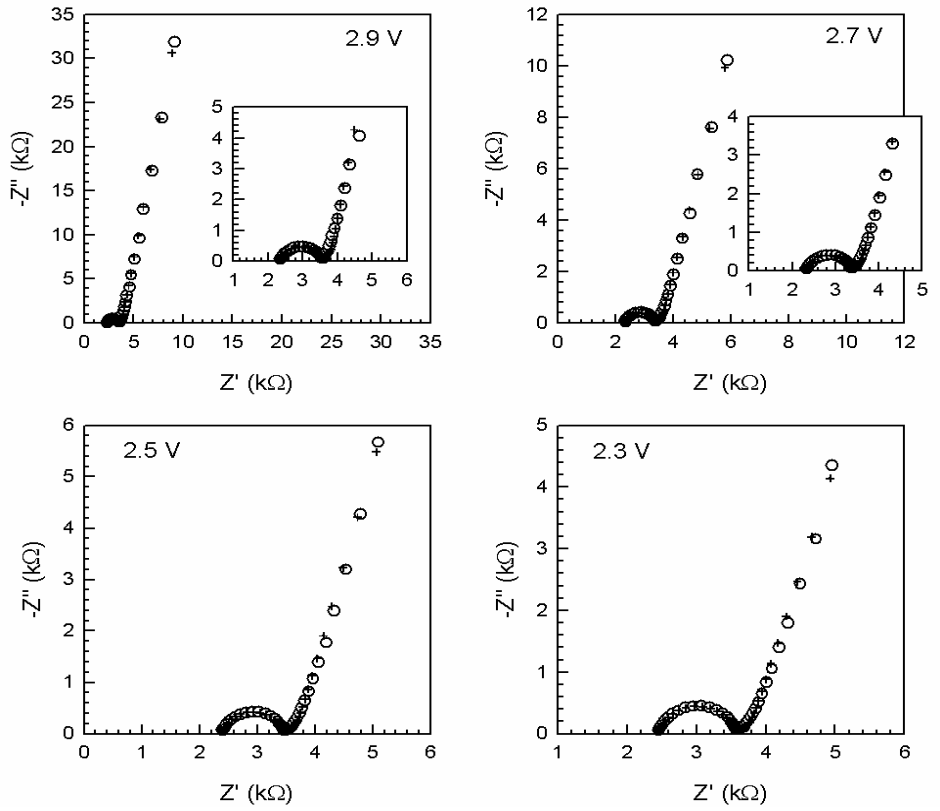

Fig. 4.29. (o) Impedance spectra of a 400 nm a-WO_3 film in a $LiClO_4$ 0.5M solution in propylene carbonate obtained in a 10 kHz-2 mHz frequency range. (+) Fits provided by the model described in Sec. 4.5. Detail of the high frequency part is given on the inset when necessary.

We can compare our results with available theories on ionic transport in amorphous systems[15, 16]. The experimentally observed values of the activation energy can be analyzed by means of the model proposed by Anderson and Stuart[17], which was specifically developed for glasses. According to this approach, the total activation energy is the sum of two parts[18], $\Delta E = \Delta E_B + \Delta E_S$. The first summand corresponds to the electrostatic binding energy assuming that the structure remains unchanged, and the second one to an additional strain energy resulting from the mechanical distortion of the lattice necessary for the ion motion, $\Delta E_S = \pi G l \left(r_+ - r_d\right)^2 / 2$. Here r_+ is the ionic radius of the cation, r_d stands for the radius of the 'doorway' the mobile ion has to open to reach the neighbouring site, and G is the shear modulus of the glass. Due to the fact

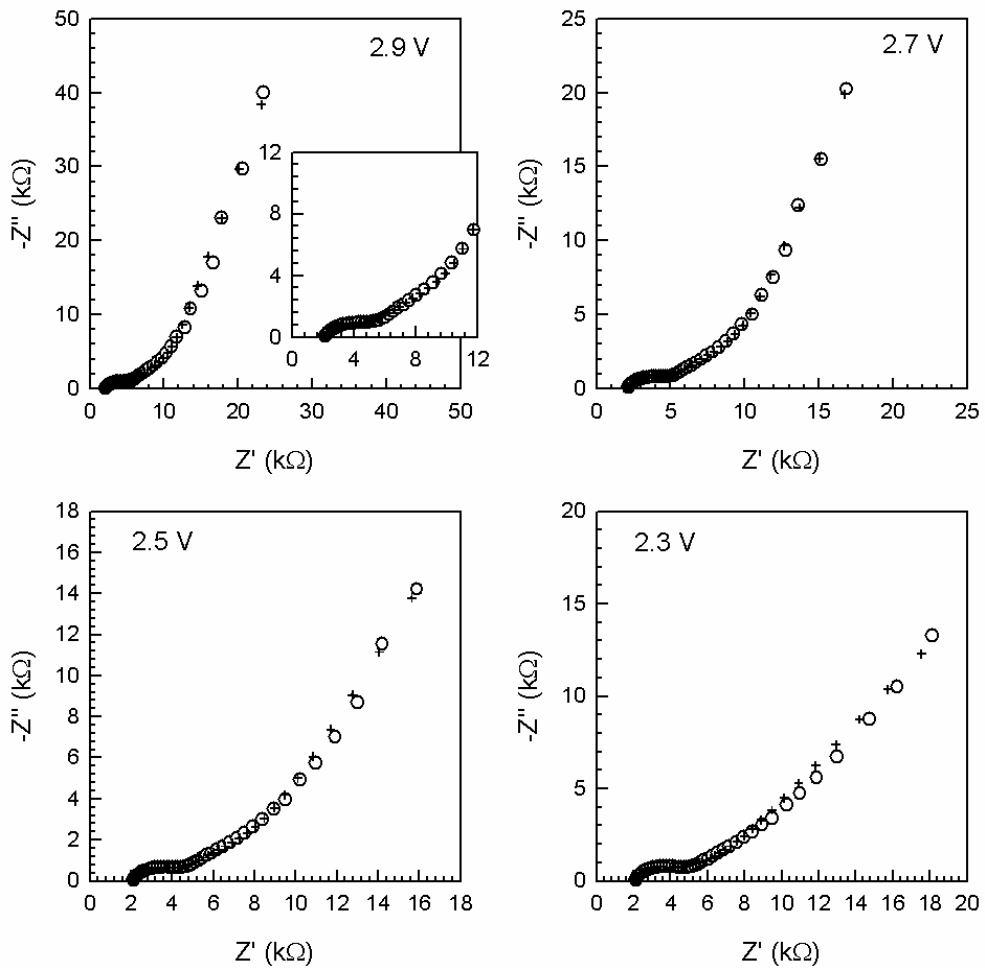

Fig. 4.30. (o) Impedance spectra of a 400 nm a-WO_3 film in a $NaClO_4$ 0.5M solution in propylene carbonate obtained in a 10 kHz-1 mHz frequency range. (+) Fits provided by the model described in Sec. 4.5. Detail of the high frequency part is given on the inset when necessary.

that WO_3 is a highly electrically polarisable material ($\varepsilon \approx 300$), the first contribution to the barrier height predicted by this model results very low $\Delta E_B \approx 50$ meV[18]. Focusing our attention on the ΔE values calculated for Li^+ and Na^+, it would be interesting to explore if the term $(r_+ - r_d)^2$ could account for such a difference, assuming similar variations of the shear modulus with composition. The ratio between activation energies is practically constant and results $\Delta E(Na^+)/\Delta E(Li^+) \approx 1.16$. Employing the following ionic radii ($r_+ = 0.76$ Å for Li^+, and $r_+ = 1.02$ Å for Na^+), it results a negative value for the 'doorway' radius, what is not coherent. In fact the channel radius is ~0.5 Å for an

octahedral cell with ~3.75 Å of side. With these parameters the activation energy ratio becomes as high as $\Delta E(\mathrm{Na}^+)/\Delta E(\mathrm{Li}^+) \approx 3.6$, what implies a barrier height larger than 1.5 eV for Na^+ diffusion. This last observation and the so different behaviour encountered for $\Delta E(\mathrm{K}^+)$ both led us to consider the Anderson-Stuart model unable to account for the reported experimental data.

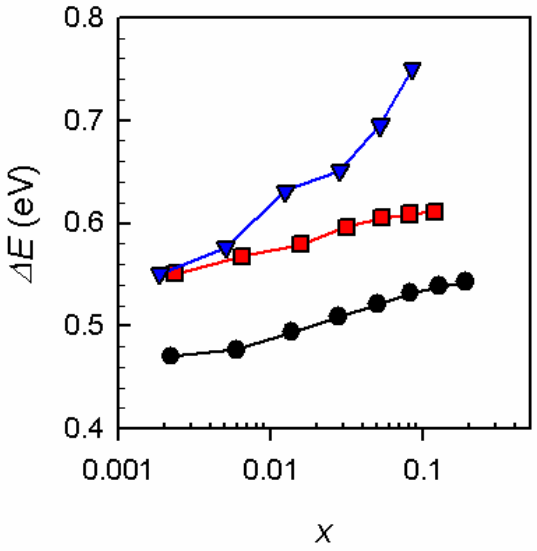

Fig. 4.31. Barrier height (activation energy) calculated from Eq. (4.25), for *a*-M_xWO_3 electrodes [M = (●) Li, (■) Na, and (▼) K]. Assuming the average hopping distance l =5 Å in these glasses and ν =10^{13} s^{-1} the vibrational frequency of a migrating ion around its equilibrium position.

4.7 Conclusions

- Several electrochemical techniques were used in order to study intercalation of Li^+ into amorphous WO_3, such as electrochemical impedance spectroscopy, chronopotenciometry and cyclic voltammetry. For a proper interpretation of the impedance spectra results, a description of the equivalent circuit was given, showing the appearance of important parameters such as the chemical capacitance and the transport resistance. Based mainly in the elements shown by the impedance results, a description of the cyclic voltammetry response was provided. The principal features of the CVs can be generated with a simple R_SC-series circuit model. The charge stored by the electroactive film during the cathodic polarization is released during the anodic polarization, yielding a peak as a result of the distortion of the purely capacitive behaviour by the series resistance effect. Therefore there is no need to introduce additional concepts. R_S shows a high value in the fits, clearly indicating than other resistive effects than the electrolyte contribution must be involved. We propose that both the ionic charge transfer on the solution/WO_3 interface as well as the resistance related to the Li^+ diffusion inside the film should be responsible of the high value of the series resistance.

- Intercalation thermodynamics from the point of view of an energy sites model has been described [Eq. (4.12)]. This model is not consistent with the asymptotic behaviour experienced by the a-WO_3 films at different thickness neither the variations of the diffusion coefficient with composition. A different approach considering lattice host distortions caused by intercalant-host interactions has been proposed [Eq. (4.14)]. The interaction parameter G that governs the interaction shows a strong variation with

thickness. For 100-nm-thick films the intercalant-host interaction plays no role so that the system can be seen as an ideal gas of non-interacting particles randomly distributed in the glassy lattice sites. An increase of G is observed at higher thicknesses, what suggests that the intercalation of Li^+ is impeded for the necessity of spending an important amount of energy in distorting the glassy host. An increment of the rigidity of the films with thickness can be the origin of the observed behaviour.

- A comparison of the thermodynamic function [Eq. (4.14)] with the previous model which describes host lattice expansions upon intercalation [Eq. (2.16)] led us to calculate volume change produced in the films. Using simple chronopotenciometry measurements, and the resulting chemical capacitance analyzed from Eq. (4.15), the volume change experienced by the film along intercalation can be calculated, which are reported to be in good agreement with direct profilometry data. We can conclude that film expansion and cell voltage are both determined by means of the underlying intercalation thermodynamics. The observation of distinct intercalation behaviour for the thinnest layers informs us about a size effect able to preclude volume change of the films, and consequently to avoid capacity losses produced after host expansion/compression upon lithium insertion/removal.

- Measurements of the diffusion coefficient and the potential barrier height for the hopping process were obtained by means of electrochemical impedance technique. Both chemical diffusion and jump diffusion coefficients decrease along intercalation, in accordance with the host distortion model proposed, where presumably the lattice distortion modifies the intersite barriers for hopping, causing an increase of the barrier heights (decrease of diffusion coefficient) with increasing extent of composition. In contrast, the opposite behaviour should be expected for the energy sites model, since

diffusion is facilitated when higher numbers of sites are available, so this model is not consistent with the experimental behaviour observed. In order to provide a better understanding of the diffusion activation energy variation observed experimentally, a simulation of the energy barrier height by means of first-principles calculations was provided assuming a crystalline structure of WO_3 instead of amorphous. In contrast to what should be expected, a good agreement between experimental and simulation was achieved. This result points out that the observed dependence $\Delta E \propto ck_BT \ln x$ is an intrinsic property of the elementary hopping process rather than a behaviour induced by the inherent disorder of the glassy structure.

- Finally, a comparison of the diffusion process using different cations (Li^+, Na^+ and K^+) was made. It was noted that the type of cation rather influences transport mechanisms than equilibrium properties (insertion thermodynamics) what led to think that host distortions are produced by means of electrostatic interactions that depend on the charge of the cation and not on its volume.

4.8 References

(1) T. Kudo and M. Hibino. *Solid State Ionics* 84 (1996) 65.

(2) M. S. Mattsson. *Phys. Rev. B* 58 (1998) 11015.

(3) E. V. Vakarin and J. P. Badiali. *Solid State Ionics* 171 (2004) 261.

(4) S. Lee, H. Miyazaki, S. D. Mahanti and S. A. Solin. *Phys. Rev. Lett.* 62 (1989) 3066–3069.

(5) G. Garcia-Belmonte, J. García-Cañadas and J. Bisquert. *J. Phys. Chem. B* 110 (2006) 4514.

(6) J. Jamnik and J. Maier. *Phys. Chem. Chem. Phys.* 5 (2003) 5215.

(7) F. Fabregat-Santiago, I. Mora-Seró, G. Garcia-Belmonte and J. Bisquert. *J. Phys. Chem. B* 107 (2003) 758.

(8) J. Bisquert. *J. Phys. Chem. B* 106 (2002) 325.

(9) J. Bisquert and A. Compte. *J. Electroanal. Chem.* 499 (2001) 112.

(10) J. García-Cañadas, F. Fabregat-Santiago, I. Porqueras, C. Person, J. Bisquert and G. Garcia-Belmonte. *Solid State Ionics* 175 (2004) 521.

(11) C. Ho, I. D. Raistrick and R. A. Huggins. *J. Electrochem. Soc.* 127 (1980) 343.

(12) J. Bisquert, G. Garcia-Belmonte and A. Pitarch. *ChemPhysChem* 4 (2003) 287.

(13) L. Gracia, J. García-Cañadas, G. Garcia-Belmonte, A. Beltrán, J. Andrés and J. Bisquert. *Electrochem. Solid St. Letters* 8 (2005) J21.

(14) G. Garcia-Belmonte, J. García-Cañadas, J. Bisquert and C. Person. *Solid State Ionics*, In press (2006)

(15) M. D. Ingram. *Phys. Chem. Glasses* 28 (1987) 215.

(16) W. Dieterich and P. Maass. *Chem. Phys.* 284 (2002) 439.

(17) O. L. Anderson and D. A. Stuart. *J. Am. Ceram. Soc.* 37 (1954) 573.

(18) S. R. Elliott. *Physics of Amorphous Materials*. Longman-Scientific (1990).

5. Conducting polymers

5. Conducting polymers

Electronically conducting polymers deposited on a conducting substrate usually show quite broad peaks that are difficult to explain from a nernstian point of view. Nevertheless a new approach based on Gaussian distribution of sites shows to provide a good explanation to the first part of the oxidation peaks.

In this chapter we will review first the existing nernstian models applied to conducting polymers. Description of the Gaussian distribution of sites model will be given afterwards and finally a comparison with experimental results on polypyrrole will be presented.

5.1 Experimental part

5.1.1. Sample preparation

Measurements were performed using polypyrrole as the conducting polymer. Films were synthesized galvanostatically on different substrates, viz. indium-doped tin oxide ITO (Delta Technologies) (15 Ω/ of surface resistance) and a Pt sheet (~1 cm^2 of active area in both cases), using acetonitrile (Baker, high purity grade), as solvent, 0.1 M $LiClO_4$ (Aldrich, >95% content) as electrolyte, and 0.1 M pyrrole (Merck) previously distilled as monomer. Constant current densities of 0.2 $mAcm^{-2}$ (ITO) and 0.4 mA cm^{-2} (Pt) were employed yielding after a sharp maximum a constant voltage near 0.75 V vs. Ag/AgCl/KCl 3M reference electrode at room temperature (see Fig. 4.2). Pt sheet was used as counter electrode. Polypyrrole films were prepared by using polymerization

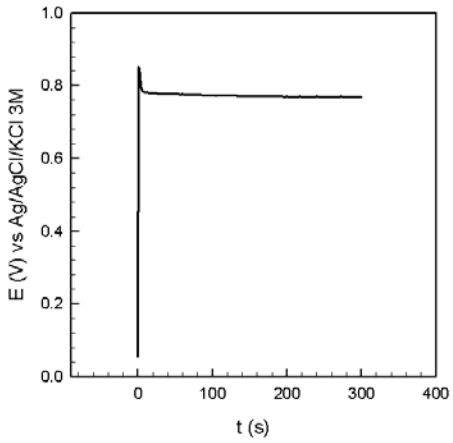

Fig. 5.1. Electrochemical polymerisation of pyrrole at 0.4 $mAcm^{-2}$ constant current onto a Pt sheet.

charges within the range of 60-120 $mCcm^{-2}$ which yielded films of estimated thickness ~120-240 nm, assuming that thickness is proportional to electropolymerisation charge (approximately 2 $\mu mC^{-1}cm^2)^1$. Then films were removed from the solution and washed in distilled water, dried in air and transferred to the three-electrode electrochemical cell where measurements were taken.

5.1.2. Electrochemical measurements

Cyclic voltammetry experiments were performed using the polymer films deposited onto ITO and Pt substrates as working electrodes, Pt sheet was used as counter electrode, and Ag/AgCl/KCl 3M electrode as reference electrode, connected to the cell by means of a salt bridge containing the electrolytic solution as reference. A solution of 0.1 M $LiClO_4$ in propylene carbonate (Merck, >99% content) was the electrolytic solution. The solutions were deoxygenated by dry nitrogen flow through the solution maintained 30 minutes prior and over the experiments. All the experiments were performed using a potentiostat-galvanostat AutoLab PGSTAT30 equipment at room temperature.

5.2 Nernstian models in conducting polymers

Electronically conducting polymers deposited on a conducting substrate can be doped and undoped electrochemically, changing the film from electrically insulating to a conducting state. Along the doping process charges are created (polarons or bipolarons) and they need to be balanced by means of counter ions from the solution that are incorporated into the polymer structure. This process produces distortions in the polymer around the oxidized or reduced positions what modifies the energy levels, which are moved into the gap region[2] (see Fig. 5.2).

The potential that is monitored in the electrochemical measurements, V, is related to the electrochemical potential of electrons in the film, which we will represent by μ for simplicity, as $V = -(\mu - \mu_{ref})/e$, with respect to the electrochemical potential in the

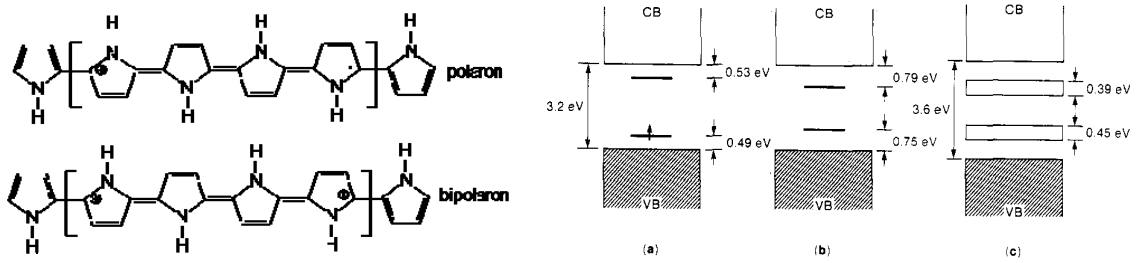

Fig. 5.2. Evolution of the band structure of polypyrrole along doping. (a) Polaron, (b) bipolaron and (c) bipolaron bands formation. On the left it is shown the structure of a polaron and a bipolaron delocalized in a 4 monomers segment.

reference electrode, μ_{ref}, which can be assumed constant. If the polymer film remains close to equilibrium during measurement, the oxidation process is described by the thermodynamic function $\mu(n)$, where n is the concentration of electrons in the conjugated system of the polymer. It is convenient to express the electrochemical potential of electrons as $\mu(p)$, where p is the density of holes (extracted electrons) in

the form of polarons (P) and bipolarons (B), taking into account that $(n+p)/2 = N_\pi$, the density of π orbitals. Theoretically, the electrochemical potential, $\mu(p)$, as a function of concentration, is derived from assumptions on the distribution and interaction of P and B species[3-7].

In a cyclic voltammetry experiment, the current is monitored as the potential varies at a constant speed, $s = dV/dt$. The electronic current density flowing into a unit volume of the polymer is

$$j = -e\frac{dn}{dt} = -e\frac{dn}{d\mu}\frac{d\mu}{dt} = se^2\frac{dn}{d\mu} = -se^2\frac{dp}{d\mu}. \qquad (5.1)$$

Therefore, the results of the voltammetry, $j(V)$, are related directly to the reciprocal of the derivative of the thermodynamic function, $\mu(p)$. As described previously (Sec. 2.2), the electrochemical capacitance (the 'redox capacity' in the specific language of conducting polymers[3]) is defined as,

$$C_\mu = e^2\frac{dn}{d\mu} = -e^2\frac{dp}{d\mu} \qquad (5.2)$$

so that voltammetry results can be expressed succinctly as

$$j = sC_\mu. \qquad (5.3)$$

Hence, $C_\mu(\mu)$ is measured directly by cyclic voltammetry. From Eq. (5.3), quasi-equilibrium conditions in cyclic voltammetry can be confirmed by an invariant $j(V)/s$ at different speeds.

The polymer is considered as a collection of N_s conjugated chain segments per unit volume, each containing m monomers. These segments describe the extension of polarons or bipolarons in the polymer chain, so that each segment contains at most one charged excitation (P or B). For instance, in polypyrrole it is considered that P or B are

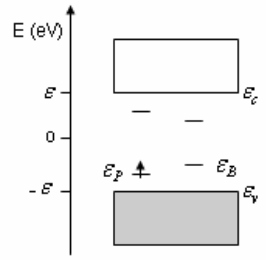

Fig. 5.3. Energy scale adopted for our description. ε_p and ε_B are the energy formation of polaron and bipolaron respectively.

extended along 4 monomer units[2]. Taking the energy reference at the center of the gap of width 2ε, the energy for adding an electron is $\varepsilon_c = \varepsilon$, and the energy for extracting an electron (adding a hole to the valence band) is $\varepsilon_v = -\varepsilon$. When a hole is added to the polymer, relaxation of the atomic positions will occur extremely rapid. The energy of the polaron formation, $-\varepsilon_P$, is lower than that of the unrelaxed hole, ε_v. Further, a double charged excitation, the bipolaron, can be formed in the conjugated chain segment[2, 8] with a total energy of formation $-\varepsilon_B$. If only P can be formed, their density is given by

$$n_P = N_s f_P(\mu, \varepsilon_P) \tag{5.4}$$

where the distribution function f_P is the Fermi-Dirac function for holes, shown in Fig. 5.4a,

$$f_P(\mu, \varepsilon_P) = \frac{1}{1 + e^{(\varepsilon_P + \mu)/k_B T}} \tag{5.5}$$

The chemical capacitance of polarons

$$C_\mu = -N_s e^2 \frac{df_P}{d\mu} \tag{5.6}$$

has the value

$$C_\mu = \frac{N_s e^2}{k_B T} f_P(1 - f_P)\,. \tag{5.7}$$

This is the standard form of the 'redox capacitance' for a nernstian species[3], Fig. 5.4b. It forms a peak at the standard potential ($f_P(\mu_0, \varepsilon_P)$=1/2), with a slope of 60 mV/decade at the cathodic side. Note that Eq. (5.5) is the Langmuir isotherm and takes also the form of the Nernst expression

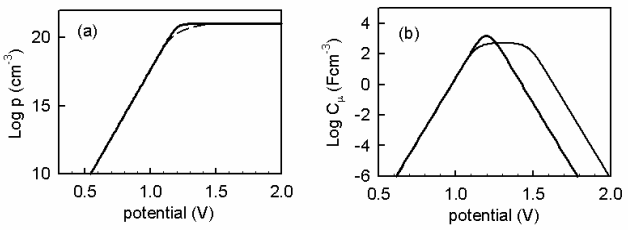

Fig. 5.4. (a) Density of polarons, n_P, for a density of conjugated chain segments N_s =10^{21}cm^{-3}, with energy ε_P =1.2 eV, in the absence of formation of bipolarons. (b) The chemical capacitance per unit volume. The thin lines show the same system with a mean field repulsive interaction that contributes a term $8\,k_BTn_P^{\,2}/2$ to the free energy.

$$\mu = -\varepsilon - k_BT \ln \frac{n_P}{N_s - n_P}.$$

Interactions are often treated with the mean-field approximation. In this model the local interactions are replaced by an averaged field (molecular field) which is determined by the distribution of electrons and which in turn governs the distribution itself[9]. The result is

$$\mu = -\varepsilon - k_BT \ln \frac{n_P}{N_v - n_P} - bk_BTn_P \tag{5.9}$$

where b is the dimensionless interaction parameter, which typically has a value ~4, for an interaction energy of 100 meV per particle. For reasonable values of b the interaction term of Eq. (5.9) becomes significant only at very high concentration and does not modify the nernstian slope of the chemical capacitance, as shown in Fig. 5.4b, for a relatively large interaction constant b =8.

Many studies based on simultaneous voltammetry and spin relaxation (ESR) have demonstrated that the oxidation of conducting polymers involves both P and B with densities n_P and n_B [10-12]. In this case there will be chain segments either empty, singly or doubly occupied by holes among the available number N_s. The free energy takes the form

$$F = (\varepsilon_P + \mu)n_P + (\varepsilon_B + 2\mu)n_B - k_BT \ln \Omega \tag{5.10}$$

where the number of arrangements is given by,

$$\Omega = \frac{N_s!}{(N_s - n_P - n_B)!n_P!n_B!} \tag{5.11}$$

and using the Stirling approximation one obtains,

$$F = (\varepsilon_P + \mu)n_P + (\varepsilon_B + 2\mu)n_B + k_B T\left(n_P \ln\frac{n_P}{n_0} + n_B \ln\frac{n_B}{n_0} - N_s \ln\frac{N_s}{n_0} \right) \tag{5.12}$$

The result of minimizing F gives the expressions[10]

$$-\mu = \varepsilon_P + k_B T \ln\frac{n_P}{n_0} \tag{5.13}$$

$$-\mu = \varepsilon_B - \varepsilon_P + k_B T \ln\frac{n_B}{n_P}. \tag{5.14}$$

The Eqs. (5.13, 5.14) correspond to equilibrium ratios of the reactions $\mathrm{A} \leftrightarrow \mathrm{P}^+ + e^-$ and $\mathrm{P}^+ \leftrightarrow \mathrm{B}^{++} + e^-$ where A is a neutral segment, with density $n_0 = N_s - n_P - n_B$. Eqs. (5.13) and (5.14) provide the distribution functions[5, 13]

$$f_P(\mu, \varepsilon_P, \varepsilon_B) = \frac{1}{1 + e^{(\varepsilon_P + \mu)/k_B T} + e^{-(\varepsilon_B - \varepsilon_B + \mu)/k_B T}} \tag{5.15}$$

$$f_B(\mu, \varepsilon_P, \varepsilon_B) = \frac{1}{1 + e^{2(\varepsilon_B/2 + \mu)/k_B T} + e^{(\varepsilon_B - \varepsilon_B + \mu)/k_B T}} \tag{5.16}$$

The densities of P and B are given by

$$n_P = N_s f_P(\mu, \varepsilon_P, \varepsilon_B) \tag{5.17}$$

$$n_B = N_s f_B(\mu, \varepsilon_P, \varepsilon_B) \tag{5.18}$$

The densities of P and B are equal, $n_P(\mu_2) = n_B(\mu_2)$, at the potential

$$\mu_2 = -\varepsilon_B + \varepsilon_P \tag{5.19}$$

Further, $n_P(\mu_1) = n_0(\mu_1)$ at the potential

$$\mu_1 = -\varepsilon_P \tag{5.20}$$

Chemical capacitances are given by the expressions

$$C_\mu^{\ P} = -N_s e^2 \frac{df_P}{d\mu}(\mu, \varepsilon_P, \varepsilon_B) \tag{5.21}$$

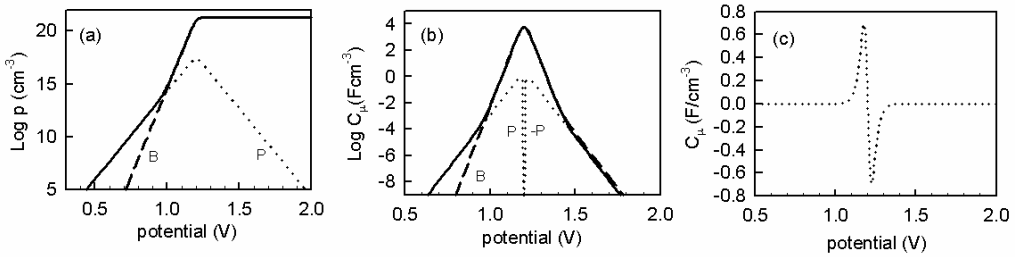

Fig. 5.5. (a) Densities of polarons, n_P, holes in bipolarons, $2n_B$, and total holes, $n_P + 2n_B$ (thick line), for a density of conjugated chain segments N_s =10^{21} cm^{-3}, with energies ε_P =1.4 eV and ε_B =2.4 eV as a function of potential, and (b) the corresponding partial and total chemical capacitances per unit volume, in logarythmic scale. The line (-P) is a negative capacitance contribution of polarons. (c) The partial capacitance of polarons in linear scale.

$$C_\mu^{\ B} = -2N_s e^2 \frac{df_B}{d\mu}(\mu, \varepsilon_P, \varepsilon_B) \tag{5.22}$$

which can be calculated readily from Eqs. (5.15) and (5.16), but are not written here explicitly. The results of the P-B model with single formation energies are illustrated in Fig. 5.5 for the case in which B are energetically favoured ($\varepsilon_B < 2\varepsilon_P$). Initially the oxidation process is dominated by Ps, Fig. 5.5a, but Bs become predominant at potential μ_1, and the concentration of B stabilizes after $\mu_3 = \varepsilon_P - \varepsilon_B/2$ (where $f_B \approx 1/2$). It is interesting to note that the density of P shows a maximum at μ_3 and decreases monotonically thereafter[5]. This behaviour is reported in ESR measurements[10-12].

The chemical capacitance, shown in Fig. 5.5b, shows first a 60 mV and then 30 mV/decade variation, corresponding to the regions dominated by formation of P and B, respectively. Then a peak centred in μ_3 is observed. It is important to recognize the peculiar behaviour of the partial chemical capacitance of the polarons. This capacitance switches suddenly to a negative value at the potential μ_3. Similar features occur when the P are more stable than B, Fig. 5.6. This negative capacitance feature occurs because the density of polarons is decreasing even though their own driving force for formation is becoming larger, i.e., the Fermi level μ is moving further below the energy $-\varepsilon_P$. Of

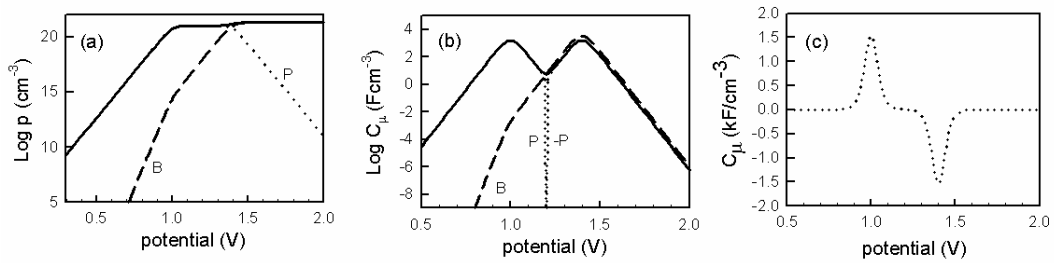

Fig. 5.6. Same as Fig. 5.5, with energies ε_P =1.0 eV and ε_B =2.4 eV.

course the emptying process of the polaron level is related to an even larger driving force for B formation by recombination of P pairs.

In conclusion to this section, all the models reviewed have in common that the formation of polarons is governed by the Fermi level crossing a well defined energy level in the gap. This leads to basically Boltzmann-Nernst dependence in the chemical capacitance, which forms asymptotically a straight line (in semilog representation) of slope 30 mV for bipolarons, 60 mV for polarons, 120 mV for polarons and ions, etc.

5.3 Gaussian distribution model

In spite of the widespread use of the single energy models outlined in the previous section in electrochemistry measurements, it is also widely accepted that the energies of P and B states in the bandgap form a wide distribution. This was first inferred from the broadening of the absorption spectra. In polypyrrole, bands of ~0.4 eV width where ascribed to overlap between bipolaron states[2]. Specifically it was shown that the Gaussian distribution in conducting polymers is caused by the fluctuation of the lattice polarization energies[14], dipole interactions[15] and molecular geometry fluctuations[16].

It is possible to give an a priori estimation of the width of the distribution[14]. Absorption (and fluorescent) bands of disordered organic solids are usually of Gaussian shape with a standard deviation of typically 60 meV. Comparing the interactions with the surrounding lattice between an exciton and a charge carrier it is demonstrated that the width of the density of states for charge carriers is about 1.5 times as big as that for singlet excitation. Hence the width should be of order 100 meV. In addition, optical absoption spectroscopy and spectral dispersion measurements show that the neutral exciton excited states have a Gaussian energy distribution[17].

For only one species (P) we consider that the N_s chain segments per unit volume are distributed in energy according to the Gaussian expression with mean energy $\varepsilon_P{}^0$ and half-width σ_P,

$$g(\varepsilon) = \frac{N_s}{\sqrt{2\pi}\,\sigma_P} \exp\left[-\frac{(\varepsilon - \varepsilon_P{}^0)^2}{2\sigma_P{}^2} \right]. \tag{5.23}$$

The derivation of the statistical function assumes a random distribution of the P among the available levels, the number of sites for each level ε being given by Eq.

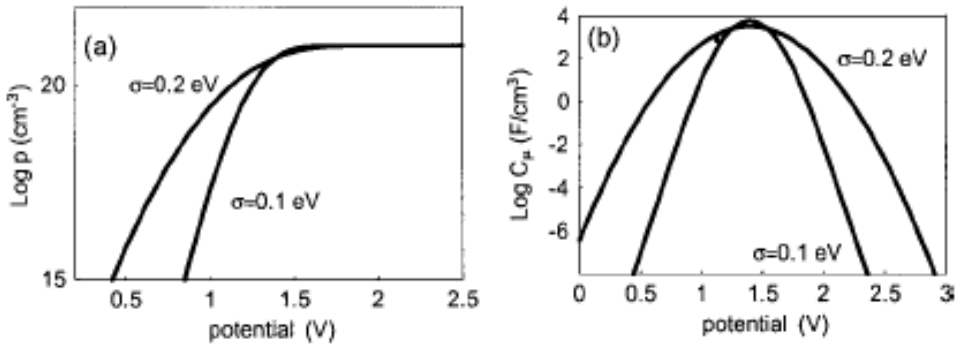

Fig. 5.7. (a) Densities of polarons, n_P, as a function of potential, for a density of conjugated chain segments N_s =10^{21}cm^{-3}. The energies of P have a Gaussian distribution with mean values $\varepsilon_P{}^0$ =1.4 eV and variances σ_P as indicated. (b) The corresponding chemical capacitances, per unit volume in logarithmic scale.

(5.23). The total number of arrangements, Ω, is the product of the number of arrangements for each level. A straightforward calculation shows that the result of minimizing the free energy is given by Eq. (5.5), $f(\mu,\varepsilon)$, for the energy level ε. The total number of polarons, as a function of the electrochemical potential, is obtained by integration

$$n_P = \int_{-\infty}^{+\infty} g(\varepsilon) f_P(\mu,\varepsilon) d\varepsilon \,. \tag{5.24}$$

The chemical capacitance is given by

$$C_\mu = -e^2 \int_{-\infty}^{+\infty} g(\varepsilon) \frac{df_P}{d\mu}(\mu,\varepsilon) d\varepsilon \,. \tag{5.25}$$

Observing in Eq. (5.5) that $df_P / d\mu = df_P / d\varepsilon$, integrating Eq. (5.25) by parts and using the zero-temperature limit of the Fermi distribution, Eq. (5.25) can be expressed as

$$C_\mu = e^2 g(-\mu) \tag{5.26}$$

so that the chemical capacitance as a function of potential corresponds to the density of states function at the energy level $\varepsilon = -\mu$. This shows that the shape of the cyclic voltammogram peak relates directly to the shape of the distribution.

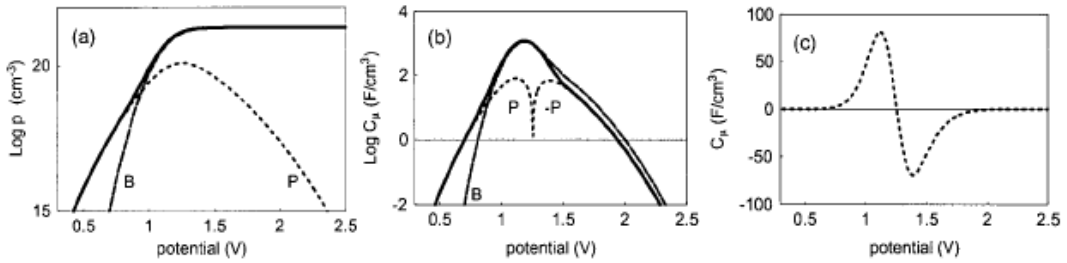

Fig. 5.8. (a) Densities of polarons, n_P, holes in bipolarons, $2n_B$, and holes, $n_P + 2n_B$ (thick line), as a function of potential, for a density of conjugated chain segments N_s =10^{21} cm^{-3}. The energies of both P and B have a Gaussian distribution with mean values $\varepsilon_P{}^0$ =1.4 eV and $\varepsilon_B{}^0$ =2.4 eV and variances σ_P =0.1 eV, σ_B =0.2 eV. (b) The corresponding partial and total chemical capacitances, per unit volume in logarythmic scale. The line (-P) is a negative capacitance contribution of polarons. (c) The partial capacitance of polarons in linear scale.

These results are illustrated in Fig. 5.7. The main contrast with respect to the previous models is that the chemical capacitance vs. potential does not form a straight asymptotic line in the semilog representation. Indeed, the chemical capacitance is a parabola, Eqs. (5.23) and (5.26), so that $\log C_\mu$ shows straight wings when plotted vs. $(\mu + \varepsilon_P{}^0)^2$. We remark also the very broad oxidation peaks that are obtained for characteristic values of the half width of the distribution.

This approach can be readily extended to the case in which both P and B can be formed upon oxidation. If we describe each species with its own characteristic energy and spread, the density of states becomes

$$g(\varepsilon,\varepsilon') = \frac{N_s}{2\pi\sigma_P\sigma_B}\exp\left[-\frac{(\varepsilon-\varepsilon_P{}^0)^2}{2\sigma_P{}^2}-\frac{(\varepsilon'-\varepsilon_B{}^0)^2}{2\sigma_B{}^2}\right]. \tag{5.27}$$

The statistical functions are obtained from the product of terms as Eq. (5.11) for each energy level. The number of polarons is described by the expression

$$n_P = \int_{-\infty}^{+\infty} g(\varepsilon,\varepsilon')\, f_P(\mu,\varepsilon,\varepsilon')\, d\varepsilon d\varepsilon' \tag{5.28}$$

where $f_P(\mu,\varepsilon,\varepsilon')$ is given in Eq. (5.15). For B, we get

$$n_B = \int_{-\infty}^{+\infty} g(\varepsilon,\varepsilon') f_B(\mu,\varepsilon,\varepsilon') d\varepsilon d\varepsilon' \tag{5.29}$$

where $f_B(\mu,\varepsilon,\varepsilon')$ is the function in Eq. (5.16).

The chemical capacitances take the forms,

$$C_\mu{}^P = -e^2 \int_{-\infty}^{+\infty} g(\varepsilon,\varepsilon') \frac{df_P}{d\mu}(\mu,\varepsilon,\varepsilon') d\varepsilon \tag{5.30}$$

$$C_\mu{}^B = -e^2 \int_{-\infty}^{+\infty} g(\varepsilon,\varepsilon') \frac{df_B}{d\mu}(\mu,\varepsilon,\varepsilon') d\varepsilon \,. \tag{5.31}$$

The results of the Gaussian distribution for both P and B are illustrated in Figs. 5.8-5.10. Note that the formation of two well resolved peaks, as in Fig. 5.6, is precluded by the distribution of energy levels of each species, P and B.

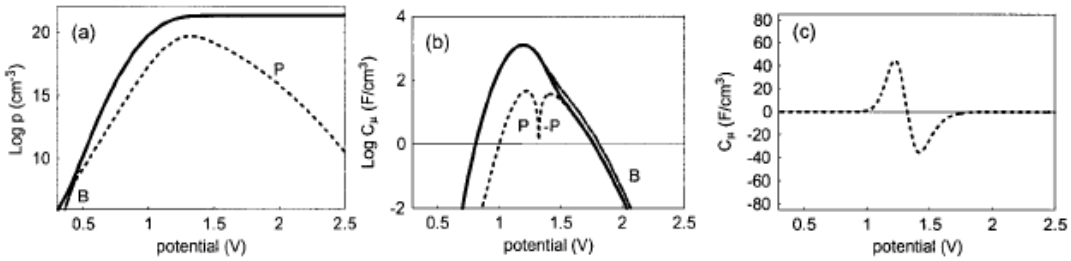

Fig. 5.9. Same as Fig. 5.8 for a Gaussian distribution of P and B with mean values with energies ε_P^0 =1.4 eV and ε_B^0 =2.4 eV and variances $\sigma_P = \sigma_B$ =0.2 eV.

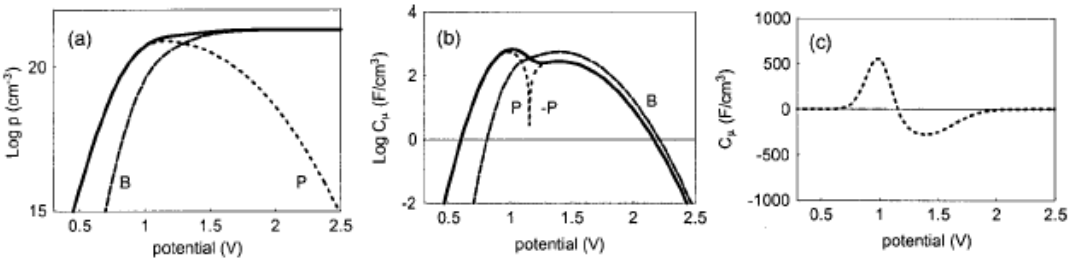

Fig. 5.10. Same as Fig. 5.8 for a Gaussian distribution of P and B with mean values with energies ε_P =1.0 eV and ε_B =2.4 eV and variances σ_P =0.1 eV, σ_B =0.2 eV.

5.4 Fitting of voltammograms

The voltammetry of conducting polymers, including oxidation and reduction peaks, shows a number of general features that are well described in the literature[5, 6, 11, 18]. Beyond the oxidation peak the voltammetry shows a current plateau and the subsequent reduction peak is broader and displaced from the oxidation peak. We are mainly interested in the experimental aspects of conducting polymers that can be described by molecular-statistical models corresponding to thermodynamic equilibrium. Considering the quasi-equilibrium part of the oxidation peak, it is shown that the model based on the Gaussian distribution of energies provides an excellent description of the changes in the polymer while it is doped electrochemically.

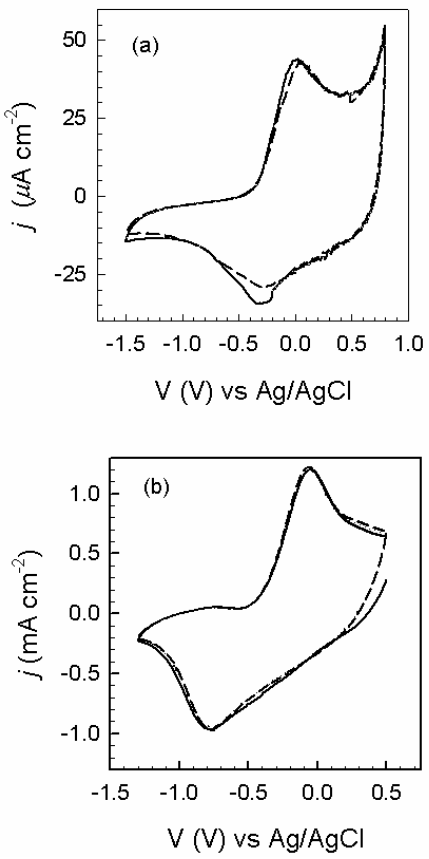

Fig. 5.11. Stable cyclic voltammograms of polypyrrole films (current per unit film area) in a solution of 0.1 M $LiClO_4$ in propylene carbonate. (a) Onto ITO substrate and 60 $mCcm^{-2}$ of polymerization charge.Scan rate was 10 mV s^{-1}. (b) Onto Pt substrate and 120 $mCcm^{-2}$ of polymerization charge.Scan rate was 50 mV s^{-1}.

In order to collect experimental results, cyclic voltammetry experiments of polypyrrole films were performed. Reproducible voltammetric behavior was attained after the first ~5 scans. Some examples of this stable response are shown in Fig. 5.11 for films deposited on different substrates. In all cases CVs present similar characteristics: a rather broadened oxidation peak appears during the positive sweep at about 0.0 V vs. Ag/AgCl for

scan rates within the range 10-50 mVs^{-1}, followed by a current plateau at more positive potentials. For thin films and low scan rates (usual experimental conditions to preclude kinetic limitations) the registered current is directly connected to the chemical capacitance of the polymer film as Eq. (5.3) because the potential applied V is very close to that governing the charging process.

As previously commented, our work is focused to the particular pattern exhibited by CVs experiments for potentials in the vicinity of the oxidation peak. Fig. 5.11 shows CV characteristic responses of two polypyrrole films deposited onto different electrodes and the comparison to different models. We note first that the peaks are too broad to be interpreted in terms of simple nernstian statistics. The width at half-heigth of the oxidation peaks (~300 mV calculated from the anodic part of such peaks) is always quite high as compared to the nersnstian widths of 90.6 mV or 181.2 mV for one and two species, respectively. Moreover, the current asymptotes predicted by these models yield linear relationships of the form $\log j \propto (eV - \varepsilon)/mk_{B}T$, in which m relates to the number of species involved, as discussed in Sec. 5.2. By examining Fig. 5.12b one can realize that the slope of the anodic part of the oxidation peak (in log-linear representation) is not constant, but decreases monotonically as the peak potential is reached. These are strong indications that the nernstian models (shown in Fig. 5.12b for comparison) are unable to explain the main features of the observed oxidation process.

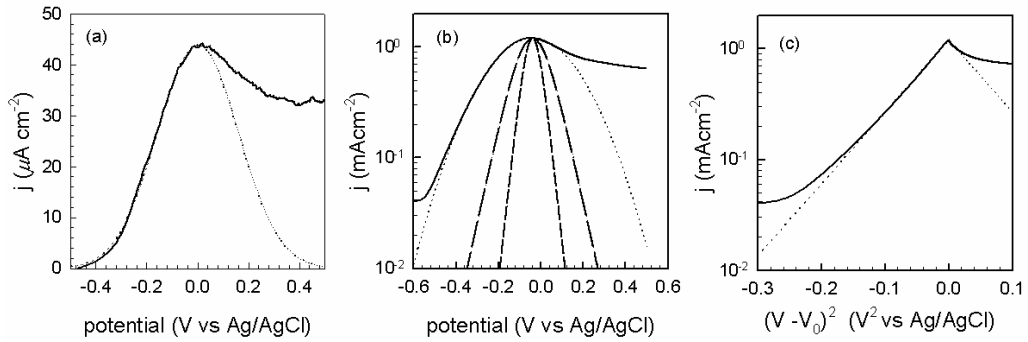

Fig. 5.12. (a) Comparison between CV response for potentials near the oxidation peak of polypyrrole films onto ITO substrate and 60 mC cm^{-2} of polymerization charge (continous) and fit (dotted) using a Gaussian distribution of states (σ =160 meV, ε^0 =1.0 meV and N_s =1.8×10^{21} cm^{-3}). (b) Comparison between CV response (log current) for potentials near the oxidation peak of polypyrrole films onto Pt substrate and 120 mCcm^{-2} of polymerization charge (continous) and fit (dotted) using a Gaussian distribution of states (σ =183 meV, ε^0 =-38 meV and N_s 5.7×10^{21} cm^{-3}). Dashed lines correspond to nernstian behavior for one (short, 60 mV/decade) and two (long, 120 mV/decade) species involved in the thermodynamics of doping. (c) Same data as (a) highlighting the quadratic dependence predicted by Eqs. (5.23) and (5.26) $\log j \propto \left[(eU-\varepsilon^0)/k_{\mathrm{B}}T\right]^2$.

In contrast, using a Gaussian distribution of sites energies we obtain readily the observed features[19]. Indeed, the theoretical plot in Fig. 5.7 shows that reasonable distributions of half width between 100 and 200 meV provide very broad oxidation peaks. In addition, the current asymptotes in Fig. 5.7 are not linear due to the parabolic shape implied by the Gaussian distribution.

We therefore consider the fit of the measured peaks to the Gaussian distribution. As observed in Fig. 5.12a, for the polypyrrole film deposited on ITO, excellent fit is obtained for the anodic part of the oxidation peak whilst the cathodic part is dominated by a current plateau. Figure 5.12b, for the polypyrrole film on Pt, shows also the excellent fit of the Gaussian model. Values of $\sigma \approx 170$ meV and $N_s \approx 10^{21}$ cm^{-3} have been obtained from these fits. Fig. 5.12b also shows that the Gaussian provides a much better agreement than nernstian models for either one or two species. Finally, the $j(V)$ dependence predicted from the Gaussian model, Eqs. 5.23 and 5.26, $\log j \propto \left[(eV-\varepsilon^0)/k_{\mathrm{B}}T\right]^2$, is emphasized in Fig. 5.12c. The representation with

$\left[(eV-\varepsilon^0)/k_BT\right]^2$ in the x-axis shows clearly the Gaussian form of the chemical capacitance, when the current raises above the background level in the anodic direction. In conclusion, the oxidation peak of polypyrrole (before the current plateau) is well described by the Gaussian distribution model.

We remark that CV experiments only show a well-defined oxidation peak which precludes a direct interpretation in terms of either polarons or bipolarons. Nevertheless the formation of bipolarons is believed to be energetically favoured so that it is likely that the dispersion calculated, σ~0.2 eV, should correspond to the energy spreading of bipolaron sites. Further resolution of the electronic species (polarons and bipolarons) involved in these peaks, and their distributions of energies, requires the combined analysis of both current (CV) and spin density (spectroelectrochemical ESR) with respect to change of potential.

The observed behaviour of the system beyond the oxidation peak is still a topic under discussion. It is thought to be caused by a capacitive behaviour but it is not well understood yet.

5.5 Conclusions

The implications of random statistical distribution functions of polarons and bipolarons in conducting polymers for electrochemical measurements in quasi-equilibrium have been discussed. The chemical capacitance with respect to the potential, in log-linear representation, shows basically a linear dependence in nernstian (single energy) models and a parabolic dependence in the presence of a Gaussian distribution of site energies. These dependences provide an important tool for analyzing the distribution of polarons and bipolarons energy levels. In nernstian model the peak is related to 1/2 occupancy of a single class of site. In contrast, in the Gaussian distribution of energies the shape of the peak is determined by the shape of the distribution. It was found that the broad oxidation peaks usually observed in polypyrrole can be explained by a wide Gaussian distribution of energies (half width $\sigma \approx 170$ meV), attributed to bipolarons.

5.6 References

(1) R. A. Bull, F.-R. F. Fan and A. J. Bard. *J. Electrochem. Soc.* 129 (1982) 1009.

(2) J. L. Brédas and G. B. Street. *Acc. Chem. Res.* 18 (1985) 309.

(3) C. E. D. Chidsey and R. W. Murray. *J. Phys. Chem.* 90 (1986) 1479.

(4) M. A. Vorotyntsev and J. P. Badiali. *Electrochim. Acta* 39 (1994) 289.

(5) G. Paasch, P. H. Nguyen and A. J. Fischer. *Chem. Phys.* 227 (1998) 219.

(6) M. A. Vorotyntsev and J. Heinze. *Electrochim. Acta* 46 (2001) 3309.

(7) D. Posadas, R. M. J. Presa and M. I. Florit. *Electrochim. Acta* 46 (2001) 4075.

(8) J. C. Scott, P. Pfluger, M. T. Krounbi and G. B. Street. *Phys. Rev. B* 28 (1983) 2140.

(9) R. Kubo. *Statistical Mechanics*. North-Holland (1965).

(10) F. Genoud, M. Guglielmi and M. Nechtschein. *Phys. Rev. Lett.* 55 (1985) 118.

(11) W. J. Albery, Z. Chen, B. R. Horrocks, A. R. Mount, P. J. Wilson, D. Bloor, A. T. Monkman and C. M. Elliott. *Faraday Discuss. Chem. Soc.* 88 (1989) 247.

(12) J. Tang, R. D. Allendoerfer and R. A. Osteryoung. *J. Phys. Chem.* 96 (1992) 3531.

(13) A. Saxena and J. D. Gunton. *Phys. Rev. B* 35 (1987) 3914.

(14) H. Bässler. *Phys. Stat. Sol. (b)* 175 (1993) 15.

(15) A. Dieckmann, H. Bassler and P. M. Borsenberger. *Journal of Chemical Physics* 99 (1993) 8136.

(16) Z. G. Yu, D. L. Smith, A. Saxena, R. L. Martin and A. R. Bishop. *Phys. Rev. B* 63 (2001) 085202.

(17) D. D. C. Bradley. *Synthetic Met.* 54 (1993) 401.

(18) S. Feldberg. *J. Am. Chem. Soc.* 106 (1984) 4671.

(19) J. Bisquert, G. Garcia-Belmonte and J. García-Cañadas. *Journal of Chemical Physics* 120 (2004) 6726.

6. Viologen modified n-TiO_2 electrode

6. Viologen modified n-TiO_2 electrode

In this chapter we study the dynamic response of viologen–activated nanostructured titanium dioxide by means of electrochemical impedance, cyclic voltammetry and optical voltammetry (registers the transmittance change along the voltammogram). Since the charge transfer between the TiO_2 nanoparticles and the attached viologen molecules is considered to be very fast, the state of charge of the semiconductor network is the key factor mediating between the electrode potential and colouration of viologen. Study of the relation between the chemical capacitance, the applied voltage and the extent of colouration is the aim of this chapter.

Our strategy is to use the electrochemical impedance technique information as an input for describing the correlation of the response of cyclic and optical voltammetry. We will first characterise the capacitance of the electrode as a function of potential by means of electrochemical impedance, identifying the contribution of the different elements in the film that dominate at each voltage region. These features will be subsequently used to interpret the voltammograms and the transmittance change that are obtained when the adsorbed viologen is reduced and oxidized during a potential scan. The quantitative contribution of the viologen molecules to the electrical current is estimated and finally, the redox process of viologen is decoupled completely from the TiO_2 response and depicted separately by means of transmittance data[1].

6.1 Experimental part

The viologen bis(2-phosphonoethyl)-4,4'-bipyridinium dichloride was synthesised as described by Cummins et al.[2]. Phosphonate groups are necessary for a proper anchoring of the viologen molecules with the substrate. Conductive glass substrate (Hartford glass, TEC8, fluorine-doped SnO_2, from now FTO) were cleaned by rinsing with 99% EtOH and dried in air. Colloidal solution of nanocrystalline TiO_2 (particle size of 10-14 nm), was spread over the cleaned conductive glass surface with a glass rod, using single layers of Scotch tape as spacers and fired at 450 ºC for 30 min in air. Immediately after cooling the samples were immersed in a 0.5 mM solution of viologen in methanol. Chemisorption of viologen onto the TiO_2 surface was allowed to proceed overnight, and then the samples were taken out from the solution and dried in air. Two TiO_2 samples of the same batch were used in this study: the first one was derivatised with viologen while the second was kept free to be used for blank measurements. Their geometric areas were 1 and 0.68 cm^2 respectivley and their average thickness 4 μm.

Electrochemical measurements were carried out in a three-electrode cell under

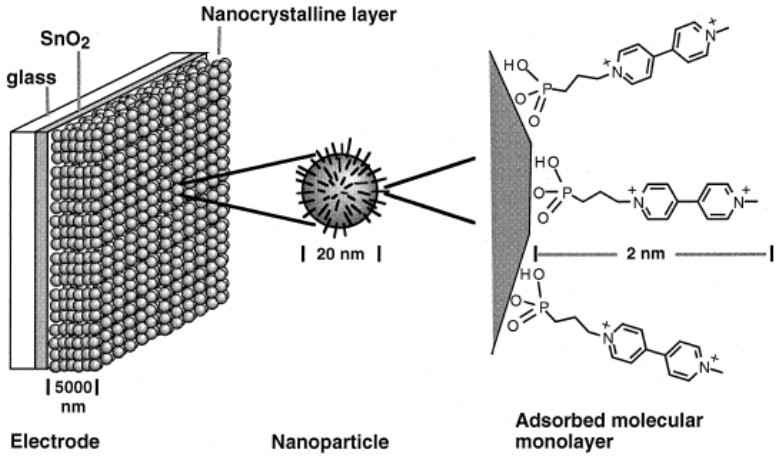

Fig. 6.1. Scheme of the n-TiO_2 electrode modified with viologen molecules. Lengths indicated are an approximation of the magnitude order of the parts involved.

nitrogen. A Ag/AgCl/KCl (3M) reference electrode was connected to the cell by means of a salt bridge containing the electrolyte solution and a Pt wire was used as counter electrode. The electrolyte solution was 0.2 M lithium triflate (Aldrich) in 3-methoxypropionitrile (Aldrich). Electrochemical impedance measurements were performed at a 10 mV potential modulation in the 1kHz to 5 mHz frequency range. The optical transmittance was measured simultaneously to the votammetries by illuminating the cell from the substrate side with a He-Ne laser (wavelength 543.5 nm) and collecting the transmitted light with a silicon photodetector.

6.2 Impedance analysis

Providing that high speeds of electron transfer, both to the TiO_2 nanostructure and between the oxide surface and the attached molecules are obtained, the crucial factor controlling the colouration is the charge density in the nanoporous network at each potential value. A quantitative description of capacitance and interfacial charge transfer of nanostructured TiO_2 electrodes can be achieved using electrochemical impedance spectroscopy technique[3] and cyclic voltammetry[4]. We start from the idea that the opacity of the film will be determined by electron density in the semiconductor nanoparticles.

By means of electrochemical impedance technique applied on both bare n-TiO_2 and viologen modified TiO_2 electrode, we can find out how the capacitance of the systems evolves with the electrode potential. The impedance spectra of the samples at the lower and higher potentials have the same shape in both cases (Fig. 6.2a). This response can be roughly modelled by the series connection of a resistance R and a capacitance C. The latter can be estimated by the low frequency limit of the capacitance spectra (Fig.

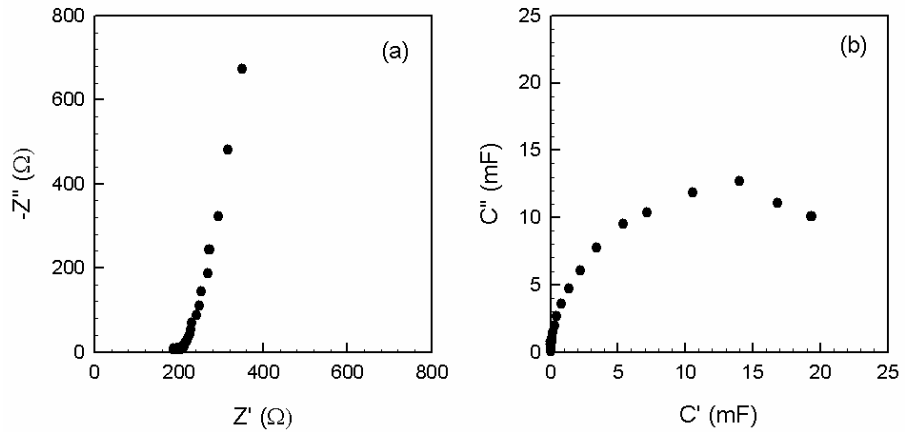

Fig. 6.2. Impedance spectra (a) and capacitive representation (b) of a viologen modified TiO_2 at -0.6 V vs Ag/AgCl/KCl 3M. Capacitance value can be estimated by the low frequency limit of (b).

(a)

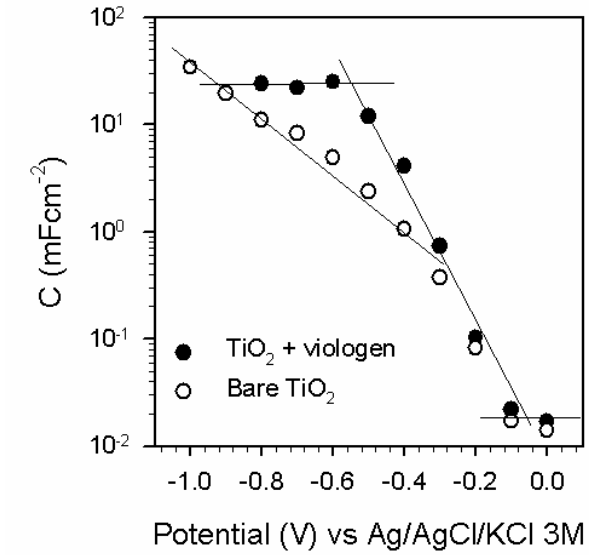

(b)

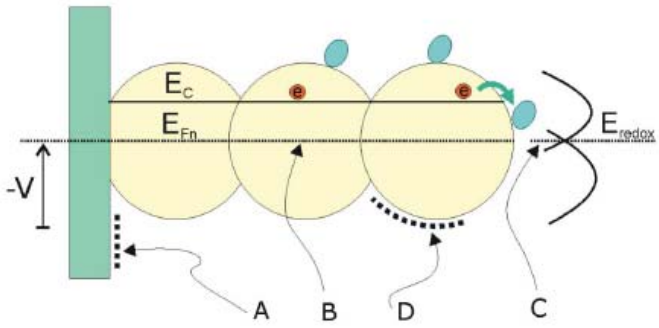

Fig. 6.3. (a) Capacitance of bare (o) and viologen activated TiO_2 (•) obtained from impedance measurements. The lines are a guide to indicate different domains of behaviour. (b) Scheme of a nanoporous electrode with attached viologen molecules, showing the different capacitive processes that contribute to the experimental response. (A) Capacitance of the Helmholtz layer at the interface between the exposed surface of the conducting substrate and the electrolyte. (B) Chemical capacitance due to increasing chemical potential (concentration) of electrons in the TiO_2 phase, obtained when the electrode potential, V, displaces the electron Fermi level, E_F, with respect to the lower edge of the conduction band, E_c, in the semiconductor nanoparticles. (C) Chemical capacitance due to the redox process occurring when the semiconductor Fermi level, E_F, displaces the redox potential E_{redox} of the viologen molecules. (D) Constant Helmholtz capacitance at the oxide/electrolyte interface.

6.2b).

From the fits of the high frequency part to a simple *RC* equivalent circuit, we obtained a series resistance of 200 Ω, which is the sum of the FTO (~40 Ω) and electrolyte resistance, and the voltage dependent capacitances shown in Fig. 6.3a. The interpretation of the different components of the capacitance is indicated in the scheme of Fig. 6.3b. In the region of positive potentials, at which the TiO_2 matrix is insulating, the observed capacitance is due to the Helmholtz layer at the uncovered FTO bottom substrate[4] and it is nearly the same in both, the bare and the covered cases. At more negative potentials, when electrons are injected in TiO_2, the capacitance of the film rises

exponentially with the applied voltage, void circles in Fig. 6.3a, what has been previously identified for bare TiO_2 electrodes in water as a process of accumulation of charge in the semiconductor[3, 4]. We summarize in the following the interpretation of this capacitance:

Assuming that the contact of TiO_2 nanoparticles with the substrate is ohmic, the local electrochemical potential of electrons at the conducting substrate $-eV$, and the Fermi level in the semiconductor network E_{Fn}, are related simply as[4] $-edV = dE_{Fn}$. The capacitance per unit volume in the semiconductor network, corresponding to the Fermi level displacement with respect to the conduction band (Fig. 6.3b), is therefore,

$$C_{TiO_2} = -e\frac{dn}{dV} = e^2\frac{dn}{dE_{Fn}}. \tag{6.1}$$

This equation corresponds to Eq (2.18), previously described in Sec. (2.2), where n is the electron density in the semiconductor. In the semiconductor network, the statistics of electrons is described by the expression (Boltzmann statistics for electrons)

$$E_{Fn} = E_{cb} + k_B T \ln\frac{n}{N_c} \tag{6.2}$$

where E_{cb} is the energy of the lower edge of the conduction band, N_c is the effective density of states in the conduction band, k_B the Boltzmann constant and T the temperature. Using Eq. (6.2), the chemical capacitance of Eq. (6.1) takes the form

$$C_{TiO_2} = \frac{e^2}{k_B T} n \tag{6.3}$$

With the identity $E_{Fn} - E_{F0} = -e(V - V_0)$, that relates the Fermi level and electrode potential to equilibrium values (indicated by subscript 0), the electron density can be expressed $n = n_0 e^{-\alpha e(V-V_0)/k_B T}$, where $\alpha \leq 1$ is an additional constant accounting for

bandgap localized states[4]. In conclusion Eq. (6.3) gives an exponential dependence of the capacitance with respect to the electrode potential.

In order to interpret the capacitance it is also important to take into account that electron charge is transferred from the semiconductor to the viologen molecules adsorbed in the TiO_2 surface. Let c_{red} and c_{ox} denote the concentration (in cm^{-3}) of reduced and oxidized molecules, with $c_{tot} = c_{red} + c_{ox}$. The reduction of viologen molecules is determined by the redox level defined as

$$E_{redox} = E_{redox}^{(0)} + k_B T \ln \frac{c_{red}}{c_{ox}} \tag{6.4}$$

where $E_{redox}^{(0)}$ is the formal redox level for $c_{red} = c_{ox}$. The reduction of the adsorbed molecules at the surface obtained at a small voltage step defines a redox capacitance or pseudocapacitance[5]. This is a particular case of the chemical capacitance[6], as described in Sec. (2.2), which in this case can be expressed as

$$C_{redox} = e^2 \frac{dc_{red}}{dE_{redox}} \tag{6.5}$$

and from Eq. (6.4) we get

$$C_{redox} = \frac{e^2 c_{tot}}{k_B T} x(1-x) \tag{6.6}$$

where x is the fraction of reduced molecules. This capacitance has a bell shape with a maximum value of $e^2 c_{tot} / (4 k_B T)$ at x=1/2, corresponding to $V = E_{redox}^{(0)}$, the standard redox potential of viologen.

Therefore, when applying a negative potential (i.e. when the electrochemical potential of electrons is raised), in the case of the viologen film, the injected charge divides into two branches, one going to charge the chemical capacitance of the semiconductor and the other one filling up the chemical (redox) capacitance of the

viologen. If we suppose that this transfer is nearly reversible with respect to interfacial charge transfer, the redox level of viologen will be close to equilibrium with the Fermi level of the semiconductor, $E_{redox} \approx E_{Fn}$. In this case the two chemical capacitors (and the charge that they accumulate) are controlled by the same potential V, and consequently they are connected in parallel (Fig. 6.4). Thus, the total chemical capacitance of the modified film (and the total charge accumulated on it) is the sum of both contributions while in the case of the bare TiO_2 film, we have only the contribution of the semiconductor and its capacitance is lower.

At the most negative potentials in Fig. 6.3a, the capacitance of viologen modified TiO_2 apparently saturates to a constant value. Two possible reasons can be given for this behaviour. On the one hand, it is possible that the total capacitance of TiO_2 plus viologen rises so much that becomes larger than Helmholtz capacitance at the whole internal surface of the film. In this case, as the electrostatic capacitor in the surface is in series with the chemical capacitance of the film, the smaller will dominate, and the semiconductor enters the state of band unpinning. On the other hand, it is likely that the combination of the exponential increase of the TiO_2 capacitance with the decrease of the viologen capacitance at potentials more negative than $E^{(0)}_{redox}$ also leads, for a certain range of potentials, to a nearly constant capacitance. Data from bare TiO_2 at these potentials, show clearly that Helmholtz limitation is not reached at these potentials. It is thus plausible to assume that the origin of the plateau is the combination of

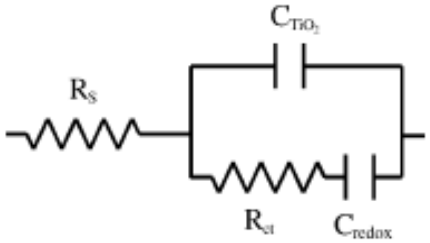

Fig. 6.4. Proposed impedance model for a viologen modified TiO_2 film in the case of existence of charge transfer resistance, R_{ct}, between the semiconductor and the chromophore. R_S is the series resistance, C_{redox} the capacicy of the viologen and C_{TiO_2} the capacitance of the titanium dioxide film according to the expressions described in the text.

capacitances. At more negative potentials, the viologen covered film is expected to follow nearly the same behaviour as the bare TiO_2, but this region, beyond cathodic potential of –0.8 V, was not investigated to avoid degradation of the film.

We can now estimate de evolution of the redox capacitance by subtracting the capacitances of bare and viologen activated TiO_2 (Fig. 6.4). Although this result has to be taken with caution because of possible displacements of the energy levels of TiO_2 related to the adsorption of the viologen, the expected bell shape predicted in Eq. (6.6) is obtained. The maximum, which occurs at the redox potential, is found to be $E_{redox}^{(0)} = -0.6 \pm 0.1$ V. From it we can obtain the lower limit value of $C_{redox}^{\max} = 20$ mF cm^{-2} from which we can estimate $c_{tot} = 3.3 \times 10^{19}$ cm^{-3}.

If the redox process was not completely reversible, there would exist in Fig. 6.3a certain offset between the electrochemical potentials E_{Fn} and E_{redox} related to the charge transfer current between TiO_2 and viologen. It can be shown that this additional physical process leads to modify our previous equivalent circuit model for the viologen system to the one of Fig. 6.4, in which C_{TiO_2} and C_{redox} are at different potentials, the difference being $E_{Fn} - E_{redox}$, which drives the current through interfacial charge transfer resistance R_{ct}, so that the parallel combination of the redox and semiconductor capacitances is decoupled in

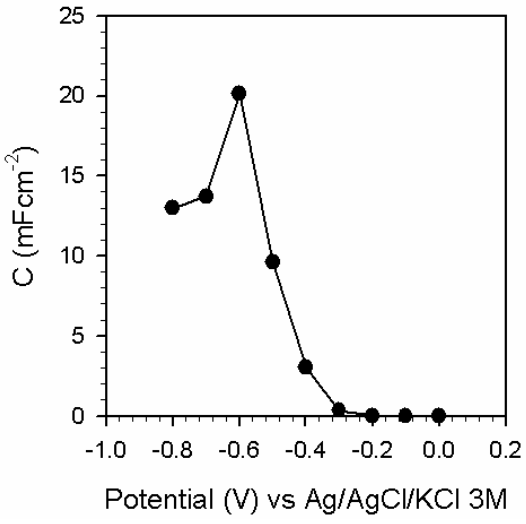

Fig. 6.5. Redox capacitance of viologen resulting from the subtraction of bare and viologen covered TiO_2 films from Fig. 6.3a.

the high frequency region. Note that the simpler parallel capacitance model discussed before is obtained in the particular case of Fig. 6.4 when charge transfer is reversible, $R_{ct} \to 0$. In our measurements, high frequency noise prevented us from determining the presence of this resistance with electrochemical impedance. We remark also that a more complicated situation occurs when the redox potential of the molecules partly shifts when $E_{cb}(TiO_2)$ moves negatively by the change of the Helmholtz potential. The molecule shift depends on the location of the redox centre of the molecule in the adsorbed molecule layer[7].

6.3 Optical voltammetry analysis

Cyclic voltammograms of a viologen modified TiO_2 film at different scan rates are shown in Fig. 6.6. The shapes are very similar to those obtained in a previous work that can be simulated with the equivalent circuit models involving capacitances that depend exponentially on the potential, with and without saturation at the constant capacitance value[4]. As stated in that work and in the same way that occurs in Sec. (4.3), the effect of the series resistance R_S, prevents the film potential (semiconductor Fermi level) to follow exactly the applied potential, because a part of the total potential is taken by the ohmic drop in R_S. This effect is particularly important when large currents are induced, at high scan rates. Therefore, due to R_S the maximum negative voltage achieved by the film (closest Fermi level position to the lower conduction band edge) during the voltammetry is not the return potential but that at which the current becomes zero for the first time in the return scan. At this moment the film has accumulated the maximum charge and thereafter it begins to be extracted. This is an essential point for understanding the evolution of transmittance, as discussed later on.

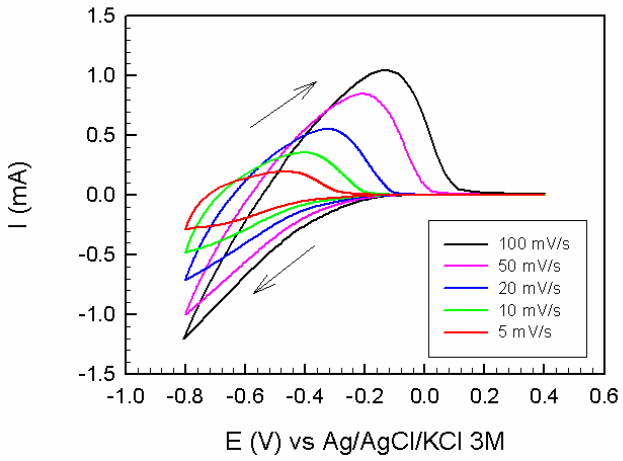

Fig. 6.6. Voltammetries of the viologen deposited film at different scan rates.

The potential at which the capacitance saturates is not reached at the higher scan rates, thus the corresponding voltammograms only show the effect of the exponentially

increasing capacitance. However, at the lower speeds, it can be seen in Fig. 5 that the current tends to a plateau corresponding to the constant capacitance, C_S, obtained by impedance (Fig. 6.3a) that leads to the constant current by the relationship $i = C_S s$, where s is the scan rate.

This interpretation of the voltammetries, explains also some of the major features of the transient transmittances obtained at different scan rates, shown in Fig. 6.7. At the highest rates the potential reached by the film is lower than the potential needed to reduce completely all the viologen. On the contrary, this potential is reached at the lower speeds. This is the reason why the minimum of transmittance decreases with decreasing scan rates and saturates at the lowest of them.

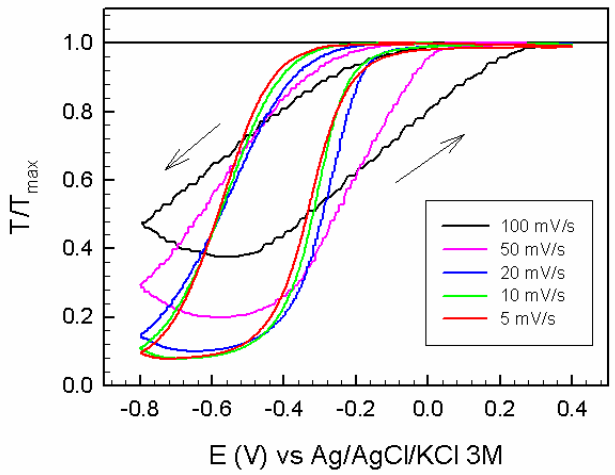

Fig. 6.7. Optical voltammetry of viologen modified TiO_2 measured simultaneously to the cyclic voltammetries taken at different scan rates.

A critical test of this explanation is obtained by analyzing the evolution of the optical change and the electrical response on a common scale of potential. As can be seen in Fig. 6.8, the minimum of transmittance occurs approximately when the voltammogram crosses the zero current voltage axis. This is because the minimum of transmittance needs to be delayed from the return potential until the most negative voltage is attained by the film. This delay is larger the greater the scan rate is.

Other facts that show that the processes of injection and extraction of charge are intimately tied to colouring can be observed in Fig. 6.8. Colouration starts when

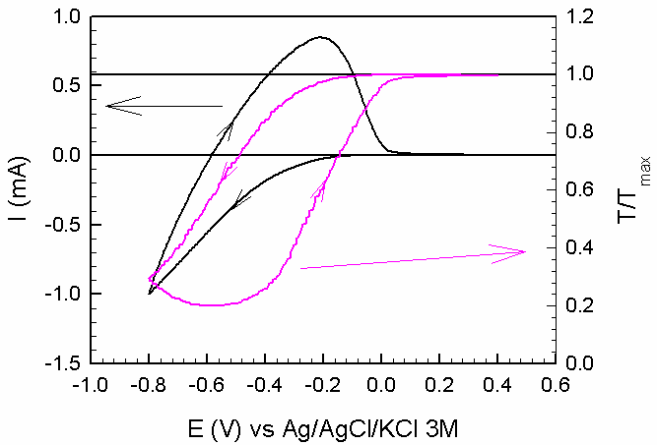

Fig. 6.8. Comparison of the optical (right axis, pink) and electrical (left axis, black) voltammetric response at a 50 mV/s scan rate.

injection current starts to rise and ends when extraction current vanishes, and furthermore the maximum current coincides, approximately with the maximum slope of the bleaching process.

Following with this view of our system, we will check the processes occurring when scanning into more negative potentials at low scan rates (Fig. 6.9). When the potential is first displaced negatively, current and transmittance decrease up to a plateau in current, at the end of which a minimum of transmittance is found. At this potential, the first reduction of viologen has been completed. Note that this plateau corresponds to the constant capacitance found in Fig. 6.3a. At more cathodic potential values, current becomes more negative and transmittance starts to rise. At this point the second reduction of viologen starts resulting in a less opaque colour (yellow) than the first one (deep blue).

When the turning point of potential is reached, the transmittance continues to increase until current becomes zero, where the more negative potential is

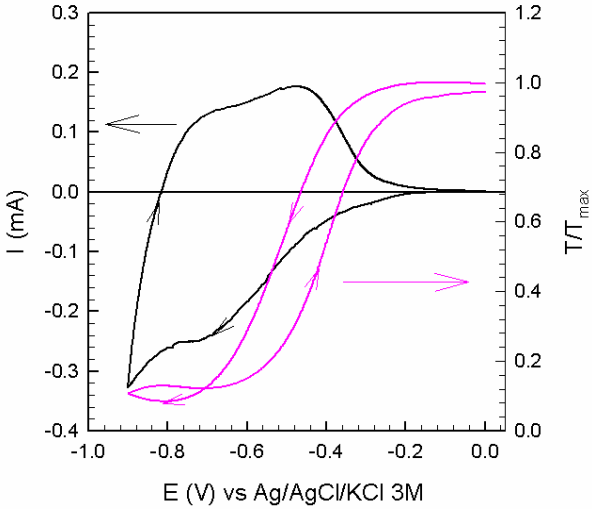

Fig. 6.9. Comparison of the voltammogram (black) taken at a scan rate of 5 mV/s with the transmittance of the film (pink), when potential is given until values where the viologen starts second reduction.

reached in the film (as indicated before) and, consequently, a maximum of transmittance is attained. As current becomes positive, the second reduction is reoxidised to first, and transmittance decreases again until it shows a new minimum indicating that reoxidation from twice reduced viologens is overcome (or even finished) by that of viologen once reduced. Thus, from this point reoxidation to the original bleached state dominates and transmittance increases. That neither the second minimum nor the final transmittance have the same magnitudes than their respective original values probably indicates that the second reduction of viologen is not fully reversible. The fact that at potentials more negative than the plateau the current continues rising, is related to the increase of capacitance due to TiO_2 mentioned above and shown in Fig 6.3a as degradation currents, if present at all, are expected to be low at these potentials.

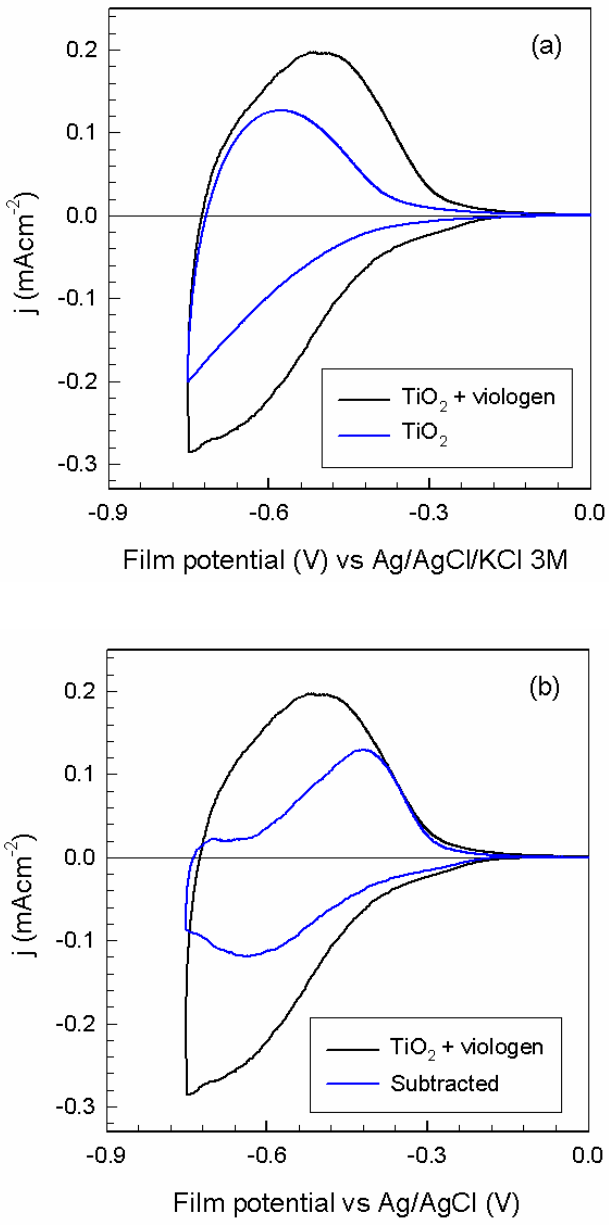

Fig. 6.10. (a) Voltammetry of viologen derivatised TiO_2 compared to the bare TiO_2 at s = 5 mV/s. (b) The same compared to the result of subtraction of normal voltammetries. Film potential is obtained after resistance compensation.

As we did before for

electrochemical impedance, we can study the redox process by comparing the voltammetries of the viologen modified film with the bare TiO_2 (Fig. 6.10). The subtraction of both voltamograms (Fig. 6.10b), shows a profile similar to the bell-shaped redox process that is predicted by Eq. (6.6) and Fig. 6.5. Figure 6.11b also indicates that the contribution of viologen to the overall electrical capacitive response is very significant. From the maximum of the subtracted voltamogram it is possible to calculate the maximum capacitance of the redox process $C_{redox}^{\max} = i_{\max}/s = 25$ mFcm^{-2}, what agrees very well with the result obtained from electrochemical impedance. However, as before, these results should be taken with some caution, as adsorption of viologen on the surface of TiO_2 can displace the voltammogram in the potential axis.

A better way to see the redox process separately is to treat transmittance data taken during voltammetry considering that any variation in the transmittance of the film, T is due to the injection of electrons in the viologen, Lambert -Beer law may be written as

$$A = \varepsilon L \frac{c_{red}}{N_A} \tag{6.7}$$

where, neglecting reflectance, $A = -\ln(T)$ is the absorbance, ε the molar absorption coefficient of reduced viologen and L the film thickness.

If we derive this expression with respect to the potential and take into account that for cyclic voltammetry $\mathrm{d}V = s\mathrm{d}t$, we obtain

$$\frac{\mathrm{d}A}{\mathrm{d}V} = \frac{\varepsilon L}{N_A}\frac{\mathrm{d}c_{red}}{\mathrm{d}V} = \frac{\varepsilon L}{sN_A}\frac{\mathrm{d}c_{red}}{\mathrm{d}t} \tag{6.8}$$

being dc_{red}/dt the variation of reduced viologens with time or, in other words, the current density j that enters viologen molecules divided by the elementary charge and the length of the film. Thus Eq. 6.(8) yields[8]

$$s\frac{\mathrm{d}A}{\mathrm{d}V}=\frac{\varepsilon}{F}\,j \tag{6.9}$$

where F is the faraday constant. Alternatively, the first equality of Eq. (6.8) when compared with Eq. (6.5) shows that $dA/dV \propto C_{redox}$, i.e. the derivative of the absorbance reveals the capacitance of the redox process completely separated from the TiO_2 capacitance contribution. We note that the contribution of Li^+ insertion to coloration of the TiO_2 film can be neglected (Fig. 6.11). It was measured to be less than 10% at the most negative potentials over the bare TiO_2.

In Fig. 6.12 we plot the optical determination of the redox process of viologen [Eq. (6.9)], and compare it with the result of the electrical technique obtained previously from subtraction in Fig. 6.10b. Good agreement is found between both representations of the redox process, though the optical method provides the clearest result. Thus, the cathodic and anodic peak potentials can be computed readily, V_{pc}=-0.63 V and V_{pa}=-0.45 V respectively, what indicates that the process is not completely reversible at these scan rates yielding a standard redox potential $E^{(0)}_{redox}$=–0.54 V vs Ag/AgCl/KCl 3M. This value lies inside the window given by impedance data and 50 mV more positive than that found in a 0.2M $LiClO_4$ in γ-butyrolactone electrolyte[9]. The partial irreversibility of the redox process at low speeds can be understood as

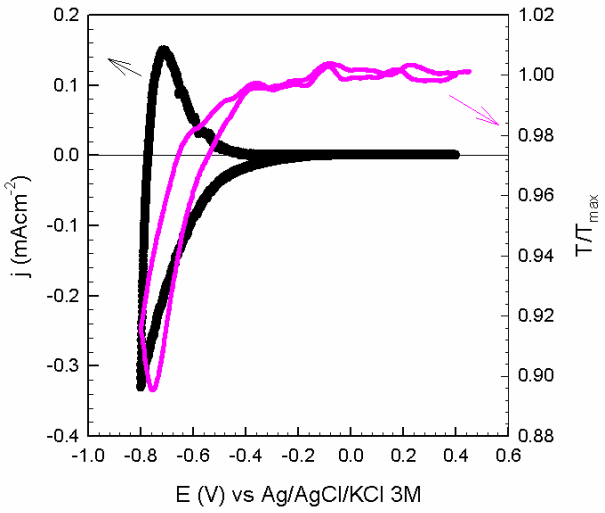

Fig. 6.11. Electric (black) and optical (pink) voltammetric response of a bare TiO_2 film at a 5 mV/s scan rate. A ~10% optical change is observed proving that the ~90% change observed in the viologen modified TiO_2 electrode (Fig. 6.7) is due to the reduction of viologen.

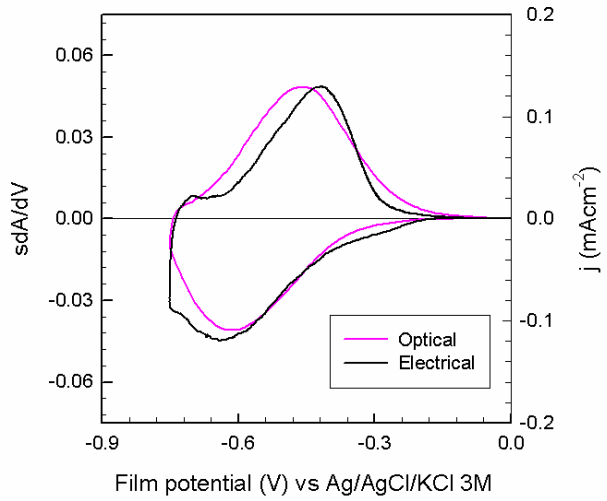

Fig. 6.12. Comparison of the decoupling of the redox process of viologen by the electrical and optical methods. Right axis: subtracted electrical voltammetry obtained in Fig. 6.10b. Left axis: derivate of absorbance times scan rate (5 mV/s).

the separation between the electrochemical potentials, E_{Fn} and E_{redox}, due to kinetic limitations in the charging of viologen, in other words, to the charge transfer resistance proposed in the model of Fig. 6.4.

A value of the molar absorption coefficient ε=3.7 x 10^4 M^{-1} cm^{-1} was estimated from the scaling of Fig. 6.12. Though this value is comparable to those that can be extrapolated from Figs. of[9, 10] respectively, it has to be taken with care as the subtraction we have made to obtain the redox response of Fig. 6.10b is very sensible to the eventual shifts in the potential indicated above.

Assuming this value of ε and that at all the viologens are in the first reduced state at the minimum of transmittance of Fig. 8, through Eqs. (6) and (7) we estimated the concentration of adsorbed viologen c_{tot} =10.2 x 10^{19} cm^{-3} (C_{redox}^{max} =63 $mFcm^{-2}$), which is of the same order of magnitude obtained previously.

6.4 Conclusions

- Viologen activated TiO_2 behaves electrically as a capacitor with a characteristic potential dependence, in series with a resistance mainly due to electrolyte and FTO substrate contributions. At the measured potentials this capacitance is the result of the sum of the Helmholtz capacitance of the uncovered FTO bottom layer (which plays a minor role), and a chemical capacitance that depends on the potential through two contributions: charge accumulation in TiO_2 and the redox capacitance that accounts for the charge injected on the viologen attached in the surface of TiO_2.

- This simple model allows explaining the correlation among impedance, voltammetry and the transmittance change in terms of the time-varying potential applied to the film, that controls the injection of charge through the modulation of the Fermi level in the semiconductor matrix.

- The dynamic response of viologen activated TiO_2 has been described separating the viologen redox process from the overall response of the system. The interfacial charge transfer process is not completely reversible, and the standard redox potential is –0.54 V vs. Ag/AgCl/KCl 3M. Furthermore, the contribution of viologen reduction to the electrical response seems to be rather significant until colouration (redox process) is completed.

6.5 References

(1) J. García-Cañadas, F. Fabregat-Santiago, J. Kapla, J. Bisquert, G. Garcia-Belmonte, I. Mora-Seró and M. O. M. Edwards. *Electrochim. Acta* 49 (2004) 745.

(2) D. Cummins, G. Boschloo, M. Ryan, D. Corr, S. N. Rao and D. Fitzmaurice. *Journal Physical chemistry B* 104 (2000) 11449.

(3) F. Fabregat-Santiago, G. Garcia-Belmonte, J. Bisquert, A. Zaban and P. Salvador. *J. Phys. Chem. B* 106 (2002) 334.

(4) F. Fabregat-Santiago, I. Mora-Seró, G. Garcia-Belmonte and J. Bisquert. *J. Phys. Chem. B* 107 (2003) 758.

(5) B. E. Conway. *Electrochemical supercapacitors*. Plenum Publishing (1999).

(6) J. Jamnik and J. Maier. *Phys. Chem. Chem. Phys.* 3 (2001) 1668.

(7) A. Zaban, S. Ferrere and B. A. Gregg. *J. Phys. Chem. B* 102 (1998) 452.

(8) S. L. D. Maranhâo and R. M. Torresi. *Electrochim. Acta* 43 (1998) 257.

(9) R. Cinnsealach, G. Boschloo, N. S. Rao and D. Fitzmaurice. *Sol. Energy Mater. Sol. Cells* 57 (1999) 107.

(10) P. Bonhote, E. Gogniat, F. Campus, L. Walder and M. Grätzel. *Displays* 20 (1999) 137.

7. Electrochromic device

7.1 Preparation and assembly

7.2 Description of the device

7.3 Device performance

7.4 Conclusions

7.5 References

7. Electrochromic device

In this chapter we will describe two small-area electrochromic devices prepared in our laboratory using a-WO_3 as electrochromic layer. The aim of this chapter is to illustrate how a device can be constructed and work properly, not to fabricate a commercially competitive device, for which a larger effort will be necessary and it is out of the scope of this thesis.

7.1 Preparation and assembly

As it was introduced in Sec. 1.3.2., an electrochromic window is formed by several layers, generally seven (see Fig. 1.13.). Two devices, A and B, were prepared having both the following structure:

Glass / ITO / a-WO_3 (200 nm) / Ionic Liquid / X-layer / ITO / Glass

X-layer was electrochemically polymerised poly(3,4-ethylenedioxypyrrole) (PEDOP), for device A, and an Sb-doped SnO_2 nanoporous film in the case of device B. Both layers were deposited over ITO/glass substrate. 200 nm a-WO_3 films were prepared and deposited over ITO/glass substrate as reported in Sec. 4.1.1. A 0.1 M Lithium trifluoromethane-sulfonimide (LiTFSI) (Aldrich) solution in 1-ethyl-3-methylimidazolium bis((trifluoromethyl)sulfonyl)amide (EMITFSI) ionic liquid was used as electrolyte. The synthesis of EMITFSI was performed according to published procedure[1].

PEDOP films were deposited over ITO (Delta Technologies) (15 Ω/ of surface resistance) by means of two voltammetric cycles between 1.0 and -0.8 V at 10 mV/s

(see Fig 7.1). Monomer 3,4-ethylene dioxypyrrole (Aldrich) 0.01M and 0.1M $LiClO_4$ (Fluka) were solved in anhydrous propylene carbonate (Aldrich) and used as electrolytic solution. Pt wire was used as counter electrode and Ag/AgCl/KCl 3M electrode connected to the system by means of a salt bridge containing the electrolytic solution without the monomer was used as reference. Nitrogen was bubbled before and over the experiments. After polymerization, the film was washed with acetonitrile and dried in air before incorporate it in the device.

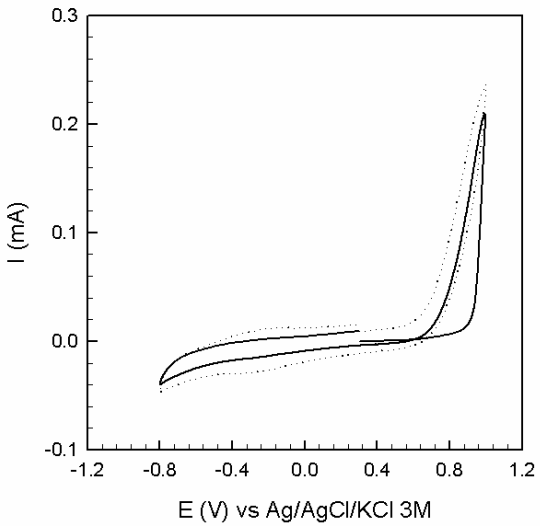

Fig. 7.1. Ellectrodeposition of PEDOP onto an ITO film by means of two voltammetric cycles. The first one (-) and the second (·). A 0.01M 3,4-ethylene dioxypyrrole and 0.1M $LiClO_4$ in propylene carbonate solution was employed.

Sb-doped SnO_2 nanoporous films were prepared by spreading a polymer precursor solution (Alfa Aesar) over the ITO substrate and sintered at 450 ºC for 20 minutes in air. This process was made twice in order to increase the thickness of the film.

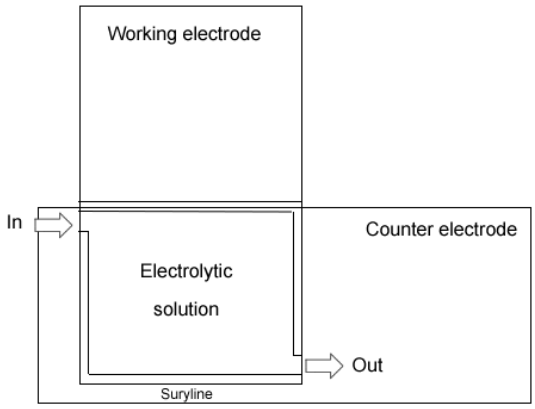

Fig. 7.2. Scheme showing how the devices were assembled. A drop of electrolytic solution was placed at the IN position which advanced to the OUT by capillarity to fill the whole space.

The devices were assembled as a sandwich-type cell by using Surlyn 1472 polymer (DuPont), which stuck the electrodes when it was heated at about 80-90 ºC. Afterwards, the electrolytic solution was inserted by capillarity in the cavity. Finally the whole cell was sealed with epoxy resin

(Nural 92) to avoid liquid leakage. Both devices showed an area of ~1.0 cm^2.

7.2 Description of the device

The electrochromic windows prepared are based on a-WO_3 (200 nm) as the elctrochromic layer. To complete the whole device an electrolytic solution and a counter electrode were needed.

The EMITFSI ionic liquid was employed as the ionic conductor. Recently ionic liquids have attracted the attention of a lot of researchers because of their physical and chemical properties[2]. They are non-volatile and non-flammable, and have high thermal stability. From an electrochemical point of view, ionic liquids have excellent properties such as high-ionic conductivity and wide potential windows. They are fluid over a wide temperature range with higher viscosities than either aqueous or organic electrolytes. Some ionic liquids have also the advantage that they can be obtained in a very dry state, making them especially suitable for applications in electrochemical systems from which moisture must be excluded over long periods of operation. Recently, was reported that ionic liquids enhance lifetimes and cycling switching speeds in π-conjugated polymer electrochemical devices[2]. Apart from that, its use has been extended to other electrochemical devices such as solar cells[3], lithium batteries[4], fuel cells[5] and supercapacitors[6].

In the electrochromic window set up the counter electrode plays the role of accommodating the opposite charge accumulated in the electrochromic layer (working electrode) without changing its Fermi level significantly (high capacitance), achieving in that way the lower possible external voltage to make the device work. For the electrochromic device A, a film of PEDOP was employed as counter electrode. This conducting polymer is electrochemically stable and also electrochromic, changing from

a red neutral state to a light blue-grey oxidized state[7]. Nevertheless, it is thought that a significant electrochromic change of the polymer is not produced in our device. The large amount of PEDOP deposited accommodates easily the charge needed to balance the inserted charge in the WO_3 layer without changing the oxidation state (colour) in the PEDOP film significantly. In the case of device B, a nanoporous Sb-doped SnO_2 film was used as counter electrode[8]. Due to the nanoporous nature of the film, it shows a large effective area and the charge is easily accommodated in the electrolyte/electrode double layer. Moreover, this layer is quite transparent and it is thought that a significant electrochromic change is not produced on it, as in the case of PEDOP.

7.3 Device performance

To evaluate the performance of the devices we carried out cyclic voltammetry experiments (scan rate 50 mVs^{-1}) and cycling between two voltage values. Along both experiments, the transmittance change was registered simultaneously at 543.5 nm using a He-Ne laser and collecting the optical signal by means of a silicon photodiode. Transmittance data were normalised by dividing by the maximum transmittance value. Figures 7.3 and 7.4 show the coloration states of the devices. Pictures were taken at the voltage values between which the cells were cycled. For the bleached and coloured states, 2.2 and -3.2 V were applied respectively in device A. In the case of device B transparent and coloured states corresponded to 2.0 and -3.0 V respectively.

Fig. 7.3. Electrochromic device A (PEDOP as counter electrode) in the bleached (2.2 V, left) and coloured (-3.2 V, right) state. Approximately a 40% transmittance change can be obtained. Area ~ 1 cm^2.

Fig. 7.4. Electrochromic device B (Sb-doped SnO_2 as counter electrode) in the bleached (2.0 V, left) and coloured (-3.0 V, right) state. Approximately a 65% transmittance change can be obtained. Area ~ 1 cm^2.

Cyclic voltammetry experiments were obtained at the same time that the optical change was recorded (see Fig. 7.5). It is observed that the coloration-decoloration process is produced only when current passes through the system (accumulation and

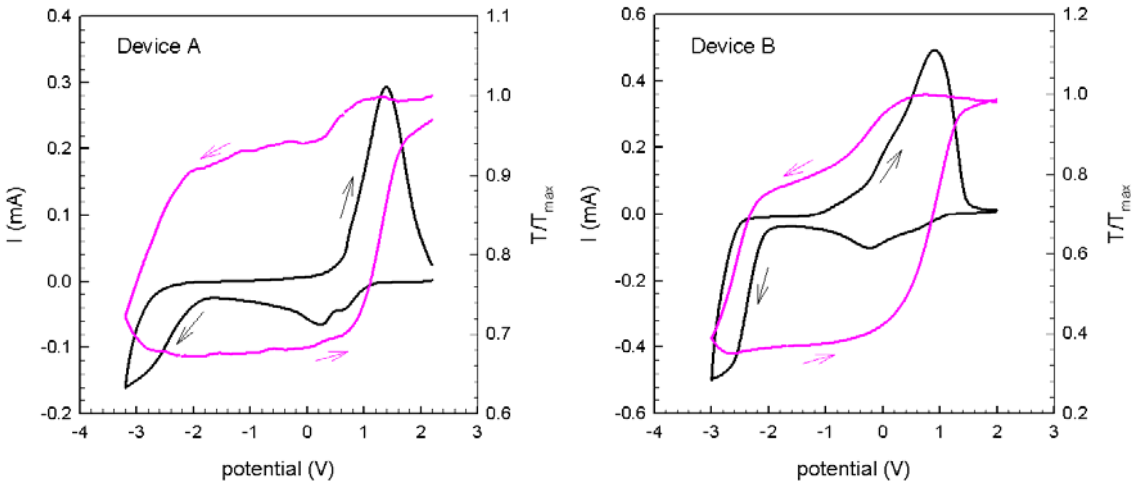

Fig. 7.5. Cyclic voltammograms (black) and transmittance change (pink) registered at 50 mVs^{-1} for the devices prepared. Arrows indicate the direction of the scans.

release of charge). About 30% of transmittance change is observed in device A, meanwhile a value close to 70% is achieved for device B. To check the stability of the devices 10 cycles between 2.2 and -3.2 V were performed for device A and between 2.0 and -3.0 V in case of device B (Fig. 7.6). Interval time was 4 s in both cases. It is observed that the devices are not very stable and what it is more bubbles appear in the device after several cycles presumably due to decomposition of the electrolyte. To improve stability of the windows a research of more suitable electrolytes will be necessary, but this is out of the purpose of this thesis, where we simply would like to show devices offering a good performance. A review of the best devices available to date is given in the introductory chapter.

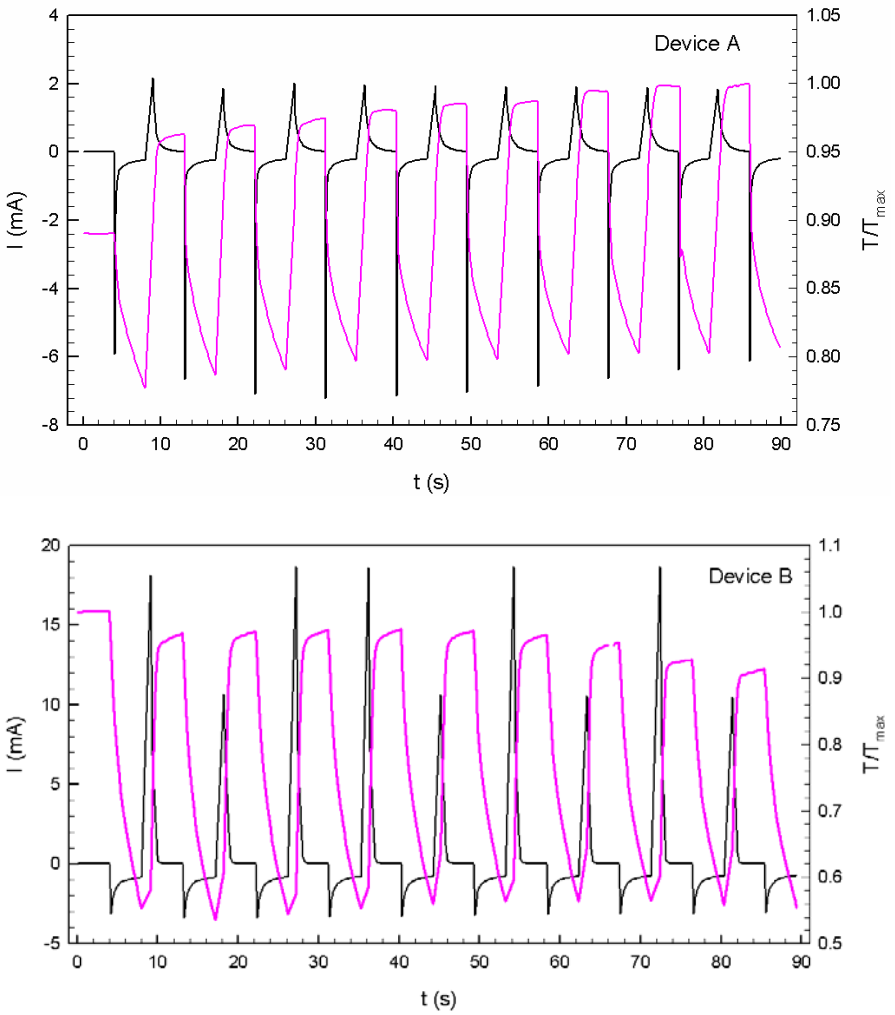

Fig. 7.6. Cycling between 2.2 and -3.2 V (Device A) and 2.0 and 3.0 V (Device B), with a 4 s interval time. Black line is current and pink one transmittance, normalised to the maximum value.

7.4 Conclusions

Two devices based on a-WO_3 as electrochromic layer were prepared. Device A consisted on a film of PEDOP as counter electrode and a nanoporous Sb-doped SnO_2 film for device B. Ionic liquid served as electrolyte. A good transmittance change from transparent to blue was obtained. Nevertheless, stability of the devices was poor, presumably due to the decomposition of the electrolyte.

7.5 References

(1) P. Bonhote, A. P. Dias, N. Papageorgious, K. Kalyanasundaram and M. Grätzel. *Inorganic Chemistry* 35 (1996) 1168.

(2) W. Lu, A. G. Fadeev, B. Qi, E. Smela, B. R. Mattes, J. Ding, G. M. Spinks, J. Mazurkiewicz, D. Zhou, G. G. Wallace, D. R. MacFarlane, S. A. Forsyth and M. Forsyth. *Science* 297 (2002) 983.

(3) P. Wang, S. M. Zakeeruddin, P. Comte, I. Exnar and M. Gratzel. *J. Am. Chem. Soc.* 125 (2003) 1166.

(4) B. Garcia, S. Lavallée, G. Perron, C. Michot and M. Armand. *Electrochim. Acta* 49 (2004) 4583.

(5) M. A. B. H. Susan, A. Noda, S. Mitsushima and M. Watanabe. *Chem. Commun.* 8 (2003) 938.

(6) J. D. Stenger-Smith, C. K. Webber, N. Anderson, A. P. Chafin, K. Zong and J. R. Reynolds. *J. Electrochem. Soc.* 149 (2002) A973.

(7) P. Schottland, K. Zong, C. L. Gaupp, B. C. Thompson, C. A. Thomas, I. Giurgiu, R. Hickman, K. A. Abboud and J. R. Reynolds. *Macromolecules* 33 (2000) 7051.

(8) J. Liu and J. P. Coleman. *Materials Science and Engineering: A* 286 (2000) 144.

8. Final conclusions and future lines

Along this work new models that describe the thermodynamics of different electrochromic materials such as amorphous WO_3 and conducting polymers have been described. A deeper insight has been gained in the study of such systems with the application of these models.

The main results found for the different materials studied can be summarised as follows:

- a-WO_3: An approach to explain the voltage-composition curves considering lattice host distortions caused by intercalant-host interactions has been given. The parameter G governs the interaction, showing a strong variation with thickness. A comparison of the thermodynamic function with a previous model describing host lattice expansions led us to calculate volume change produced in the films. Using simple electrochemical methods and analyzing the chemical capacitance results, the volume change experienced by the film along intercalation can be calculated, which are in good agreement with direct profilometry data. Measurements of the diffusion coefficient and the potential barrier height for the hopping process were obtained. Both chemical diffusion and jump diffusion coefficients decrease along intercalation, in accordance with the host distortion model proposed. A distinctive behaviour was observed for the 100 nm film where volume changes were not observed. This fact points to the occurrence of a particular intercalation mechanism related with the reduction of the size that will be left for future investigations.

- Conducting polymers: The voltammetry of conducting polymers typically shows rather broadened oxidation peak followed by a current plateau. These peaks are too broad to be interpreted in terms of simple nernstian statistics. A Gaussian

distribution of sites energies is proposed and able to explain the first part of the peaks, till the current plateau appears. The distribution provides an important tool for analyzing the distribution of polarons and bipolarons energy levels. A capacitive behaviour is supposed to be involved in the plateau region but its origin is not well understood yet and will be the object of future work.

- Viologen modified electrode: Electrochemical and optical behaviour of a viologen modified n-TiO_2 electrode has been studied. The capacitive response of the electrode shows three different contributions due to the uncovered FTO/electrolyte capacitance, the chemical capacitance of the TiO_2 and the redox capacitance of the viologen adsorbed molecules. Optical transmittance measurements have been explained qualitatively. Colouration change is mainly due to the reduction of adsorbed viologen molecules. Extraction of the electrical process due to the viologen redox process solely can be achieved from optical voltammetry measurements. Standard redox potential and molar absorption coefficient can be obtained, which shows a good agreement with the values from the literature. Once described the behaviour of the modified electrode by itself, it should be interesting to study its behaviour in a complete device, where two electrodes are presented and depending on the electrolyte employed band movements or even different conduction mechanisms can be observed.

- Finally, and as a demonstration, two electrochromic windows were prepared based in a-WO_3 as electrochromic layer, ionic liquid as electrolyte and PEDOP conducting polymer or Sb-doped nanoporous SnO_2 as counter electrodes. The devices showed good performance but poor stability.